Investigation of Partially Premixed Combustion Instabilities through Experimental, Theoretical, and Computational Methods

by

YunTao Chen

A dissertation submitted in partial fulfillment
of the requirements for the degree of
Doctor of Philosophy
(Aerospace Engineering)
in The University of Michigan
2015

Doctoral Committee:

Professor James F. Driscoll, Co-Chair
Assistant Professor Matthias Ihme, Co-Chair, Stanford University
Assistant Professor Mirko Gamba
Professor Volker Sick

To my parents, who enlightened me on the purpose of life.

ACKNOWLEDGEMENTS

I have been lucky to be able to claim that my work for the last five years is my real passion. However going through five years of graduate school is still proved to be quite challenging. Not only a firm belief on the path that I have chosen was needed, the help of others around me has also been essential.

First and foremost, I'd like to thank my advisors, Prof. Driscoll and Prof. Ihme. I would not be in this department and have this wonderful educational experience if Prof. Ihme did not recruit me five years ago. From him I learnt the discipline and dedication that a young professional needs to succeed in this competitive world. And if not for Prof. Driscoll, I would not be able to learn things "on the other side of the fence," i.e. to be an experimentalist (albeit self-claimed). Prof. Driscoll taught me more than the technical expertise that he has, he showed me that you can still be a gentleman in academia, an environment that is mostly governed by the jungle rule. In this regard I also want to thank Prof. Hong G. Im, who was generous to let an undergraduate to work in his lab, which laid the foundation for the rest of my career.

This thesis can not be completed without the additional insights from Prof. Gamba and Prof. Sick. Prof. Gamba is both knowledgable and very willing to help students at most needed time. He also showed me with his own example what kind of dedication is needed to start one's career. Prof. Sick was very generous to accept my invitation to be on my committee. As always, a kind and understanding person who possesses world-leading expertise is not someone who you meet very often.

I believe that the education you get in the graduate school is not about finishing your thesis projects, but the opportunity to immerse yourself into an highly intellectual environment. This environment is built by the people that work with you day to day. The fellow graduate students that I met in Michigan are capable of living to that claim. The help from my seniors, Dr. Yee Chee See, Dr. Patton Allison, and Dr. Jacob Temme bridged the knowledge gaps between classes and my own research problem. Guys (unfortunately that's literally accurate) in my office, DJ Lee, Chan Wai Lee, Clarance Gan, Hara Kentaro, Chris Koh, Brad Maeng, Sun Yong, all provided the comradeship that is indispensable. The assistance from my group mates, Bharat Tulsyan, Aaron Skiba, Tim Wabel, Robin Klomparens, and Rohan Morajkar, are much appreciated. I'd also like to thank my friends across the street in the AOSS department, for accepting me as the honorary member of their Chinese student circle when a Chinese companion is a rarely available in the aero department, except my friends and fellow aero engineers Lyu Zhoujie (Peter) and Zhang Dianyun.

Lastly, but most importantly, I want to thank my parents. They gifted me with all the physical and mental strength that is needed to plow through the path that leads to where I am today. This thesis is dedicated to my parents, although they would probably prefer a couple of grandchildren instead.

TABLE OF CONTENTS

CHAPTER

LIST OF FIGURES

Figure

LIST OF TABLES

Table

LIST OF ABBREVIATIONS

CFD	Computational Fluid Dynamics
DLR	*Deutsches Zentrum für Luft- und Raumfahrt*, German Aerospace Center
DME	Dimethyl Ether
DNS	Direct Numerical Simulation
FDF	Flame Describing Function
FFT	Fast Fourier Transform
FoV	Field of View
FPV	Flamelet/Progress Variable
GTMC	Gas Turbine Model Combustor
IRO	ICCD Relay Optics (Optical Intensifier)
LDV	Laser Doppler Velocimetry
LES	Large Eddy Simulation
MRMF	Modular Reduced-order Model Framework
PDF	Probability Density Function
PIV	Particle Image Velocimetry
PLIF	Planar Laser Induced Fluorescence
PPJB	Piloted Premixed Jet Burner
PVC	Precessing Vortex Core
RANS	Reynolds Averaged Navier Stokes
RHS	Right Hand Side (of an equation)
SGS	Sub-Grid Scale

LIST OF SYMBOLS

Latin Symbols

AFR_{st}	Stoichiometric air-fuel ratio
C	Progress variable (Chapter II)
c	Speed of sound (Chapter III)
D	Element equivalent diameter
k	Acoustic wave number
l	Element length
P	Pressure
S	Element cross section area
T	Temperature
t	Time
U	Axial velocity
V	Element volume
y	Species mass fraction
Z	Mixture fraction (Chapter II)

Greek Symbols

γ	Ratio of heat capacities
ω	System instability frequency [rad/s]
ω_0	Plenum Helmholtz frequency of GTMC
ω_2	Combustion chamber Helmholtz frequency of GTMC
ϕ	Equivalence ratio

ψ_{20}	Combust. chamber/plenum phase difference of GTMC
ρ	Density of mixture
τ_{c}	Convection time scale
Θ	Fuel-specific parameters in Eq.(3.43)

Other Symbols

$\Delta h_{\mathrm{f}}^{\circ}$	Lower heating value
$\dot{m}$	Mass flow rate
$\jmath$	Square root of -1
$\mathcal{L}$	Burner-specific parameters in Eq.(3.43)
$\mathcal{Z}$	Acoustic impedance (Chapter III)

Subscripts

0	Plenum properties
1	Injector properties
2	Combustion chamber properties
3	Chimney properties
a	Air
b	Burnt mixture
f	Fuel
ref	Reference (point, solution, value, etc.)
r	Real part (of a complex number)
tot	Total (fuel and air)
u	Unburnt mixture

Superscripts

$\dot{x}$	Rate of variable x
$\overline{x}$	Reynolds-filtered variable x (Chap. I & II); average of variable x (Chap. III)
$\widehat{x}$	Magnitude of complex number x
$\widetilde{x}$	Favre-filtered variable x
x'	Fluctuation of variable x

ABSTRACT

Investigation of Partially Premixed Combustion Instabilities through
Experimental, Theoretical, and Computational Methods
by
YunTao Chen

Co-Chairs: James F. Driscoll and Matthias Ihme

Partially premixed combustion has the merits of lower emission as well as higher efficiency. However, its practical application has been hindered by its inherent instabilities. This work is a study of instabilities in partially premixed combustion, through a combination of numerical simulation, theoretical modeling, and experimental investigation, with the hope of furthering our understanding of the underlying physics. Specifically, a Flamelet/Progress Variable (FPV) combustion model in the context of Large Eddy Simulation (LES) is extended to simulate a piloted (partially) premixed jet burner (PPJB). The ability and shortcomings of this state-of-the-art high fidelity combustion model are assessed. Furthermore, a Modular Reduced-order Model Framework (MRMF) is developed to integrate a range of elementary models to describe the instabilities that may occur in combustors utilizing partially premixed combustion technologies. A multi-chamber Helmholtz analysis is implemented, which is shown to be an improvement over previous single-chamber analyses. The assumptions and predictions of the proposed model are assessed by pressure and simultaneous Particle Image Velocimetry (PIV)–formaldehyde (CH_2O) Planar Laser Induced Fluorescence (PLIF) measurements on a Gas Turbine Model Combustor (GTMC) at a sustained rate of 4 kHz. The proposed model is shown to be able to predict the instability frequency at experimental conditions. It also explains the trends of the variation of instability frequency as mass flow rates and burner geometry are changed, as well as the measured phase shift between different chambers of the burner. Finally, under the current framework an explanation of the dependence of the existence of combustion instability on equivalence ratio is provided.

CHAPTER I

Introduction

1.1 Motivation

At the turn of this century, fossil fuels have been labeled as the energy source of the past. They bear the blame of environment pollution and face the threat of a dwindling supply. Much attention was focused on the development of renewable and clean energy sources such as wind, solar, nuclear and hydrodynamic energy. Despite this trend, most of the transportation industry still depends on the combustion of fossil fuels to power cars, lorries, ships, and airplanes. There have not been any feasible alternative energy sources capable of replacing combustion engines in heavy duty missions in near future.

Additionally, in recent years a series of events have made the global energy industry to change its attention. After the nuclear leaks in Fukushima power plant in Japan, nuclear energy, the most stable source among all clean energy, were under much suspicion from the public. The advancement in fracking and shale gas extraction technology made North America a new source of supply for fossil fuels. Fracking does not only ensure the self-sufficiency of energy need of the North American countries, it also drives down the fossil fuel price in the global market. The oil price has drop sharply in the last year, from well above $100 per barrel in early 2010s to currently about $40 per barrel in late 2014. As a result, there have been renewed interests in fossil fuel combustion, especially in utilizing the newly available natural gas supply in power generation.

The moral of the story is that the combustion of fossil fuel is going to be here to stay for a long time. This motivates us to reflect on our way of burning fossil fuels and to explore new technologies to remedy some of the negative effects of traditional combustion engines. One of the areas of interest is the reduction of air pollution, mostly $\mathrm{NO_x}$. The formation of $\mathrm{NO_x}$ in combustion devices is a result of $\mathrm{N_2}$ molecules reacting with O_2 molecules in a high temperature environment for a sustained period of time. Among technologies brought in to reduce NO_x pollution, partially premixed combustion is one of the rising stars. This is a relatively new field of research in combustion sciences, and there are still many aspects of partially premixed combustion that we do not fully understand. For example, the problem of combustion instabilities has plagued many practical applications of this technology and we do not have a full understanding of the causes of this instability, let alone accurately predict it.

It is the target of this thesis to gain a deeper understanding of partially premixed combustion processes, especially that of combustion instability. The end goal is to use this knowledge to aid the development of next-generation of combustion engines with improved efficiencies and reduced emissions. In the following sections, the basic concepts and techniques that were involved in the present work are introduced. Then the specific goals and the outline of this work will be discussed.

1.2 Partially Premixed Combustion

The term "Partially Premix Combustion" spun out from the concept of premixed combustion. In terms of fuel and oxidizer mixing process, canonical combustion processes can be separated into two regimes: premixed combustion, in which fuel and oxidizer are well mixed to reach a homogeneous state before ignition, and non-premixed combustion, in which fuel and oxidizer are well separated before ignition. Premixed combustion and non-premixed combustion are dominated by different physical interactions, hence two distinct and separated set of theories have been developed to describe each regime. This also leads to different modeling approaches for premixed and non-premixed flames.

However, in practical combustion applications, seldom is a flame completely in a premixed flame regime or in a non-premixed flame regime. Instead, fuel and oxidizer are usually mixed incompletely before ignition, in which case the flame has to propagate in a stratified mixture. This process can not be characterized either by premixed or non-premixed combustion. And this is where the term "Partially Premixed Combustion" comes into being. This regime is not only unavoidable in many cases, but also quite desirable in most of them. This is because partially premixed combustion configurations usually are at the optimum point between pure premixed and non-premixed combustion, they provide improved efficiency and reduced pollution than non-premixed configurations, while being more robust and easily-controlled than pure premixed configurations.

One example of flames in the partially premixed regime is a lifted turbulent jet non-premixed flame. This is relevant to practical applications because similar processes can be found in jet engines and stationary gas turbine generators. An example of a lifted non-premixed flame is shown in figure 1.1.

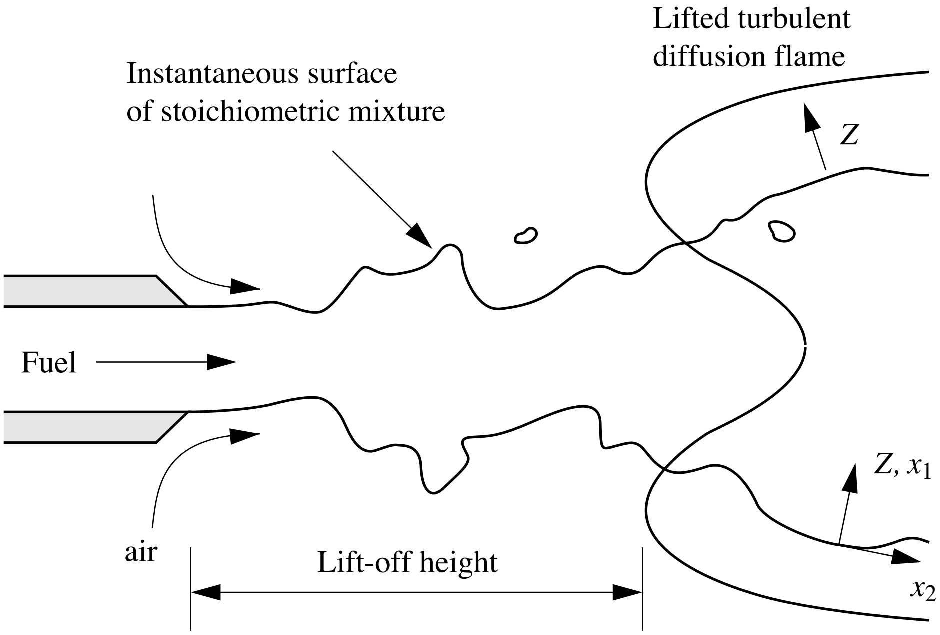

Figure 1.1: Schematics of a lifted turbulent jet flame [1]

In this example, a jet of fuel is issued into air from a nozzle. When the exit velocity is small, the flame will be anchored at the rim of the nozzle. As the exit velocity is increased, the shear stress between fuel and air is increased. When the resulting stretching rate exceeds that of the quenching limit of a non-premixed flame, the attached flame will be extinguished at the rim. However, if the jet velocity is not too large, the flame will reestablish itself somewhere downstream where the local stretching rate is again within the quenching limit. At this moment the schematics of the flame dynamics will be the one shown in figure 1.1. Fuel is partially mixed with air before entering the flame region.

One quantity of much interest to practical engine designers of similar configurations is the flame lift-off height (as labeled in figure 1.1). This is because in practical applications, the lift-off height has to be sufficiently large to avoid excess heat transfer from the flame to the injector nozzle. The uniqueness of partially premixed flame reveals itself in the prediction of lift-off height of the lifted flame. It is found that neither a premixed combustion theory or a non-premixed combustion theory can completely explain and predict the lift-off processes [12]. This example highlighted the difficulties shared by understanding and predicting many other variables in partially premixed combustion. Specifically, in many circumstances, the knowledge and experiences acquired from many decades of research in canonical premixed and non-premixed flames can not be readily applied to partially premixed combustion regime. This opens a new frontier of combustion research that calls for continuous efforts of combustion researchers.

1.3 Combustion Instability

Combustion instability is characterized by the phenomenon of large heat release and flame location oscillations. In practice, combustion instability is usually coupled with acoustic instability, which is defined as the process of an exponentially growing pressure oscillation amplitude or a limit cycle of pressure oscillations sustained at a large amplitude. The relationship between combustion instability and acoustic instability was investigated by Lord Rayleigh [13], who stated that acoustic oscillations are amplified by heat release when the latter is in phase with pressure oscillations. This is called the Rayleigh criterion. Similarly, acoustic oscillations are damped if heat release and pressure oscillations are out of phase. One way of quantifying the Rayleigh criterion is to calculate the so-called Rayleigh integral:

$$\mathcal{R}_{\text{int}} = \int_0^T p' \dot{q}' dt \tag{1.1}$$

where p' denotes the pressure oscillation and $\dot{q}'$ denotes the heat release oscillation. The Rayleigh criterion is satisfied when the Rayleigh integral is larger than zero.

Combustion instability is one of the key obstacles that engineers face while designing combustion devices utilizing premixed or partially premixed combustion technology. In practice, combustion instability usually occurs in the combustion chamber of gas turbine engines. It will result in large fluctuations of pressure and temperature, thus subject the exit liner and high temperature turbine to large and asymmetric fluid mechanic and thermal loads. This may lead to the catastrophic failure of the downstream components of the engine, which will result in substantial capital lost and potentially fatal accidents.

Combustion instability is already known to be governed by pressure oscillations and heat release oscillations. However, each of these oscillations can be caused by various factors. Pressure oscillations can be initiated by standing waves, resonance of certain resonators, and other flow features. Heat release oscillations can be caused by equivalence ratio oscillations [14] as well as flame surface area oscillations [15]. Because of the numerous possible combinations of different modes of pressure and heat release oscillations, it is usually very difficult to accurately predict the existence and properties of combustion instabilities.

1.4 Large Eddy Simulation

Large Eddy Simulation (LES) is a method developed for Computational Fluid Dynamics (CFD) to remedy the formidable cost in resolving all relevant scales of turbulent flows in numerical simulations. One of the pioneers in advocating this method is J. Smagorinsky [16]. The physical reasoning behind this method is based on the fact that most of the energy in a turbulent flow is contained in the large and distinct structures, as shown in figure 1.2. Hence it is desirable to resolve the important energy-containing large scales, while leaving the small scales that are very expensive to compute to a well-designed model. The scales that are not resolved are the residue or the so-called Sub-Grid Scale (SGS).

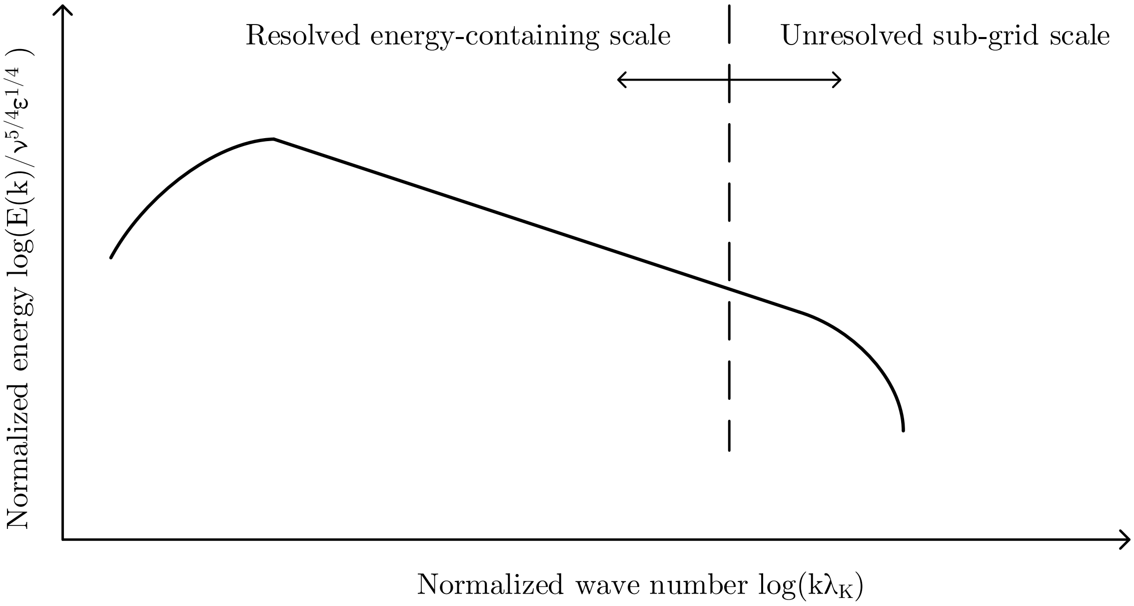

Figure 1.2: Energy spectrum of turbulent flows and the separation of scales in LES

The essence of the separation of scales in LES lies in the spacial and temporal filtering of the flow field, so that the resolution of the grid can be reduced compared to Direct Numerical Simulation (DNS). The filtering process takes the form:

$$\overline{\eta(\mathbf{x},t)} = \int_{-\infty}^{\infty}\int_{-\infty}^{\infty} \eta(\mathbf{r},t')\cdot \mathcal{G}(\mathbf{x}-\mathbf{r},t-t')dt'd\mathbf{r} \ , \tag{1.2}$$

where $\mathcal{G}(\mathbf{x}-\mathbf{r},t-t')$ is the LES filter. Equation 1.2 is usually called Reynolds-filtering. This filter has a characteristic length and time scale associated with it, which is of the same order of magnitude as the LES grid size. A density weighted filtering is also defined for reacting flows with large temperature/density variations:

$$\widetilde{\eta(\mathbf{x},t)} = \frac{1}{\overline{\rho}}\int_{-\infty}^{\infty}\int_{-\infty}^{\infty} \rho\cdot\eta(\mathbf{r},t')\cdot \mathcal{G}(\mathbf{x}-\mathbf{r},t-t')dt'd\mathbf{r} \ . \tag{1.3}$$

This filtering process is called Favre-filtering. Reynolds-filtering and Favre-filtering are related by:

$$\widetilde{\eta} = \frac{\overline{\rho\eta}}{\overline{\rho}} \ . \tag{1.4}$$

Instead of the classical Navier-Stokes equations, a LES code solves a filtered version of the governing equations. Take the momentum equation as an example, the Navier-Stokes equation takes the form:

$$\rho\frac{\partial u_{\mathrm{j}}}{\partial t} + \rho u_{\mathrm{k}}\frac{\partial u_{\mathrm{j}}}{\partial x_{\mathrm{k}}} = -\frac{\partial p}{\partial x_{\mathrm{j}}} + \frac{\partial \sigma_{\mathrm{jk}}}{\partial x_{\mathrm{k}}}, \tag{1.5}$$

where σ is the stress tensor.The counterpart of Eq.(1.5)in the filtered form would be:

$$\overline{\rho}\frac{\partial \widetilde{u}_{\mathrm{j}}}{\partial t} + \overline{\rho}\widetilde{u}_{\mathrm{k}}\frac{\partial \widetilde{u}_{\mathrm{j}}}{\partial x_{\mathrm{k}}} = -\frac{\partial \overline{p}}{\partial x_{\mathrm{j}}} + \frac{\partial \overline{\sigma_{\mathrm{jk}}}}{\partial x_{\mathrm{k}}} + \frac{\partial \sigma^{\mathrm{res}}_{\mathrm{jk}}}{\partial x_{\mathrm{k}}}. \tag{1.6}$$

The solution to this equation describes the quantities of interest in the resolved scale. The contribution of Sub-Grid Scale (SGS) quantities to the solution is governed by the SGS stress term σ^{res}, which in the aforementioned context takes the form of:

$$\sigma^{\mathrm{res}}_{\mathrm{jk}} = \overline{\rho}\left(\widetilde{u}_{\mathrm{j}}\widetilde{u}_{\mathrm{k}} - \widetilde{u_{\mathrm{j}}u_{\mathrm{k}}}\right) \ . \tag{1.7}$$

This SGS stress in Eq.(1.7) is unclosed and requires modeling. This is where SGS models come into play. In the classical form of constant coefficient Smagorinsky SGS model, the Reynolds stress part ($\mathcal{T}_{\mathrm{ij}} = \widetilde{u_{\mathrm{i}}u_{\mathrm{j}}} - \widetilde{u}_{\mathrm{i}}\widetilde{u}_{\mathrm{j}}$) is decomposed into two parts, and the traceless component of it ($\mathcal{T}^{\mathrm{d}}_{\mathrm{ij}}$)is defined by:

$$\mathcal{T}^{\mathrm{d}}_{\mathrm{ij}} = \mathcal{T}_{\mathrm{ij}} - \frac{1}{3}\mathcal{T}_{\mathrm{kk}}\delta_{\mathrm{ij}}. \tag{1.8}$$

Then $\mathcal{T}_{\mathrm{ij}}^{\mathrm{d}}$ is modeled by a so called eddy viscosity model:

$$\mathcal{T}_{\mathrm{ij}}^{\mathrm{d}} = -2\nu_{\mathrm{t}} \cdot \widetilde{S_{\mathrm{ij}}} = -2(C_{\mathrm{s}}\Delta)^2|\widetilde{S}|\widetilde{S_{\mathrm{ij}}}, \tag{1.9}$$

where $\widetilde{S_{\mathrm{ij}}}$ is the filtered strain-rate tensor. It is defined as:

$$\widetilde{S_{\mathrm{ij}}} = \frac{1}{2}\left(\frac{\partial \widetilde{u_{\mathrm{i}}}}{\partial x_{\mathrm{j}}} + \frac{\partial \widetilde{u_{\mathrm{j}}}}{\partial x_{\mathrm{i}}}\right) - \frac{\delta_{\mathrm{ij}}}{3}\widetilde{u_{\mathrm{kk}}}, \tag{1.10}$$

and $|\widetilde{S}|= \sqrt{2\widetilde{S_{\mathrm{ij}}}\widetilde{S_{\mathrm{ij}}}}$ is its norm. Additionally, Δ in Eq.(1.9) is the filter size (normally the grid size) and C_{s} is the Smagorinsky constant. The Smagorinsky constant takes the value between 0.1 and 0.3 in various early works, and it was found that its value is important in obtaining accurate predictions. Hence later a model that dynamically calculates the optimum value of C_{s} was developed [17]. The basic idea of this dynamic Smagorinsky SGS model is to apply another test filter on top of the LES filter. The optimized Smagorinsky constant is one that can minimize the difference between resolved and modeled values of a predefined identity (often called the Germano identity). Details of this model and its procedures can be found in the paper by Germano et al. [17].

1.5 Flamelet/Progress Variable Model

Numerical simulation of turbulence is already a daunting task to do, simulating turbulent reacting flows just adds another level of complexity. The chemistry of reacting flows are governed by different time and length scales than those of the flow, and more importantly, adheres to different physical laws than the governing equations of fluid mechanics. Coupling reaction with fluid flow has hence been a difficult problem.

As aforementioned, one of the challenges in simulating reacting flows is that the chemical scales are much smaller than that of the flow. Simply increasing the temporal and spacial resolution of the entire simulation is impractical and ill-advised, for one then needs to resolve scales that are so small that it would render simulating any realistic geometry impossible. Hence it is desirable, in some appropriate circumstances, to develop a model that can represent the effect of chemical reactions in the existing computational framework. In the context of LES, this comes down to representing the source terms of different variables contributed by chemical reactions in the filtered grid. Specifically, we would like to know:

$$\widetilde{\dot{\boldsymbol{\omega}}}(\boldsymbol{Y}, t),$$

where $\dot{\boldsymbol{\omega}}$ is the source term in transport equations, $\boldsymbol{Y}$ are the mass fractions of all relevant species and t is the time coordinate.

One of the models for this term is the FPV model [18, 19]. In its simplest case, we assume that the species concentration space can be represented by two scalars. The first one is called the mixture fraction Z, which originates from the concept of "mixedness" of fuel and oxidizer in a pure non-premixed flame, defined as the mass fraction of the fuel stream in a mixture. The second scalar is called the progress variable C, which is usually defined as a linear combination of the mass fractions of selected species. It is related to the local stretch rate of the flame, or in other words, the reactivity of the flame. Then we can represent the un-filtered source terms as:

$$\dot{\boldsymbol{\omega}}(Z, C),$$

and the functional relationship can be solved by laminar flame solutions. However, in LES we do not have the instantaneous value of Z and C, and we do not explicitly need instantaneous source terms. Instead, we need the filtered version of all these quantities so that we can perform calculations. Issues arise here because:

$$\widetilde{\dot{\boldsymbol{\omega}}} \neq \dot{\boldsymbol{\omega}}(\widetilde{Z}, \widetilde{C}).$$

To account for the differences between these two terms, the presumed PDF approach was proposed. The basic idea of the presumed PDF is to assume that turbulence does not destroy the flame structure, the flame sheet is so thin that it is well within a LES cell. So there are a large amount of flamelets in each LES cell, but statistically they follow the same PDF determined by the resolved mixture fraction and progress variable, i.e.:

$$\widetilde{\dot{\boldsymbol{\omega}}} = \iint \dot{\boldsymbol{\omega}}(Z, C)\widetilde{P}(Z, C) dZ dC. \tag{1.11}$$

The probability density function P is a function of the filtered mixture fraction $\widetilde{Z}$ and the filtered progress variable $\widetilde{C}$. The details of this model and the choices of PDF will be detailed in section 2.3.

1.6 LASER Diagnostic Methods

No theory or model can stand by itself without the validation by experimental data. This is especially important in turbulent combustion where a closed form analytical solution is not available in most cases. One key feature of turbulent flow is that it is very sensitive to boundary conditions, hence accurate assessment of flow variables in an experiment should always refrain from perturbing the flow in any sense. The usage of LASER based diagnostic tools facilitated such needs. Not only is it non-intrusive, LASER diagnostics are also normally time and spacial resolving, due to the short and strong pulses of current LASER systems. Two of the commonly used LASER diagnostic methods are Particle Image Velocimetry (PIV) and Planar Laser Induced Fluorescence (PLIF).

1.6.1 Particle Image Velocimetry

The method of Particle Image Velocimetry (PIV) is used to measure the velocity vectors in 2D or 3D space inside a flow. Here we take 2D PIV as an example. In a PIV experiment, the flow is first seeded with small inert particles (solid or liquid). Two successive pulses of LASER sheet are fired and their LASER light will be reflected by the particles. The reflected light is captured by detecting devices (most commonly cameras), and images of particles (seen as small dots in the picture) will be generated in two successive frames, as shown in figure 1.3 (frame 1 and 2).

Using statistical tools, the same particle in each frame is identified. From this information, the movement of the particle during the time between two frames(Δt) is determined. Hence the velocity vector can be calculated, as shown in figure 1.3d.

Several factors are very important in determining the accuracy of a PIV experiment. The first one is the particle size. If the size is too large, then the particles can not closely follow the stream lines of the flow. If the size is too small, than not enough signal can be picked up by the detection devices. Another factor is the inter-frame time Δt. If it is too short, than the relative movements of particles in the two frames will be too small. Due to the limited resolution of digital cameras, this will create large uncertainties in the vector calculations. In the meantime, if the inter-frame time is too long, then a big portion of particles in the 1st frame will have already left the camera field of view when the second frame is shot. This would result in a loss of statistical correlations, thus affecting the accuracy of the calculation. There are a wide range of references that are dedicated to the discussion of this technique, interested readers are referred to these resources [20, 21].

(a) 1st Frame (b) 2nd Frame (Δt later)

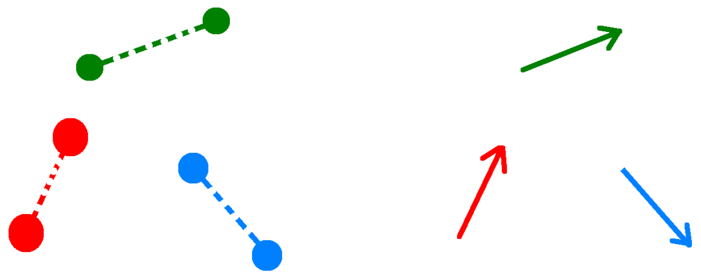

(c) Two frames superimposed (d) Resulting velocity vectors

Figure 1.3: PIV method schematics

1.6.2 Planar Laser Induced Fluorescence

The Planar Laser Induced Fluorescence (PLIF) method is usually utilized to measure the species concentration field in a 2D space. The physical foundation of this method lies in the excitation of certain energy states of a targeted specie with LASER light. The molecules of the targeted specie would then enter an excited energy state. Later these excited molecules would relax to a lower energy state spontaneously, emitting light in the process. With careful filtering of the light, a camera can capture the emitted light. Based on the strength of the received signal at each spacial location in a frame, the concentration field of that specie can then be calculated.

Figure 1.4 shows the spectrum of the returned signal emitted by formaldehyde molecules (CH_2O) when excited by LASER light at a wavelength of 355 nm. We can see that most of the returned signal have wavelengths within the range of 400 nm to 500 nm. Hence in experiment if an optical high-pass filter that has a cut-off frequency somewhere between 355 nm and 400 nm is placed in front of the camera, then the influences of the incident LASER light can be minimized. Relative distribution of formaldehyde concentration is proportional to the returned signal strength at each location of a planar image (before light saturation). Details of this technique can be

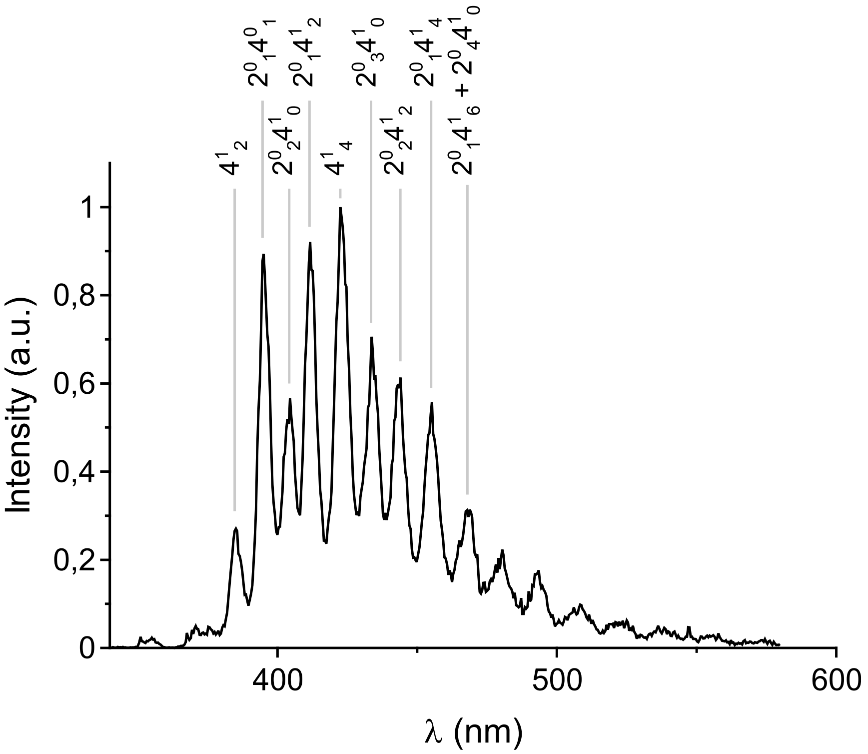

Figure 1.4: Spectrum of fluorescence signals retuned by CH_2O excited at 355nm [2]

found in reference [22].

1.7 Goals of This Work

The scope of this thesis is to advance the understanding of partially premixed combustion through numerical, theoretical, and experimental methods. Specifically, the current states of the high fidelity as well as low order model for partially premixed combustion are assessed. Improvements and extensions to these models are proposed, and the validity of these modifications are assessed by the comparison with experimental data. Specifically, the goals of this work are:

- To access the validity of the current state-of-the-art turbulent combustion model, the Flamelet/Progress Variable (FPV) model, on the partially premixed combustion regime;
- To extend the existing FPV model if needed to improve simulation results in this regime.
- To propose a reduced order model of combustion instability in confined combus-

tion devices and to assess its validity on a model combustor when geometrical parameters, equivalence ratios, and mass flow rates are changed.

- To explore the driving mechanism of instability under the framework of the proposed reduced order model, supported by the experimental data of high-speed laser diagnostic measurements.

1.8 Thesis Outline

To achieve the aforementioned goals, this works is organized as follows:

In chapter I we have stated the motivation to the current research topic. Concepts relevant to this work are briefly introduced, with related references. The specific goals of this work and our procedures to achieve these goals are stated in this section.

In chapter II we will fist look into a high fidelity numerical model for partially premixed combustion. The model of interest here is the Flamelet/Progress Variable (FPV) model. It is put into the context of Large Eddy Simulation (LES) to simulate the Sydney Piloted Premixed Jet Burner (PPJB), which is a three stream partially premixed burner. One important part of the model, the presumed PDF, is extended and tested. Simulation results are compared with experimental data provided by Dr. Dunn [3] in all four operating cases, each with a different jet velocity. The simulation results generally agree well with the experimental data, but certain short-comings are also noticed. This assessment provided confidence in the current model, and also pointed out where future improvements of this FPV model can be pointed.

In chapter III we change our gear from one of the most complex numerical models stated in chapter II to some of the most concise models in partially premixed combustion. Here we explore the reduced order model for combustion instabilities in confined combustion devices. Combustion instability is one of the key issues that hinder the wide applications of partially premixed combustion technologies. It is complex in nature, due to the interactions between turbulence, chemistry, and acoustics. Our experience in dealing with an extensive computational model like the FPV model has taught us the difficulty in applying those models in real world environment. Hence we appreciate the advantages of a simple and first-oder-accurate model in understanding such a complex physical process. Several existing reduced order models are first surveyed. It is found that none of the models are very applicable to a real engine operating environment. Hence a Modular Reduced-order Model Framework (MRMF) based on Helmholtz analysis of a series of connected chambers are proposed. The advantage of the unique modular approach of the proposed framework is discussed.

Then the derivation of governing equations under the proposed framework on a simplified four element geometry is presented.

The Modular Reduced-order Model Framework (MRMF) proposed in chapter III has to be verified with experimental data to assess its validity. The platform for this verification is chosen to be the *Deutsches Zentrum für Luft- und Raumfahrt*, German Aerospace Center (DLR) Gas Turbine Model Combustor (GTMC). It strikes a very good balance between the level of realistic complications and easiness of the applications of diagnostic tools. In chapter IV, the basic information and parameters related to GTMC are first introduced. Then previous measurements conducted both at DLR and at the University of Michigan are surveyed. Through multi-point pressure measurements, it is found out that GTMC does satisfy the basic assumptions of this model, and the model predictions should be applicable to this setup. The rest of this chapter is dedicated to the assessment of the capability of MRMF to predict and explain a series of phenomena related to combustion instabilities in GTMC when flow and fueling parameters are changed. It is found that under appropriate input parameters, our proposed model is capable of providing satisfactory predictions and explanations for experimental observations.

Even though pressure measurements can provide information on the strength and frequency of the combustion instability in GTMC, they lack the spatial and temporal resolutions needed to assess some specific assumptions in our reduced order model. Hence in chapter V we present our high speed laser diagnostics to investigate the interactions between pressure, heat release, and velocity fluctuations under various operating conditions in GTMC. We first introduce the experimental setup and calibration of the simultaneous 4 kHz PIV-PLIF-pressure measurements. Sharp edges in formaldehyde PLIF images are treated as the marker of heat release region. The frequency spectrums of pressure, heat release, radial, and axial velocity in rich, lean, stoichiometric, and reduced flow rate conditions are presented and discussed. The significance of these results in connection with our model assumptions of MRMF is also discussed.

Finally, this thesis closes with chapter VI, which includes conclusions and summaries of the entire work. Recommendations for future work are also provided.

CHAPTER II

Numerical Study of Partially Premixed Combustion – Large Eddy Simulation of the Piloted Premixed Jet Burner (PPJB)

2.1 Introduction

As mentioned in section 1.2, the implementation of premixed and partially-premixed combustion technologies in modern gas turbine engines has the potential of reducing pollutant emissions and increasing overall combustor performance [23]. An example of using premixed combustion strategies in aviation gas turbine engines is GE's Twin Annular Premixed Swirl (TAPS) combustor [24, 25]. This combustor utilizes a diffusion flame as pilot, and the main heat-release is facilitated by an outer swirl-injector that is operated in a lean premixed combustion mode. The characterization of flame-stabilization and heat-release mechanisms in these complex flow environments introduces modeling challenges that require addressing to improve existing modeling capabilities for such practically relevant combustion conditions.

Of interest to the current study is the Sydney Piloted Premixed Jet Burner (PPJB) that was investigated by Dunn et al. [3, 26, 27]. This burner configuration was designed with the objective to resemble conditions relevant to partially-premixed gas turbine combustors, but without the additional complexity of geometrical confinement, swirl, or recirculation. In this burner, a central fuel jet is stabilized by a pilot consisting of a stoichiometric methane/air mixture. The burner is embedded in an outer coflow of hot reaction products that are generated by combusting a lean hydrogen/air mixture. In this experiment, a series of operating conditions are investigated, in which the jet exit velocity is successively increased while keeping all other conditions identical.

This burner configuration has been modeled by several research groups. Rowinski & Pope [28] employed a RANS-PDF method, and performed comprehensive studies to assess the sensitivity of inlet boundary conditions, turbulence models, mixing models, heat losses, and chemical mechanisms. They highlighted the significance of finite-rate chemistry effects, and identified the mixing model as source for model deficiencies.

Duwig et al. [29] investigated the importance of the complexity of the reaction mechanisms on the model predictions. They found that global reaction mechanisms are not sufficient to describe the flame-structure, and at least a 20-species skeletal mechanism is required to capture the measurements. They also stated that stabilization of the flame relies on the intense small-scale mixing between pilot and jet stream. This agrees with the argument of Dunn et al. and Rowinski & Pope that the turbulence/flame interaction plays a critical role in this burner configuration.

The interested reader is also referred to colloquia on PPJB-modeling efforts of different groups that were focus areas of recent TNF-workshops [30, 31].

The objective of this chapter is to assess the capability of a flamelet-based LES combustion model to predict this piloted jet burner. To this end, a three-stream Flamelet/Progress Variable (FPV) formulation is considered, which has previously been applied to low-Damköhler number combustion [32, 33]. The mathematical model and developments pertaining to the present application are presented in section 2.3. A prior model analysis is performed in section 2.4, examining relevant modeling assumptions regarding the applicability of this three-stream formulation to partially-premixed combustion regimes, the statistical representation of the scalar mixing, and the joint PDF-closure. Following this investigation, the model is employed to the simulation of the four cases PM1-{50,100,150,200}, and modeling results are compared with experimental data in section 2.6. The chapter finishes with conclusions.

2.2 Experimental Setup

A schematic of the piloted premixed jet burner is shown in Fig. 2.1 [3]. The burner consists of three coaxial streams. A fuel-lean methane/air mixture at room temperature is supplied by the central stream. The nozzle exit diameter of the central fuel pipe is $D_{\text{ref}} = 4$ mm. The flame is stabilized by a pilot-stream which consists of reaction products from a stoichiometric methane/air mixture. The pilot is surrounded by a hot coflow of products from a burned hydrogen/air mixture. The coflow-stream isolates the flame from the surrounding air-stream to eliminate potential quenching and dilution effects [3].

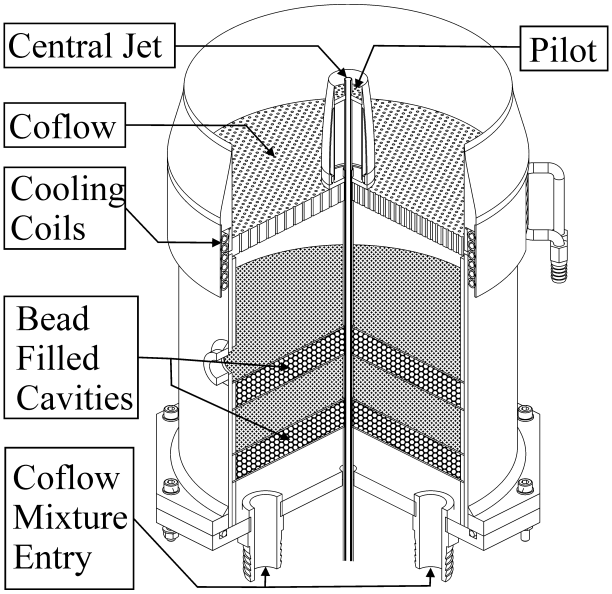

Figure 2.1: Schematic of the piloted premixed jet burner [3].

While keeping all other conditions fixed, the jet exit velocity, U_J, was discretely varied between 50 m/s to 200 m/s (in increments of 50 m/s). The increased jet-exit velocity leads to higher strain-rates, resulting in increasing levels of extinction and re-ignition. Species were measured by simultaneous Planar Laser Induced Fluorescence (PLIF) imaging, and Laser Doppler Velocimetry (LDV) was used for measuring the velocity field. Measurements of major species of fuel, oxygen, product species and hydroxyl radicals are reported. For reference, operating conditions and parameters for all cases are summarized in Tab. 2.1.

Variable	Unit	Jet	Pilot	Coflow
D	mm	4.0	23.5	197.0
U	m/s	Varies	5.2	3.98
T	K	290	2274	1493
Mixture	–	CH_4-Air	CH_4-Air	H_2-Air
ϕ	–	0.5	1.0	0.43

Case	U_J [m/s]	Re	Ka
PM1-50	50	12500	100
PM1-100	100	25000	1600
PM1-150	150	37500	2500
PM1-200	200	50000	3500

Table 2.1: Operating conditions for the piloted premixed jet burner [3].

2.3 Mathematical Formulation

This section discusses the mathematical formulation and key assumptions of the present model. In the present work, we model the combustion in the PPJB as partially-premixed combustion regime that we represent using a steady flamelet formulation. To confirm that this model-representation is adequate, a prior model analysis is performed in section 2.4.

2.3.1 Three-stream Flamelet/Progress Variable (FPV) Model

In the present study, a three-stream Flamelet/Progress Variable (FPV) combustion model [32, 33] is extended and applied to the piloted jet burner. In this model, the turbulent flame is described from the solution of one-dimensional laminar flamelets [34, 1]:

$$-\frac{\chi_{Z_1}}{2}\frac{\partial^2 \boldsymbol{\phi}}{\partial Z_1^2} = \dot{\boldsymbol{\omega}} \,, \tag{2.1}$$

where Z_1 is the mixture fraction, $\boldsymbol{\phi}$ is the vector of all species mass fractions $\boldsymbol{Y}$ and temperature T, and $\boldsymbol{\omega}$ denotes their respective source terms. The scalar dissipation rate is denoted by χ_{Z_1} with $\chi_{Z_1} = 2\alpha|\nabla Z_1|^2$, and α is the molecular diffusivity. A unity Lewis-number approximation is employed. Solutions to this equation are obtained with appropriate boundary conditions, namely at $Z_1 = 1$ (fuel stream, denoted by $\boldsymbol{\phi}^{\mathrm{F}}$) and $Z_1 = 0$ (oxidizer stream, denoted by $\boldsymbol{\phi}^{\mathrm{O}}$). In the PPJB-configuration, the condition in the fuel stream is obtained from the reported experimental data. To differentiate between the compositions in both oxidizer streams (namely pilot and coflow streams; see Fig. 2.1), an additional conserved scalar is introduced. This scalar is denoted by Z_2 and is referred to as "secondary mixture fraction", following the definition that $Z_2 = 0$ in the pilot and $Z_2 = 1$ in the coflow. Both mixture-fractions, Z_1 and Z_2, can be related to the elemental mass fractions through the following expression:

$$\begin{bmatrix} Z_1 \\ Z_2 \end{bmatrix} = \boldsymbol{A}^{-1} \begin{bmatrix} y_{\mathrm{C}} - y_{\mathrm{C}}^{\mathrm{O}(0)} \\ y_{\mathrm{H}} - y_{\mathrm{H}}^{\mathrm{O}(0)} \end{bmatrix} \,, \tag{2.2}$$

with

$$\boldsymbol{A} = \begin{bmatrix} y_{\mathrm{C}}^{\mathrm{F}} - y_{\mathrm{C}}^{\mathrm{O}(0)} & y_{\mathrm{C}}^{\mathrm{O}(1)} - y_{\mathrm{C}}^{\mathrm{O}(0)} \\ y_{\mathrm{H}}^{\mathrm{F}} - y_{\mathrm{H}}^{\mathrm{O}(0)} & y_{\mathrm{H}}^{\mathrm{O}(1)} - y_{\mathrm{H}}^{\mathrm{O}(0)} \end{bmatrix} \,, \tag{2.3}$$

where the superscripts "O(0)" and "O(1)" refer to the pilot ($Z_2 = 0$) and the coflow stream ($Z_2 = 1$). The elemental mass fractions of carbon and hydrogen are denoted by y_C and y_H, respectively. In this context it is noted that the expressions for Z_1 and Z_2 are identical to the variables ξ_1 and ξ_3, defined by Dunn [35].

With the variables defined above, the solution of the flamelet equations, Eq. (2.1), can then be written as:

$$\boldsymbol{\phi} = \boldsymbol{\phi}(Z_1, Z_2, \chi_{Z_{1,\mathrm{ref}}}) \; , \tag{2.4}$$

where $\chi_{Z_{1,\mathrm{ref}}}$ is the scalar dissipation rate at a reference mixture fraction $Z_{1,\mathrm{ref}}$. In the present study, this reference mixture fraction is taken as 0.75. Instead of parameterizing $\boldsymbol{\phi}$ in terms of $\chi_{Z_{1,\mathrm{ref}}}$, a reaction progress variable C is introduced. It is defined as [33]:

$$C = Y_{\mathrm{CO}_2} + Y_{\mathrm{H}_2\mathrm{O}} + Y_{\mathrm{CO}} + Y_{\mathrm{H}_2} \; , \tag{2.5}$$

which has been shown to provide a unique parameterization of the flamelet state-space [33]. In this way the entire solution space of the steady flamelet equations can be represented as:

$$\boldsymbol{\phi} = \boldsymbol{\phi}(Z_1, Z_2, C) \; . \tag{2.6}$$

After parameterizing all flamelet-solutions by Z_1, Z_2, and C, it was found that the convex hull of the FPV state-space represents a triangular prism in which the base is spanned by an isosceles right triangle along the Z_1 and Z_2 coordinates.

2.3.2 Presumed PDF Closure

In the presumed Probability Density Function (PDF) model, the interaction between the reaction chemistry and turbulence is modeled by a PDF. The thermodynamic quantities that were obtained from the laminar flamelet equations are convoluted over the entire PDF support to yield a chemical library that is used in the simulation:

$$\widetilde{\boldsymbol{\phi}} = \iiint \boldsymbol{\phi}(Z_1, Z_2, C)\widetilde{P}(Z_1, Z_2, C)dZ_1\, dZ_2\, dC \; . \tag{2.7}$$

In the context of LES, the PDF is denoted as $\widetilde{P}(Z_1, Z_2, C)$, where the tilde denotes a Favre-averaged quantity. Using Bayes' theorem, the joint PDF can be written as $\widetilde{P}(Z_1, Z_2)P(C|Z_1, Z_2)$, and the conditional PDF of the progress parameter has been modeled as a Dirac-delta function [36, 19]. More detailed closure models, such as the statistically most-likely distribution or a beta-PDF closure can also be employed [37]. This, however, has not been considered here and is subject of future work. The treatment of the joint PDF for Z_1 and Z_2 will be discussed next.

In a conventional two-stream problem, the beta distribution has been shown to provide an adequate description of the sub-grid scale mixing [38, 39, 37]. The beta distribution has the following functional form:

$$\widetilde{P}(Z_1) = \beta(Z_1) = \frac{\Gamma(a_1 + a_0)}{\Gamma(a_1)\Gamma(a_0)} Z_1^{a_1 - 1}(1 - Z_1)^{a_0 - 1} \ , \tag{2.8}$$

where the coefficients a_0 and a_1 are determined by the mean and variance of the independent variable, and Γ denotes the Gamma function.

By extending this closure formulation to a three-stream system, we will assume that the marginal PDF of the secondary mixture fraction Z_2 also follows a beta distribution, resulting in the constraints:

$$\beta(Z_1) = \int_0^1 \widetilde{P}(Z_1, Z_2) dZ_2 \ , \tag{2.9a}$$

$$\beta(Z_2) = \int_0^1 \widetilde{P}(Z_1, Z_2) dZ_1 \ , \tag{2.9b}$$

on the support

$$Z_1 \geq 0 \ , \qquad Z_2 \geq 0 \ , \qquad Z_1 + Z_2 \leq 1 \ . \tag{2.10}$$

It can be shown that the Dirichlet distribution [40, 41] satisfies these requirements. The Dirichlet distribution is a multivariate generalization of the beta distribution, and has the following definition:

$$\widetilde{P}(Z_1, Z_2) = \frac{\Gamma\left(a_0 + a_1 + a_2\right)}{\Gamma(a_0)\Gamma(a_1)\Gamma(a_2)} Z_1^{a_0 - 1}(1 - Z_1 - Z_2)^{a_1 - 1} Z_2^{a_2 - 1} \ . \tag{2.11}$$

where the coefficients a_0, a_1, and a_2 are determined as function of $\widetilde{Z_1}$, $\widetilde{Z_2}$, and $\widetilde{Z_1''^2}$:

$$a_0 = \left(\frac{\widetilde{Z_1}}{\widetilde{Z_1''^2}} \left(1 - \widetilde{Z_1}\right) - 1 \right) \widetilde{Z_1} \ , \tag{2.12a}$$

$$a_1 = \left(\frac{\widetilde{Z_1}}{\widetilde{Z_1''^2}} \left(1 - \widetilde{Z_1}\right) - 1 \right) (1 - \widetilde{Z_1} - \widetilde{Z_2}) \ , \tag{2.12b}$$

$$a_2 = \left(\frac{\widetilde{Z_1}}{\widetilde{Z_1''^2}} \left(1 - \widetilde{Z_1}\right) - 1 \right) \widetilde{Z_2} \ , \tag{2.12c}$$

and the variance of the secondary mixture fraction and covariance are evaluated as:

$$\widetilde{Z_2''^2} = \frac{\widetilde{Z}_2(1-\widetilde{Z}_2)}{\widetilde{Z}_1(1-\widetilde{Z}_1)}\widetilde{Z_1''^2}, \tag{2.13a}$$

$$\widetilde{Z_1''Z_2''} = \frac{\widetilde{Z}_2\widetilde{Z_1''^2}}{1-\widetilde{Z}_1}. \tag{2.13b}$$

With these formulations, the Favre-averaged library of the FPV model can then be written as:

$$\widetilde{\boldsymbol{\phi}} = \widetilde{\boldsymbol{\phi}}(\widetilde{Z}_1, \widetilde{Z_1''^2}, \widetilde{Z}_2, \widetilde{C}) \ , \tag{2.14}$$

in which $\widetilde{C}$ is used for parameterizing the reaction progress coordinate. This library is generated by following the process:

1. laminar flamelet equations with different oxidizer-side boundary conditions defined by Z_2 values varied from of 0 to 1 are solved using the software FlameMaster [42];
2. flamelets are sorted according to their Z_2 and C values and are mapped to a universal three dimensional grid of Z_1, Z_2, and C;
3. a four dimensional flamelet library with indices of $\widetilde{Z}_1$, $\widetilde{Z_1''^2}$, $\widetilde{Z}_2$, and $\widetilde{C}$ is constructed, the value of a range of thermo-chemical variables are contained in each cell of this library, generated by the convolution of the table generated in step 2 with the prescribed PDF using Eq.(2.7).

The three-stream FPV model requires the solution of transport equations for $\widetilde{Z}_1$, $\widetilde{Z_1''^2}$, $\widetilde{Z}_2$, and $\widetilde{C}$, so that the required thermo-chemical variable can be looked up from the aforementioned flamelet library using $\widetilde{Z}_1$, $\widetilde{Z_1''^2}$, $\widetilde{Z}_2$, and $\widetilde{C}$ as indices. The governing equations of these variables are presented in the next section.

2.3.3 Governing Equations

In addition to the solution of the conservation equations for mass and momentum, the low-Mach number, variable-density LES-formulation requires the solution of four additional transport equations for the first two moments of mixture fraction, as well as the Favre-filtered secondary mixture fraction and progress variable. These modeled equations take the following form:

$$
\begin{aligned}
\widetilde{\mathcal{D}}_t\overline{\rho} &= -\overline{\rho}\,\nabla\cdot\widetilde{\boldsymbol{u}}\,, && \text{(2.15a)}\\
\overline{\rho}\widetilde{\mathcal{D}}_t\widetilde{\boldsymbol{u}} &= -\nabla\overline{p}+\nabla\cdot\overline{\boldsymbol{\sigma}}+\nabla\cdot\boldsymbol{\sigma}^{\mathrm{res}}\,, && \text{(2.15b)}\\
\overline{\rho}\widetilde{\mathcal{D}}_t\widetilde{Z_1} &= \nabla\cdot(\overline{\rho}\widetilde{\alpha}\nabla\widetilde{Z_1})+\nabla\cdot\boldsymbol{\tau}^{\mathrm{res}}_{\widetilde{Z_1}}\,, && \text{(2.15c)}\\
\overline{\rho}\widetilde{\mathcal{D}}_t\widetilde{Z_1''^2} &= \nabla\cdot(\overline{\rho}\widetilde{\alpha}\nabla\widetilde{Z_1''^2})+\nabla\cdot\boldsymbol{\tau}^{\mathrm{res}}_{\widetilde{Z_1''^2}}-2\overline{\rho}\widetilde{\boldsymbol{u}''Z_1''}\cdot\nabla\widetilde{Z_1}-\overline{\rho}\widetilde{\chi}^{\mathrm{res}}_{Z_1}\,, && \text{(2.15d)}\\
\overline{\rho}\widetilde{\mathcal{D}}_t\widetilde{Z_2} &= \nabla\cdot(\overline{\rho}\widetilde{\alpha}\nabla\widetilde{Z_2})+\nabla\cdot\boldsymbol{\tau}^{\mathrm{res}}_{\widetilde{Z_2}}\,, && \text{(2.15e)}\\
\overline{\rho}\widetilde{\mathcal{D}}_t\widetilde{C} &= \nabla\cdot(\overline{\rho}\widetilde{\alpha}\nabla\widetilde{C})+\nabla\cdot\boldsymbol{\tau}^{\mathrm{res}}_{\widetilde{C}}+\overline{\rho}\widetilde{\omega}_C\,, && \text{(2.15f)}
\end{aligned}
$$

in which $\widetilde{\mathcal{D}}_t = \partial_t + \widetilde{\boldsymbol{u}}\cdot\nabla$ is the Favre-filtered substantial derivative. The sub-grid stresses $\boldsymbol{\sigma}^{\mathrm{res}}$ and sub-grid turbulent fluxes $\boldsymbol{\tau}^{\mathrm{res}}_{\phi}$ are modeled by the dynamic Smagorinsky model. The turbulent fluxes are modeled by a gradient transport assumption, and the residual scalar dissipation rates $\widetilde{\chi}^{\mathrm{res}}_{Z_1}$ and $\widetilde{\chi}^{\mathrm{res}}_{Z_2}$ are modeled using spectral arguments [43, 44].

2.4 Prior Model Evaluation

Prior to applying the three-stream FPV formulation to LES of the PPJB configuration, a model evaluation is performed to assess relevant model assumptions. To this end, single-point measurements at selected locations and operating conditions are used. In the following section, the representation of the reaction-chemistry in terms of the three-stream flamelet state-space is evaluated. The representation of the PDF-closure and the scalar mixing is considered in Sec. 2.4.2.

2.4.1 Assessment of Chemistry Representation

In view of the complex chemical and turbulent interactions, we first examine the applicability of the three-parameter flamelet-progress variable formulation to this burner configuration. The thermochemical state-space in this formulation is obtained from the solution of one-dimensional partially-premixed flame-structures, and the reaction chemistry is described using the GRI-mechanism 3.0 [45]. Other detailed reaction mechanisms [46, 47] have also been considered, and provide similar results with only minor differences for radical species.

2.4.1.1 Flamelet Boundary Conditions

Boundary conditions for the oxidizer streams (pilot and coflow) are determined from the knowledge about the burner operating conditions and reported measurements at the first measurement location, $x/D_{\mathrm{ref}} = 2.5$. To determine the product mixture composition in the pilot-stream, chemical equilibrium computations for the experimentally reported reactant composition (see Tabs. 2.1 and 2.2) were performed. Comparisons of the equilibrium composition with measurements at $x/D_{\mathrm{ref}} = 2.5$ showed that the experimentally determined composition in the core of the pilot stream differs from the calculations. This is illustrated in figure 2.2, showing measured species profiles for the four cases PM1-$\{50, 100, 150, 200\}$; results from the equilibrium computation are presented by dashed lines.

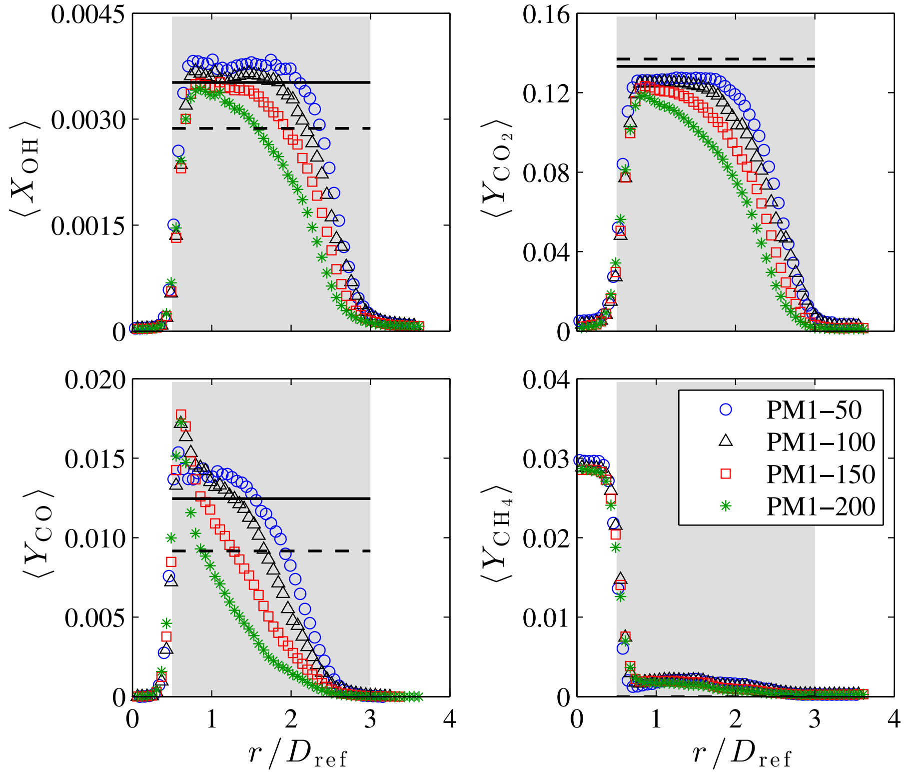

Figure 2.2: Measurements of species profiles at $x/D_{\mathrm{ref}} = 2.5$ for the cases PM1-$\{50, 100, 150, 200\}$; the shaded region indicates the pilot stream, dashed lines correspond to the computed equilibrium composition, and solid lines indicate the inlet composition that is used for all subsequent computations.

From figure 2.2 the presence of some unburned fuel in the pilot-stream and super-equilibrium composition of CO and OH can be seen. This suggests that the pilot mixture has a higher enthalpy, which can be attributed to the preheating by the outer coflow. To confirm this hypothesis, additional equilibrium computations with a specified reactant temperature of 400 K were performed. Results from this computation are shown by the solid lines in figure 2.2, providing considerably better agreement with measurements. The prevailing differences might partially be attributed to incomplete combustion and other secondary effects that are not further considered in the present investigation. The mass fractions that were prescribed as inlet conditions are summarized in Tab. 2.2.

	Jet	Pilot	Coflow
$Y_{\mathrm{N_2}}$	0.7454	0.7258	0.7581
$Y_{\mathrm{O_2}}$	0.2263	0.0055	0.1306
$Y_{\mathrm{CH_4}}$	0.0283	–	–
$Y_{\mathrm{H_2O}}$	–	0.1204	0.1112
$Y_{\mathrm{CO_2}}$	–	0.1332	–
Y_{CO}	–	0.0125	–
Y_{OH}	–	0.0022	0.0001
$Y_{\mathrm{H_2}}$	–	0.0004	–

Table 2.2: Prescribed species mass fraction composition at the inlet.

Steady-state flamelet-profiles were then computed for the specified boundary conditions in the fuel-stream. Boundary conditions in the oxidizer stream are prescribed from the solution of a mixing problem between pilot and coflow streams [32]. All thermochemical variables that are considered for this prior model evaluation are tabulated in terms of Z_1, Z_2, and C. To assess the FPV-chemistry representation, this table is accessed using data from the measurements,

$$\boldsymbol{\phi} = \boldsymbol{\phi}(Z_1^{\mathrm{Exp}}, Z_2^{\mathrm{Exp}}, C^{\mathrm{Exp}}) \,, \tag{2.16}$$

in which the independent FPV-state-space variables, denoted by the superscript "Exp," are evaluated from the single-point scatter data [3, 35].

2.4.1.2 Validity of Flamelet Assumption

For the present prior model analysis we consider the cases PM1-50 and PM1-200, representing the two extreme operating points of this burner. Scatter data at two axial locations ($x/D_{\mathrm{ref}} = \{2.5, 15\}$) and three radial locations ($r/D_{\mathrm{ref}} = \{0.7, 1.1, 2.5\}$, corresponding to the shear-layer between fuel and pilot streams, and the core of the pilot-stream; see figure 2.3) are considered. For this analysis, measurements in an interval of $\pm 0.05 D_{\mathrm{ref}}$ around the measurement location are considered. Results for

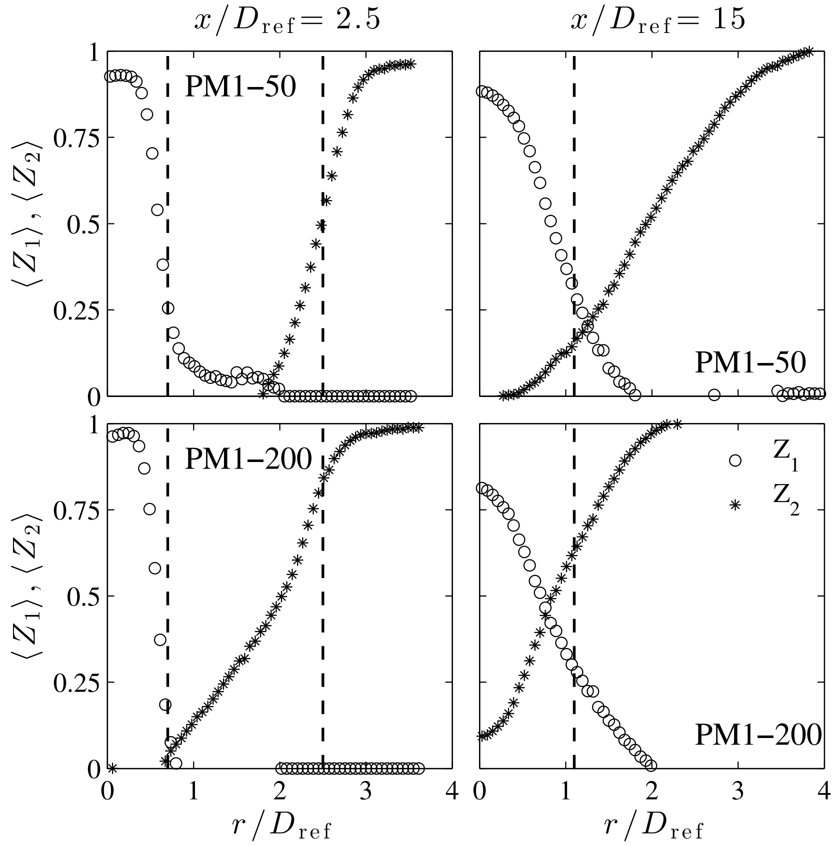

Figure 2.3: Radial profiles of measured mixture-fractions $\langle Z_1 \rangle$ and $\langle Z_2 \rangle$ for the cases PM1-50 and PM1-200. Vertical dashed lines indicate locations at which the prior PDF-model analysis is performed.

temperature, mass fraction of CO, and mole fraction of OH are compared with measurements in figure 2.4. From this comparison it can be seen that the evaluated temperature profiles from the FPV-chemistry representation are in very good agreement with experiments. The CO mass fraction, obtained from the chemistry table, is initially underpredicted at $r/D_{\mathrm{ref}} = 0.7$; however, the agreement with experimental results improves with increasing distance along the radial direction. The observed differences might be due to incomplete combustion processes, which was discussed in the context of figure 2.2. Comparisons of the OH mole fraction, shown in the bottom panels of figure 2.4, are also well predicted by the FPV-chemistry representation.

This analysis is extended and radial scatter data for temperature, Y_{CO}, and X_{OH} are evaluated from the chemistry library using the single-point measurements for Z_1, Z_2, and C as input. Results from this analysis are presented in figures 2.5, 2.6, and 2.7. From these figures, it can be seen that the mean temperature profiles from the

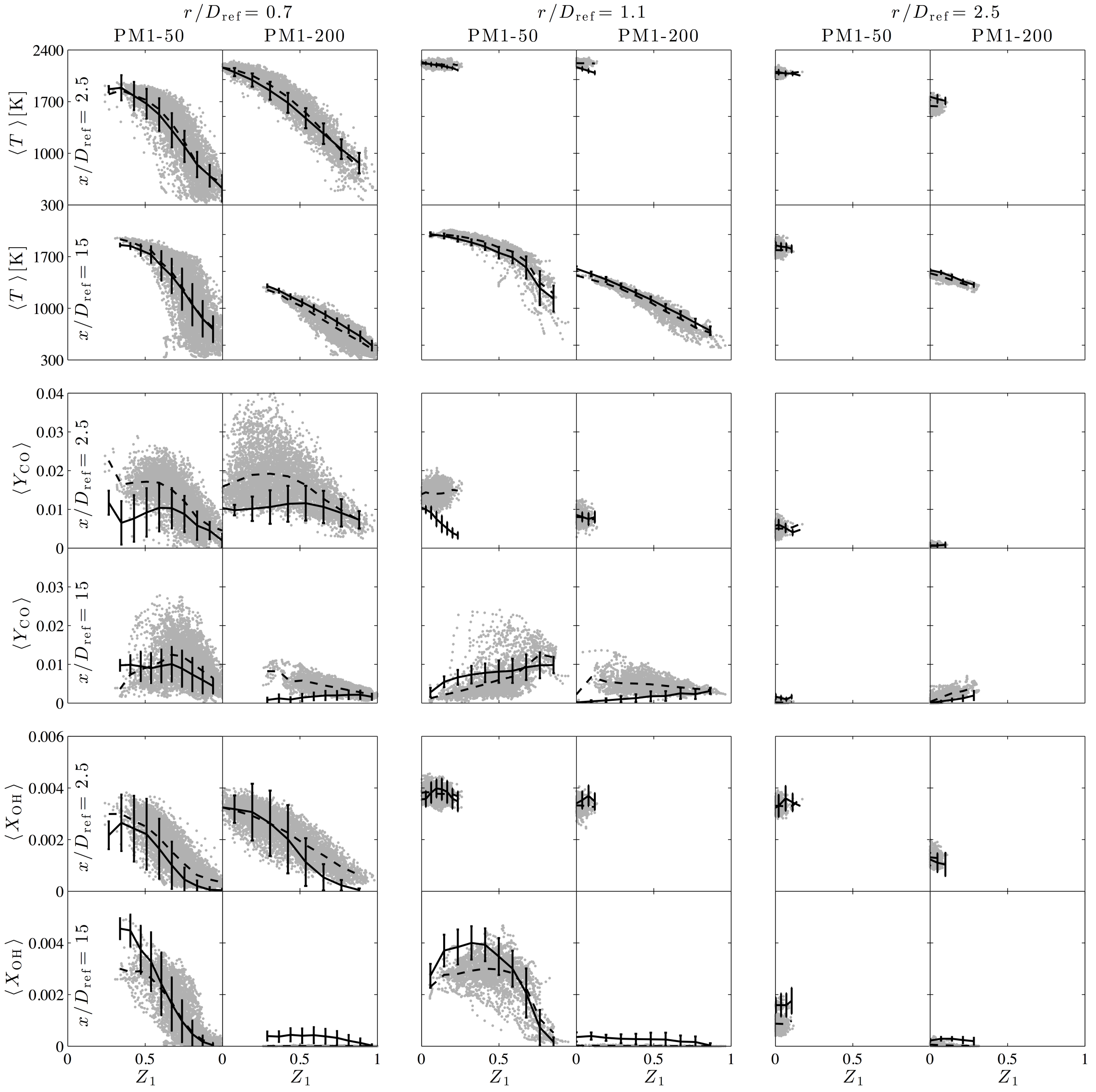

Figure 2.4: Prior model analysis comparing results for T, Y_{CO}, and X_{OH} from FPV-chemistry evaluation and experiments for the cases PM1-50 and PM1-200. Experimental scatter data are shown by gray symbols; dashed lines show conditional mean results from measurements, and solid lines are results from the prior model evaluation. Vertical bars indicate the range within one standard deviation away from the mean.

prior model analysis are in good agreement with measurements, and differences are confined to the outer shear layer-region at $x/D_{\mathrm{ref}} = 2.5$. These differences can be attributed to heat loss effects that are not included in the chemistry representation; the consideration of these effects will be addressed in Sec. 2.5.2. Except for the first measurement location for the case PM1-50, the computed CO-mass fraction profiles are in good agreement with measurements. Interestingly, the predictions for OH at $x/D_{\mathrm{ref}} = 2.5$ are in very good agreement for both cases considered. At further downstream locations, the computed X_{OH} is slightly higher, but simulation results remain within one standard deviation of the measurements.

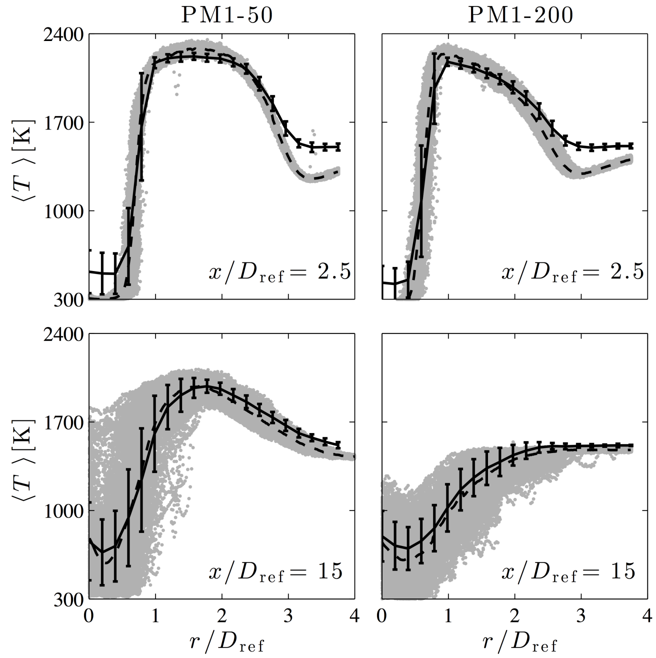

Figure 2.5: Prior model analysis comparing radial profiles for temperature, rom chemistry evaluation and experiments for the cases PM1-50 and PM1-200. Experimental scatter data are shown by gray symbols; dashed lines show conditional mean results from measurements, and solid lines are results from prior model evaluation. Vertical bars indicate the range within one standard deviation away from the mean.

2.4.1.3 Effect of Non-unity Lewis Numbers

The analysis presented in the previous section was performed under the assumption of unity Lewis number. To assess the effect of preferential diffusion, we repeat this analysis by considering flamelet-solutions that are generated for $\mathrm{Le}_i \neq 1$. Results of this investigation are presented in figure 2.8. A direct comparison with figure 2.4 shows that both flamelet libraries provide comparable results, suggesting that Lewis-number effects are small for the current model.

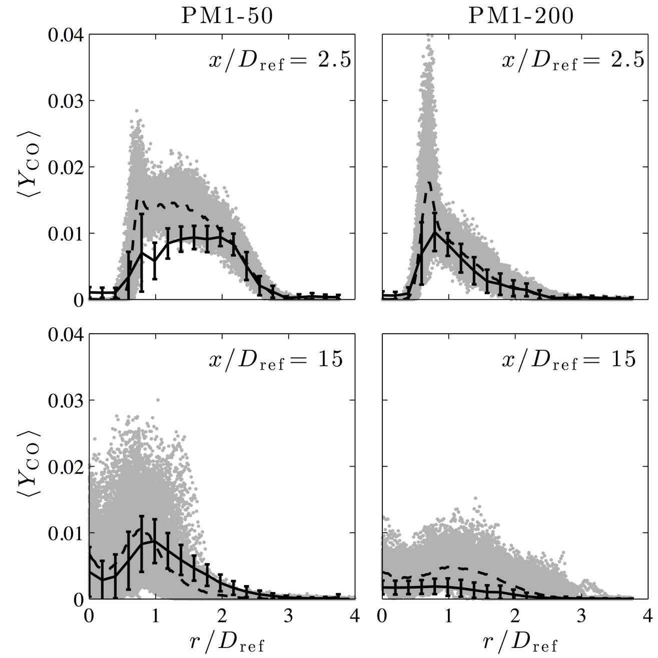

Figure 2.6: Prior model analysis comparing radial profiles for CO mass fraction, legend follows that of figure 2.5

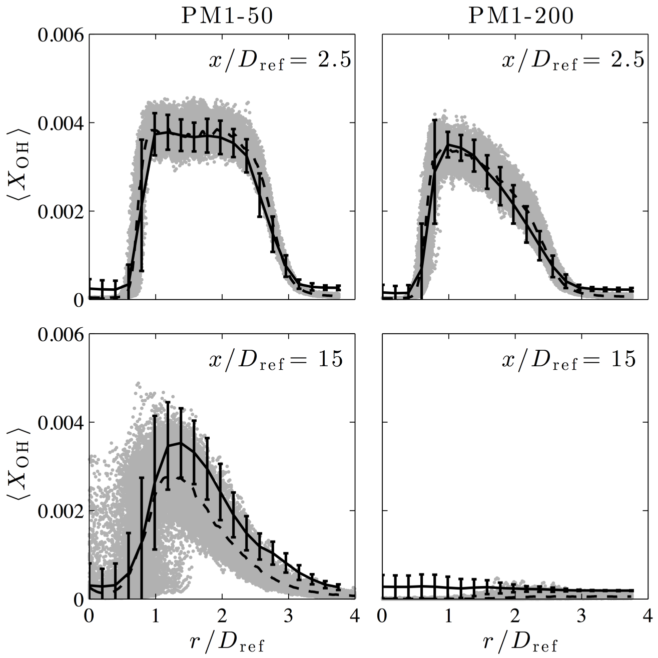

Figure 2.7: Prior model analysis comparing radial profiles for OH mole fraction, legend follows that of figure 2.5

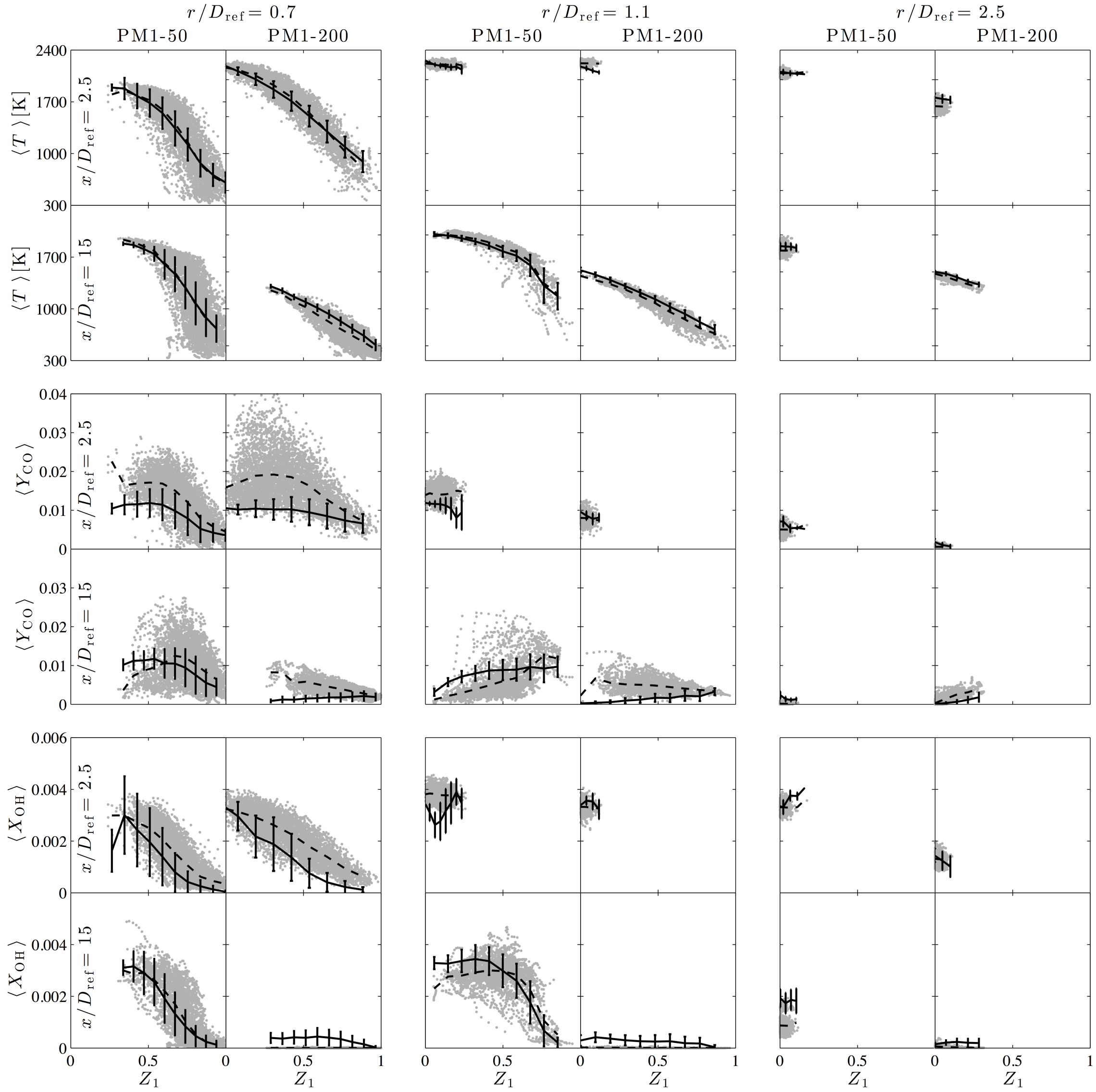

Figure 2.8: Comparison between non-unity Lewis number FPV-chemistry and experiments for the cases PM1-50 and PM1-200. Experimental scatter data are shown by gray symbols; dashed lines show conditional mean results from measurements, and solid lines are results from the prior model evaluation. Vertical bars indicate the range within one standard deviation away from the mean. Scatter data are collected in an interval of ±$0.05D_\mathrm{ref}$ around the measurement location.

2.4.2 Assessment of PDF Closure

The validity of the closure for the joint mixture fraction PDF is assessed by comparing measurements with the presumed PDF formulation that was discussed in Sec. 2.3.2. In this analysis, we focus on three distinct locations that are characteristic for the three-stream mixing dynamics. These locations and corresponding scalar mixing profiles are illustrated in figure 2.3 for the cases PM1-50 and PM1-200. The radial locations $r/D_{\mathrm{ref}} = 0.7$ and 2.5 at $x/D_{\mathrm{ref}} = 2.5$ are representative for the binary mixing between fuel–pilot and pilot–coflow, respectively. To investigate the statistical representation of the three-stream joint mixing, we also consider the measurement location at $r/D_{\mathrm{ref}} = 1.1$ and $x/D_{\mathrm{ref}} = 15$. For all cases considered, scatter data are collected in an interval of $\pm 0.05 D_{\mathrm{ref}}$ around the measurement location.

Comparisons of measured and computed PDFs for the binary mixing are presented in Figs. 2.9 and 2.10. In the experiment the mass fractions of multiple species were measured using the Raman technique. From the mass fractions of these species, the elemental mass fractions of carbon, hydrogen, and oxygen can then be determined. The mixture fractions at the experimental measurement points are calculated using Eq. (2.2). The probability distribution of these mixture fractions are plotted as the grey bars. The lines indicate the probability density functions of Beta distributions with the same mean and variance as the corresponding experiential data. It can be seen that the PDF-closure captures the shape of the marginal PDF, providing a good representation of the binary mixing.

The statistical representation of the joint mixing is analyzed by considering the location $r/D_{\mathrm{ref}} = 1.1$ and $x/D_{\mathrm{ref}} = 15$. Comparisons between measurements and simulations are illustrated in Figs. 2.11 and 2.12, and results are presented for all four operating conditions. The marginal PDFs are computed by integrating the joint PDF with respect to Z_2 and Z_1, respectively.

Marginal PDFs of Z_1 and Z_2 for all four cases are shown in figure 2.11, and it can be seen that the Dirichlet distribution provides a good representation of experimentally determined distributions. From this comparison, effects of different operating conditions on the scalar mixing properties can be observed. In particular, the direct comparison among the four cases in figure 2.11 shows an enhanced mixing and a reduction in the skewness with increasing jet-exit velocity.

The effect of the enhanced mixing intensity can also be seen by comparing joint PDFs in figure 2.12. Shown on the left are experimental data and computed results from the presumed Dirichlet distribution are illustrated on the right. The following observations can be made: First, a qualitative comparison with experimental data indicates that the Dirichlet distribution captures the main features of the PDF. To quantify differences in the PDF-support and spreading in compositional space, we compare computed and experimentally determined covariances. Computed values are reported in figure 2.12, and the direct comparison shows that the measured covariance is skewed towards slightly larger negative values. The second observation is

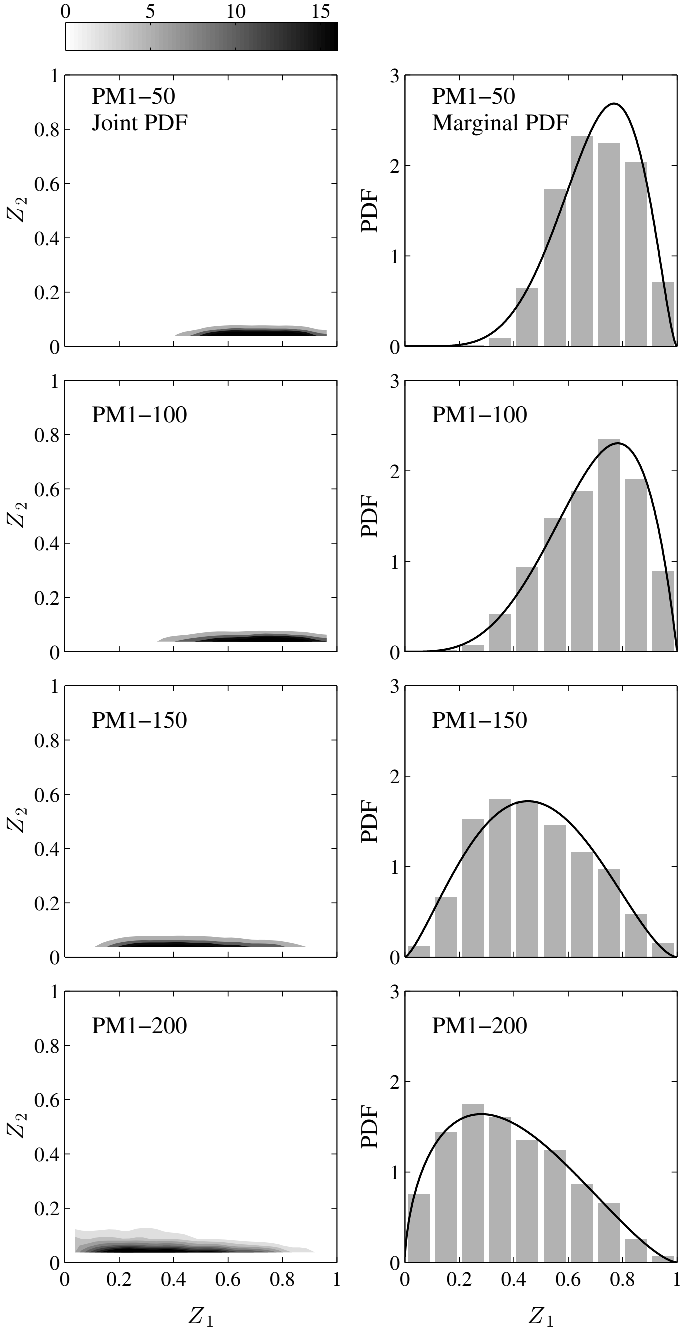

Figure 2.9: Scalar mixing distributions at $r/D_{\mathrm{ref}} = 0.7$ and $x/D_{\mathrm{ref}} = 2.5$, showing (left) measured joint PDFs and (right) comparison between measured and computed marginal PDF for $P(Z_1)$. Experimental data is represented by bars and computed results are shown by solid lines.

in regard to the mixing, confirming that the mixing effect increases with increasing jet-exit velocity. The primary reason for this is a larger entrainment effect as U_{J} increases, so that the pilot-stream is rapidly displaced by coflow-mixture. This en-

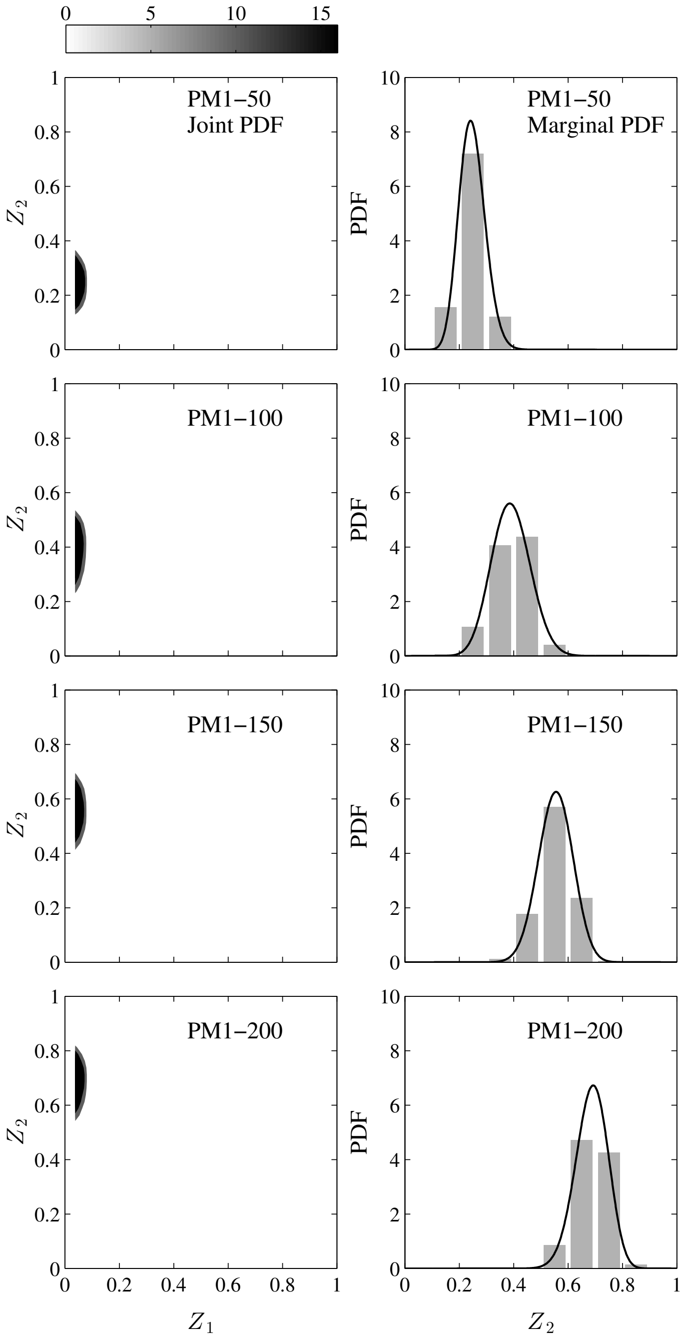

Figure 2.10: Scalar mixing distributions at $r/D_{\mathrm{ref}} = 2.5$ and $x/D_{\mathrm{ref}} = 2.5$, showing (left) measured joint PDFs and (right) comparison between measured and computed marginal PDF for $P(Z_2)$. Experimental data is represented by bars and computed results are shown by solid lines.

hanced entrainment can also be seen in figure 2.20, where a comparison of computed temperature fields for all four cases is provided. There the influences of pilot are reduced as the central jet speed is increased.

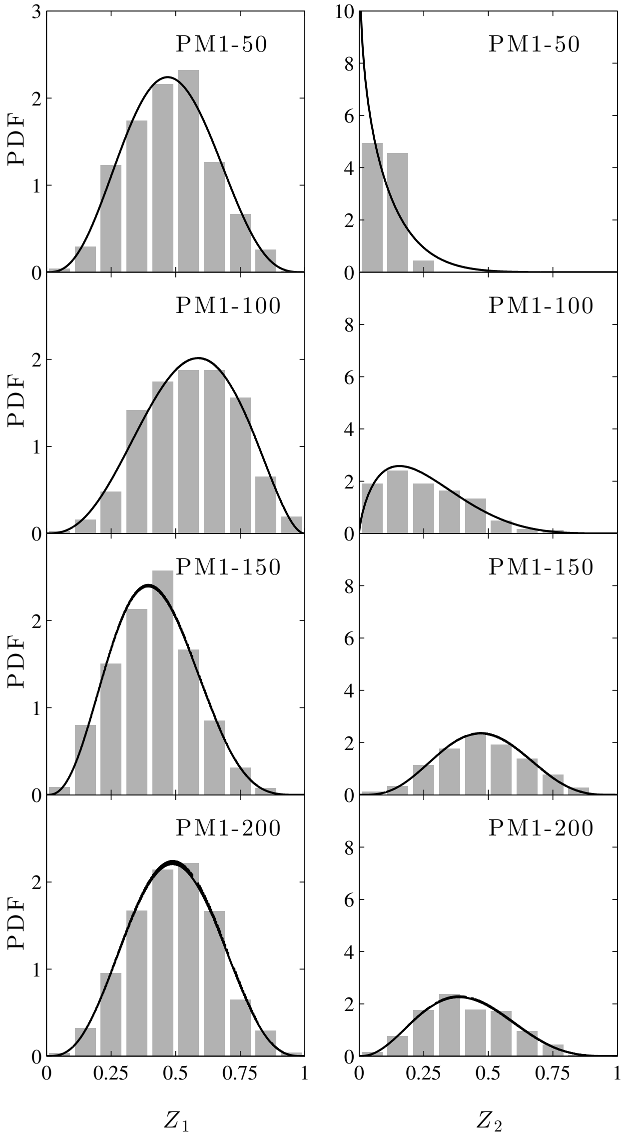

Figure 2.11: Comparison of measured and computed marginal PDFs of Z_1 and Z_2 at $x/D_{\text{ref}} = 15$ and $r/D_{\text{ref}} = 1.1$. Experimental data is represented by gray bars and results obtained from the Dirichlet-distribution as presumed PDF closure are shown by solid lines.

In summary, this prior model analysis of the presumed PDF closure shows that the Dirichlet distribution, as a multivariate generalization of the beta distribution, provides an adequate representation of the scalar mixing in this three-stream piloted burner configuration.

Following this prior model-evaluation, the three-stream FPV model is next applied to LES of the PPJB-configuration. After presenting the computational setup and

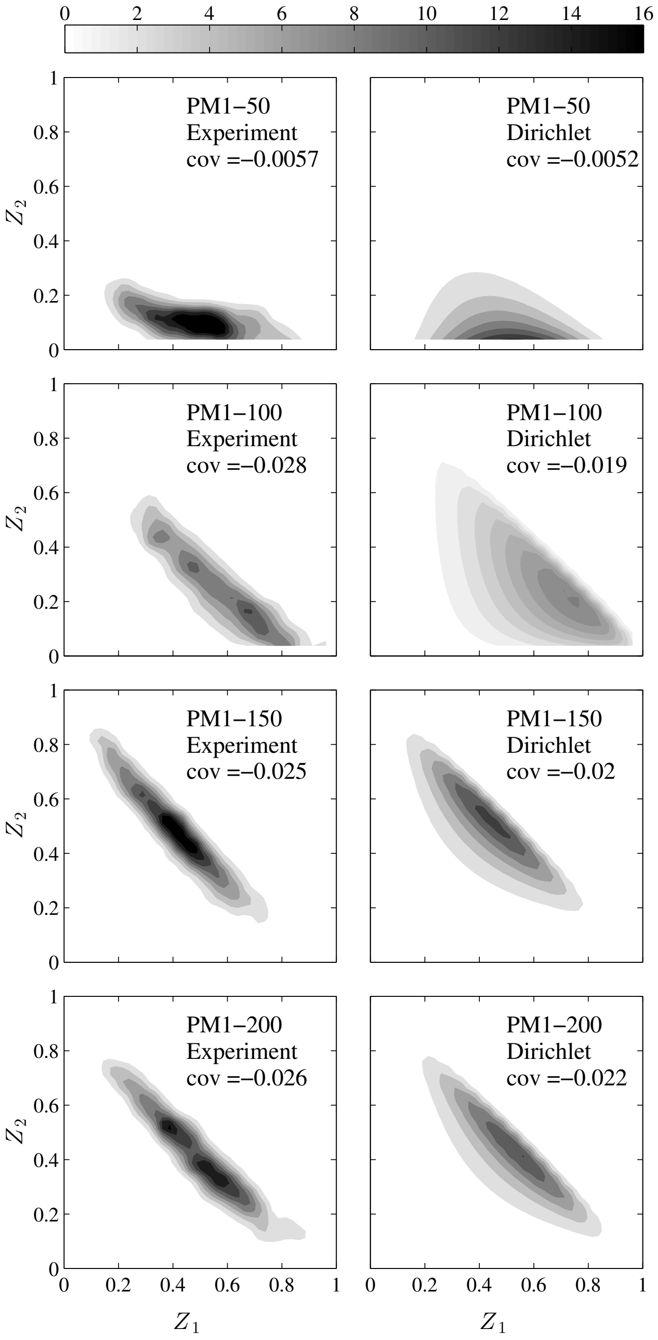

Figure 2.12: Comparison of joint PDFs of Z_1 and Z_2 at $r/D_{\text{ref}} = 1.1$ and $x/D_{\text{ref}} = 15$ for experimental data (left) and Dirichlet distribution (right).

discussing heat-loss effects in the next section, simulation results will be presented in Sec. 2.6.

2.5 Computational Setup and Boundary Conditions

2.5.1 Numerical Setup

The governing equations are solved in a cylindrical domain, having a length of 60 D_{ref} and a radius of 20 D_{ref}. The computational domain is discretized by a structured grid with 256 grid points in axial direction, 256 grid points in radial direction, and 64 grid points in azimuthal direction. The grid is stretch in axial and radial directions to resolve the shear layer and nozzle-near region. An equidistant grid is used in azimuthal direction. The grid spacing information is shown in Fig. 2.13. A grid convergence study on a shorter domain has been carried out for PM1-100 with three refinement levels, and only insignificant changes in velocity and mixture-fraction profiles were found.

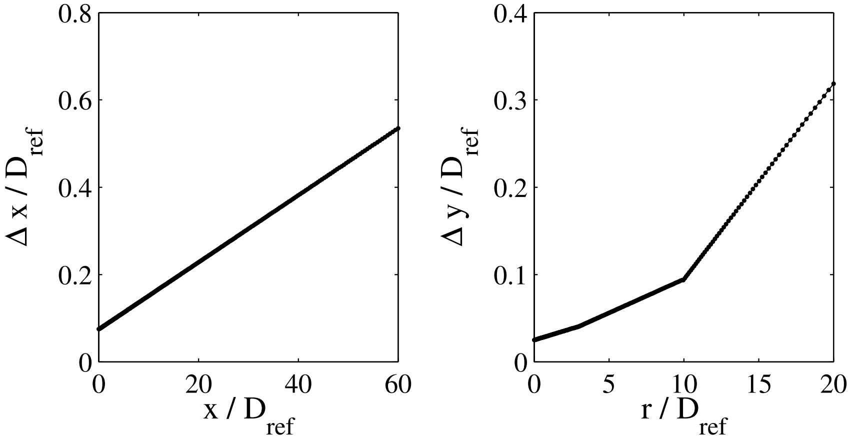

Figure 2.13: Grid spacing in axial and radial directions.

The inflow velocity profile in the fuel-stream is prescribed from the solution of a turbulent periodic pipe-flow simulation by enforcing the experimentally reported bulk-flow velocity. Inlet velocity profiles for the pilot and coflow follow a hyperbolic tangent profile with specified boundary-layer thickness of 0.05 D_{ref}. From parametric investigations, it has been determined that the boundary layer thickness has only a minimal impact on the entrainment near the nozzle exit.

The generating of the chemistry library follows a four-steps procedure: *i*) we first generate all flamelets that we parameterize in terms of Z_2; *ii*) for the given set of flamelets at a specified Z_2, we then sort all flamelets with respect to the reaction progress parameter; *iii*) the flamelet solutions are then interpolated onto a structured generalized curvilinear mesh of very fine resolution; *iv*) finally, Eq. (2.7) is evaluated by discretizing the integral using a second order accurate trapezoidal rule. The resulting four-dimensional table is then discretized using a structured mesh. The mesh is conform along the $\widetilde{Z_1}$-$\widetilde{Z_2}$ directions, equidistantly spaced along the direction of $\widetilde{C}$, and grid-stretching is employed in the $\widetilde{Z''^2_1}$-direction to increase the resolution. The chemistry library is discretized by 100 × 25 × 10 × 75 in the directions of $\widetilde{Z_1} \times \widetilde{Z''^2_1} \times \widetilde{Z_2} \times \widetilde{C}$.

2.5.2 Wall Heat Losses

Temperature measurements [35] near the burner-exit showed that the gas mixture in the pilot and coflow streams are affected by heat-losses to the wall. This was also confirmed computationally by Rowinski & Pope [28].

To investigate the effect of the temperature non-uniformity on the present simulation results, we first performed an adiabatic base-line computation of the PM1-100 case. In this simulation, we prescribed homogeneous scalar boundary conditions for $\widetilde{Z_1}$, $\widetilde{Z_2}$, and $\widetilde{C}$ at the inflow. Results from this calculation are presented in Fig. 2.14, showing that the temperature near the nozzle exit between pilot and coflow (close to $r/D_{\mathrm{ref}} = 3$) is approximately 250 K higher than the experimental data.

Measurements suggest that these heat-losses are confined to a chemically inert region near the nozzle exit. Therefore, we incorporate heat-loss effects into the model in an approximate way. To this end, the flamelet-space along the direction of Z_1 is extrapolated to $Z_1 < 0$ following the relation $dZ_1 = (\partial_{Z_1} T)^{-1} dT$, and $\partial_{Z_1} T$ is evaluated from a non-reacting flamelet. The density in this non-adiabatic region is evaluated from the temperature profile and the mixture is identical to that of the reactant composition at $Z_1 = 0$. In this way, the effect of changing inlet temperature profiles can be represented in terms of the mixture-fraction profiles at the inlet without altering the species composition. Boundary conditions for the mixture fraction Z_1 are then obtained by extrapolating the measured temperature profiles at $x/D_{\mathrm{ref}} = 2.5$ upstream of the nozzle-inlet plane. The so evaluated inlet boundary conditions for $\widetilde{Z_1}$, $\widetilde{Z_2}$, and $\widetilde{C}$ are shown in Fig. 2.15 along with the corresponding temperature profile. The mixture fraction variance $\widetilde{Z''^2_1}$ is set to zero in the inlet.

Using this model-extension, an additional simulation for the case PM1-100 is performed and the results are compared to the adiabatic formulation in Fig. 2.14. Comparing the temperature profiles at the first two measurement locations, it can be seen that the inclusion of wall-heat losses in this approximated way results in significant improvements of the temperature profiles without affecting the species composition, thereby retaining model consistency.

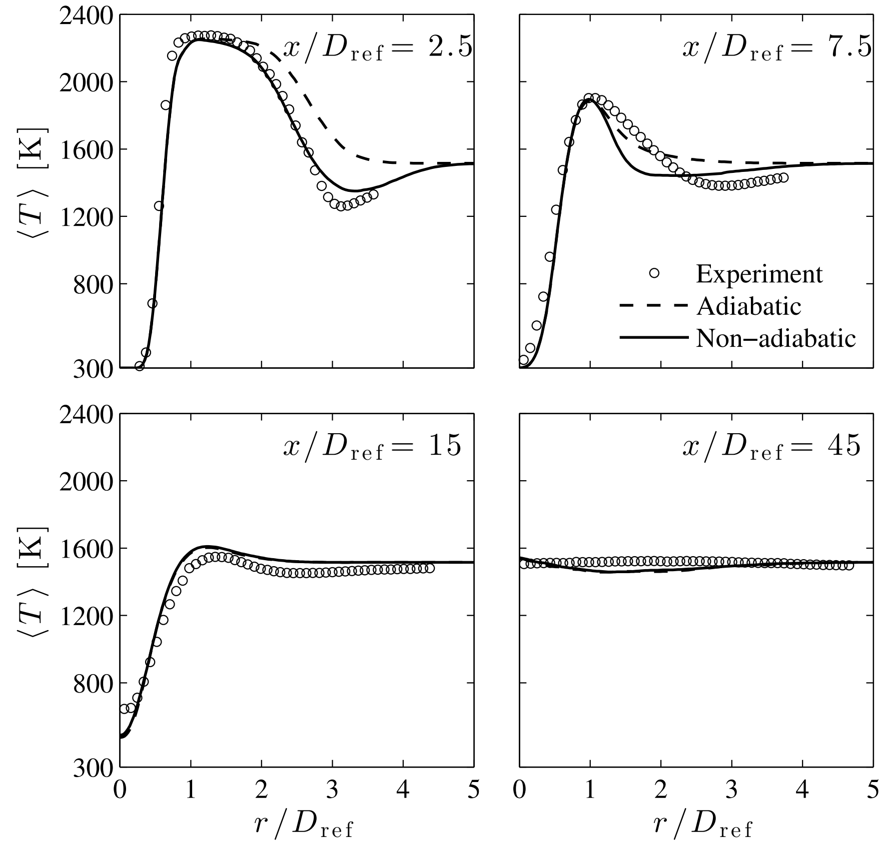

Figure 2.14: Effect of wall-heat losses on the temperature field for the case PM1-100.

Since the impact of wall-heat losses is limited to the temperature field in close proximity to the nozzle-near region, the following analysis will focus on the results obtained from the adiabatic three-stream FPV formulation, recognizing that this model can be extended to incorporate heat-loss effects [48].

2.6 Results

In the following sections simulation results for all four operating conditions are compared with experimental data. All simulations are conducted using the same computational mesh, chemistry library, closure models, and boundary conditions in the coflow and pilot streams. Specific to each case, velocity inlet conditions are prescribed from separate turbulent pipe-flow simulations. Statistical results are obtained by averaging over azimuthal direction and in time. All simulations were conducted over ten flow-through times to obtain statistically converged results. Mean quantities are denoted by angular brackets and RMS-quantities are denoted by a dash.

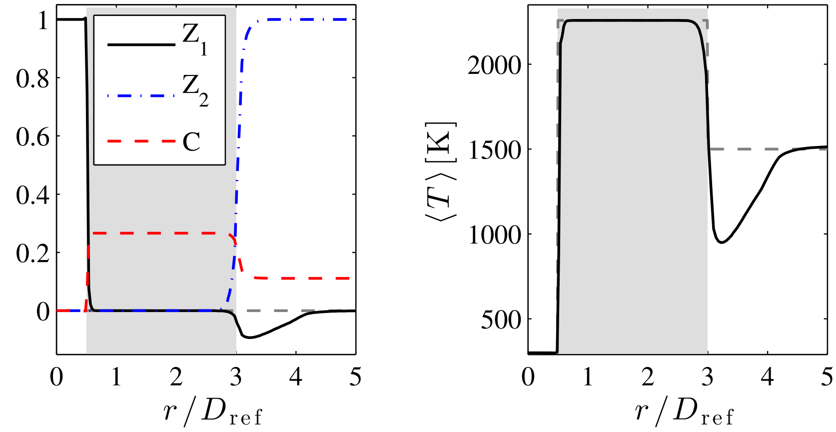

Figure 2.15: Inlet profiles of $\widetilde{Z_1}$, $\widetilde{Z_2}$, and $\widetilde{C}$ (left) and temperature (right) for PM1-100; the gray dashed line indicates the boundary condition of $\widetilde{Z_1}$ for the homogeneous case and its corresponding temperature profile is shown on the right. The shaded region indicates the pilot stream.

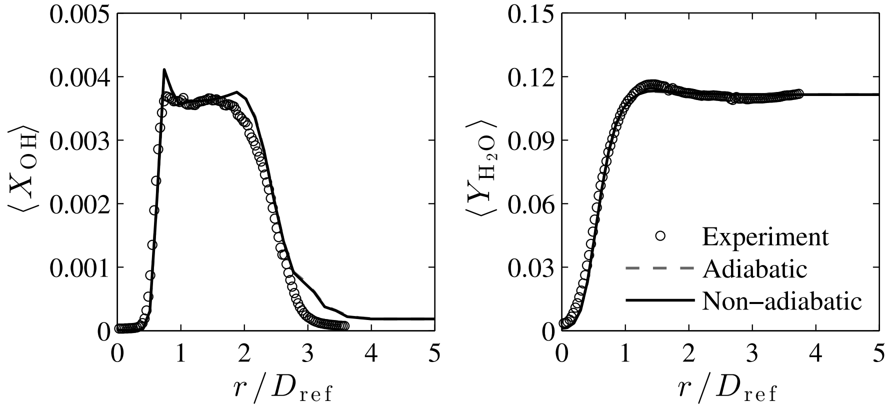

Figure 2.16: Radial profiles of mean mole fraction of OH (left) and water mass fraction (right) for PM1-100 at $x/D_{\mathrm{ref}} = 2.5$.

2.6.1 Mixture Fraction Results

An important set of flow-field quantities for model comparisons are the two mixture fractions Z_1 and Z_2. Comparisons of radial profiles for the mean and RMS of these quantities are presented in Figs. 2.17 and 2.18.

It is noted that measurements for PM1-50 were not reported at $x/D_{\mathrm{ref}} = 45$, so that only comparisons for PM1-{100,150,200} are shown at the last measurement station. Good agreement between measurements and simulations is obtained at the first measurement location for all four cases. However, differences become appar-

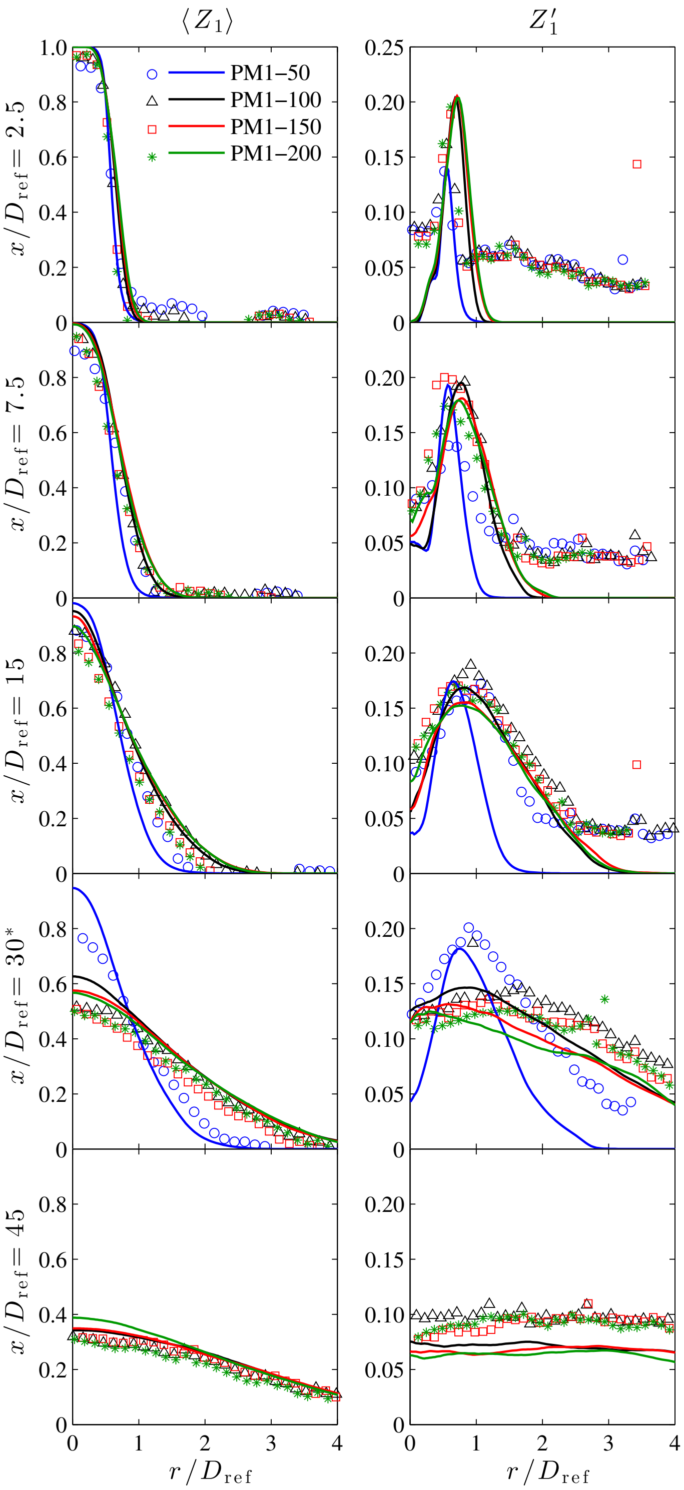

Figure 2.17: Comparisons of measured (symbols) and computed (lines) radial mixture fraction profiles for Z_1; (*) data is measured at $x/D_{\text{ref}} = 25$ for PM1-50.

ent with increasing downstream direction. While discrepancies for the cases PM1-{100,150,200} are mostly confined to the centerline, differences in radial decay are apparent for the low-speed case PM1-50. Shown on the right of Fig. 2.17 are the RMS-quantities, and it can be seen that the location and peak value are adequately predicted by the simulations. In the present simulation, the chemical composition in the coflow is assumed to be uniform in each stream. The experimentally reported fluctuations do not exceed five percent, and these perturbations could be attributed to a variability in the pilot-burner, which was also discussed in Sec. 2.4.1.

Comparisons of radial profiles for the first two moments of Z_2 are presented in Fig. 2.18, and the agreement between experiments and simulations is comparable to the results that were obtained for the primary mixture fraction. The only major difference between experiments and predictions is observed at $x/D_{\text{ref}} = 2.5$ for the case PM1-50. With increasing downstream distance the agreement improves. At the last measurement station, the mixture fraction profiles for the cases PM1-{100,150,200} converge and no significant differences are apparent.

2.6.2 Velocity Profiles

Comparisons of mean and RMS profiles for the axial velocity component are shown in Fig. 2.19. The measurements show qualitatively and quantitatively different results between PM1-50 and the other three cases. In particular, the mean-velocity profile for PM1-50 plateaus and stays fairly constant until $x/D_{\text{ref}} = 30$, after which the velocity rapidly decays. In contrast, the mean-velocity profiles continuously decay for the other cases. Apparent from the measurements for PM1-150 and PM1-200 are two clearly distinct regions with different velocity decay rates. This can be attributed to the depletion of the pilot and subsequent replacement of fluid from the outer coflow.

The simulations capture the trend of the mean and RMS velocity profiles. Although inflow-conditions from a turbulent pipe-flow simulation with specified bulk-flow were used, some differences between simulations and measurements can be observed.

2.6.3 Temperature Results

Comparisons of the temperature fields for all four configurations are presented in Fig. 2.20. In these figures the instantaneous temperature fields are shown on the left and mean temperature results are presented in the panels on the right.

This direct comparison emphasizes the effect of the increasing jet-exit velocity on

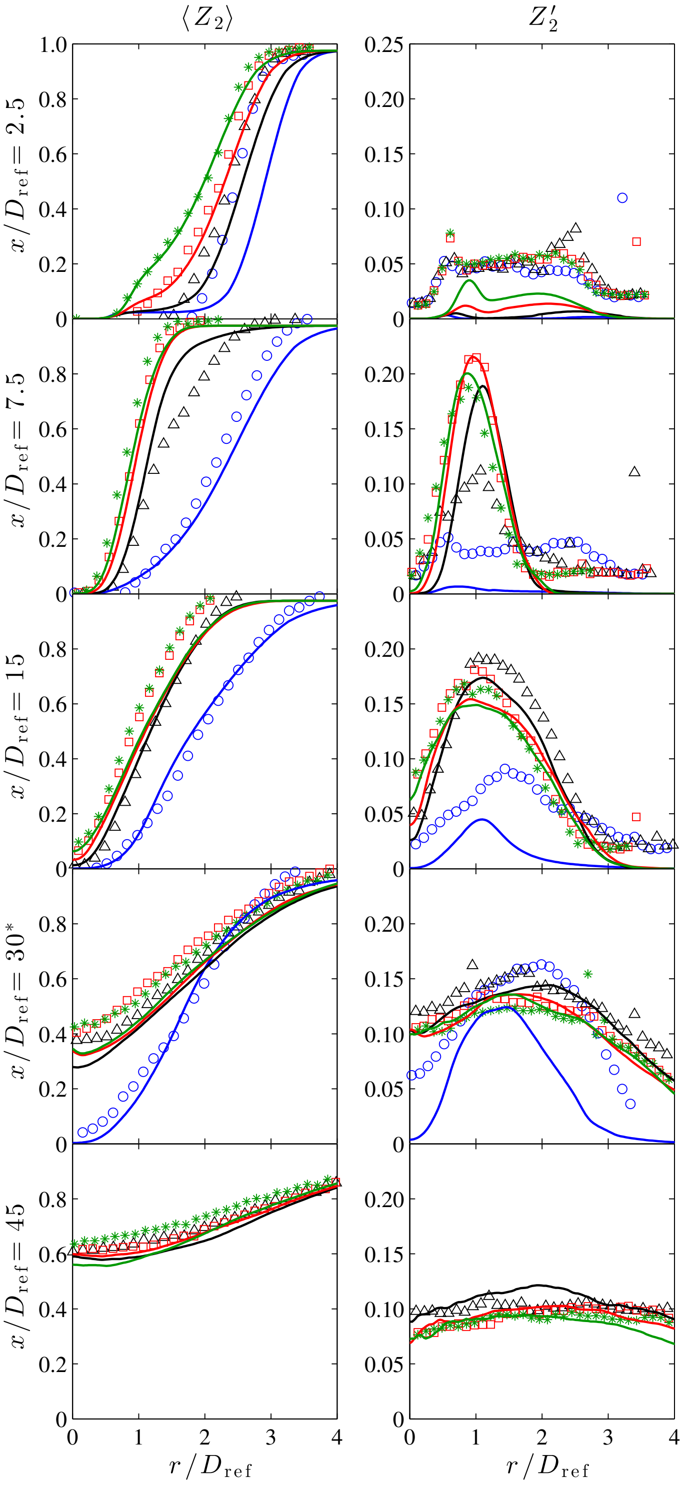

Figure 2.18: Comparisons of measured (symbols) and computed (lines) radial mixture fraction profiles for Z_2; (*) data is measured at $x/D_{\text{ref}} = 25$ for PM1-50. Refer to Fig. 2.17 for legend.

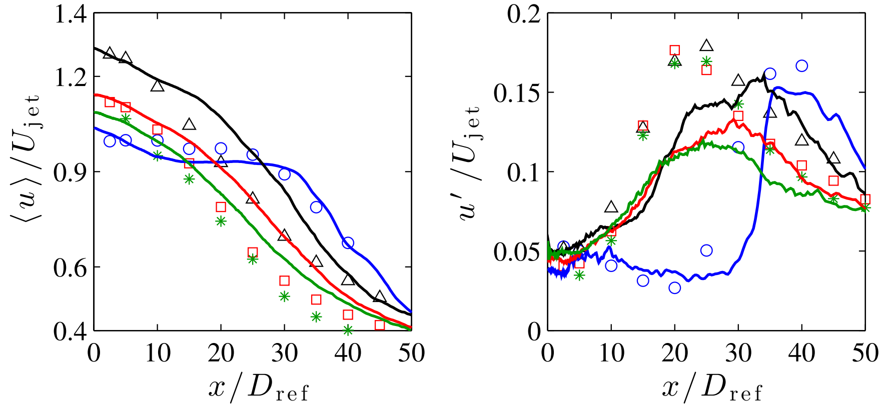

Figure 2.19: Comparison of mean and RMS axial velocity profiles along jet centerline. Refer to Fig. 2.17 for legend.

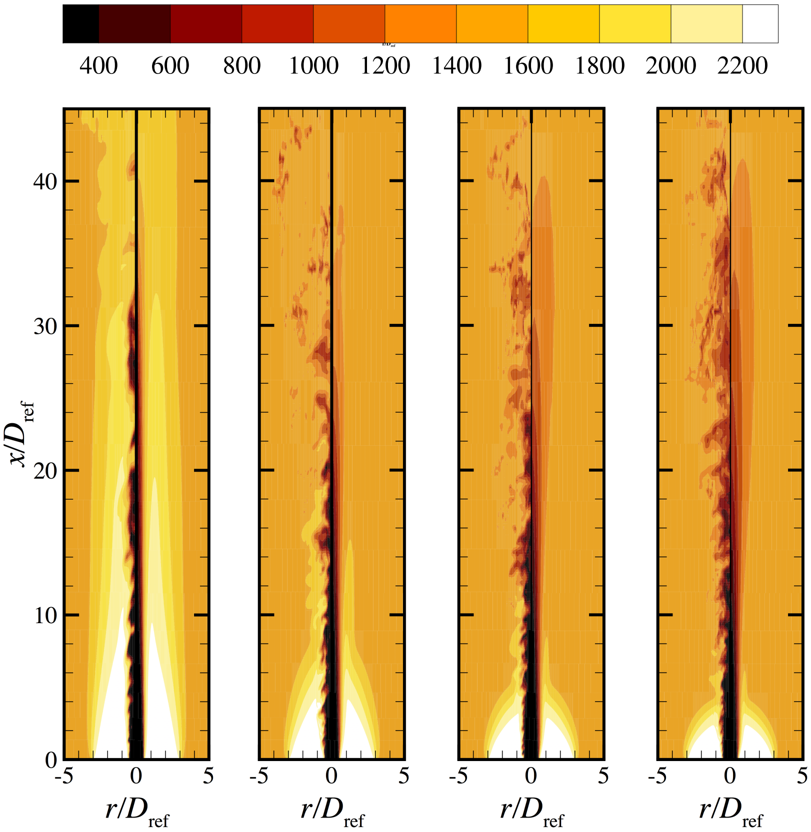

(a) (b) (c) (d)

Figure 2.20: Comparison of the instantaneous (left) and mean (right) temperature field (in units of Kelvin) for (a) PM1-50, (b) PM1-100, (c) PM1-150, and (d) PM1-200.

the temperature field, resulting in enhanced entrainment of the outer streams into the jet core region. Specifically, the temperature field for the case PM1-50 (Fig. 2.20a) exhibits a fairly continuous region of high temperature gases that extends continuously from the pilot to the downstream region beyond $x/D_{\text{ref}} = 30$. However, from PM1-100 and onward, the formation of a "neck-region" is clearly evident at which the pilot stream is fully depleted and replaced by the outer coflow. This neck-region moves closer to the nozzle exit with increasing jet exit velocity. To complement this qualitative analysis, comparisons of statistical temperature profiles are presented in Fig. 2.21. Note that for the case PM1-50 the temperature was measured at $x/D_{\text{ref}} = 25$ instead of 30, and measurements at $x/D_{\text{ref}} = 45$ were not reported.

Good agreement for mean and RMS temperature results is obtained for all three cases. Differences on the outer side of the pilot-stream at $x/D_{\text{ref}} = 2.5$ are attributed to heat-losses, which has been discussed in Sec. 2.5.2. Apart from this discrepancy, simulation results for PM1-50 and PM1-100 are in good agreement with experiments, and the peak temperature location and flame-length are well predicted. With increasing jet-exit velocity the model overpredicts the heat release. A potential reason for this discrepancy can be attributed to the subgrid-closure to capture local extinction and reignition. Such effects can be incorporated into this model formulation by utilizing an unsteady flamelet-formulation, which was discussed for the modeling of autoignition and vitiated combustion [44].

2.6.4 Species Results

Comparisons of radial profiles for species mass fractions of methane, water, and carbon dioxide, as well as hydroxyl mole fraction are presented in Figs. 2.22 and 2.23. Good agreement with experiments is obtained for Y_{CH_4} and $Y_{\text{H}_2\text{O}}$ at the first two measurement locations, and only marginal differences among the different cases are apparent. Predictions for the water mass fraction are in close agreement with the measurements throughout the flame. However, evident from the methane-profiles is an overprediction of the fuel consumption beyond $x/D_{\text{ref}} = 15$. This trend correlates with higher flame-temperature and heat-release which was discussed in the context of Fig. 2.21.

Modeling results for the CO_2 mass fraction are presented in the first column of Fig. 2.23. Apart from a slight shift in the region corresponding to the outer shear-layer for PM1-50, the modeling results are in good agreement with experiments. Due to the higher reaction progress, Y_{CO_2} is overpredicted at the last two measurement locations for PM1-150 and PM1-200, and similar results have been reported by Rowinski &

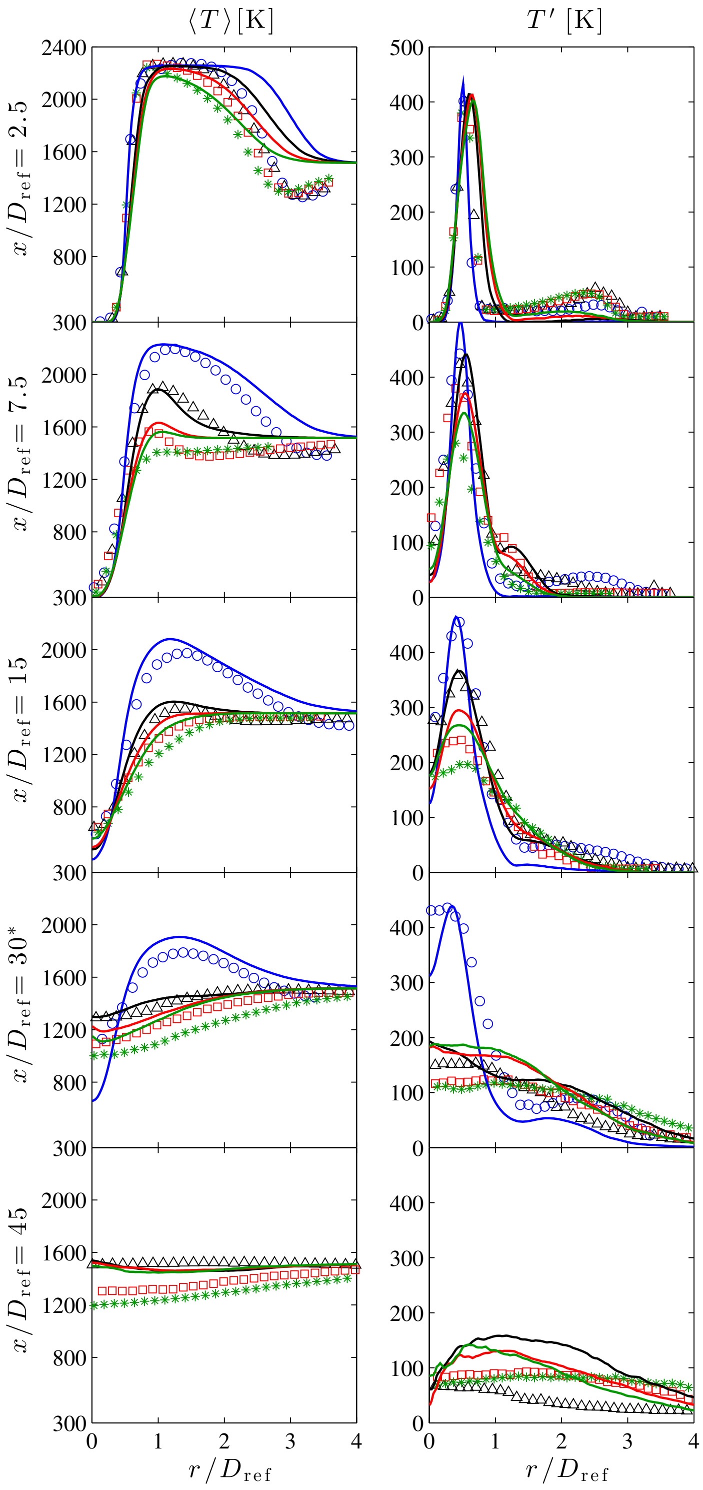

Figure 2.21: Comparisons of radial temperature profiles. Refer to Fig. 2.17 for legend.

Pope [28].

Comparisons for the mean OH-mole fraction are presented in the right column of

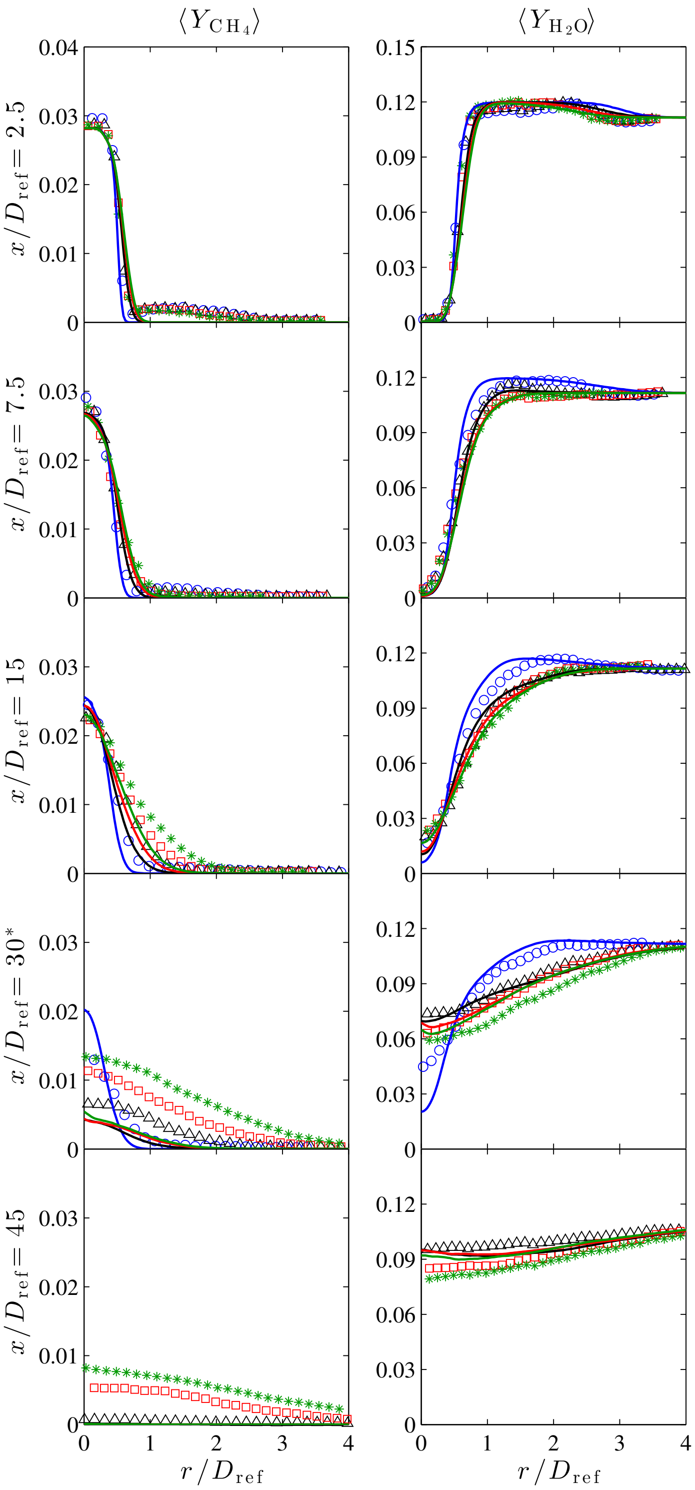

Figure 2.22: Comparisons of radial profiles for mass fractions of methane (left) and water (right). Refer to Fig. 2.17 for legend.

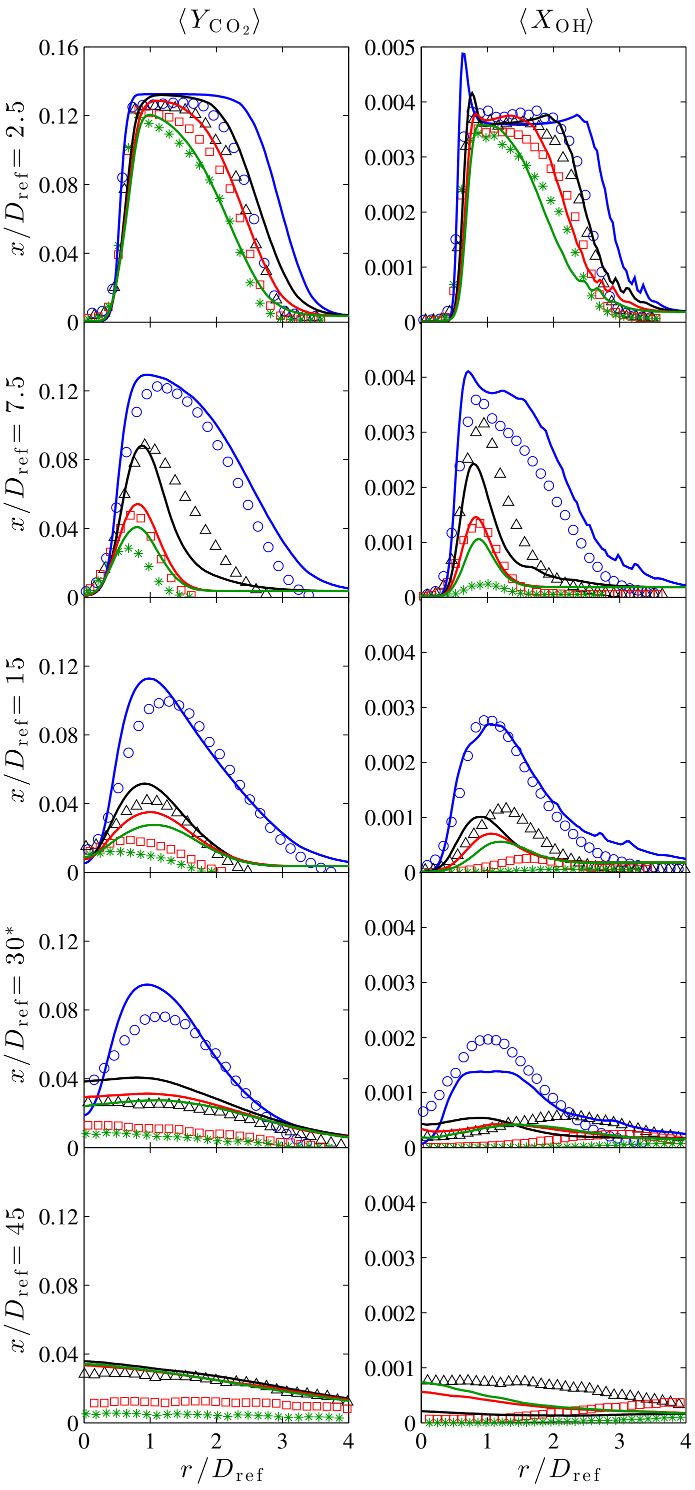

Figure 2.23: Comparisons of radial profiles for carbon dioxide mass fraction (left) and mole fraction of OH (right). Refer to Fig. 2.17 for legend.

Fig. 2.23. The satisfactory agreement at the first measurement location can be attributed to the adjustment of the boundary conditions, and was discussed in Sec. 2.4.1. While the model underpredicts X_{OH} for PM1-100, a consistent overprediction for the cases PM1-150 and PM1-200 is observed. However, given the assumption of homogeneous scalar inflow compositions in the pilot and coflow streams the agreement is acceptable and further improvements can be expected by accommodating variable (and time-dependent) species profiles.

2.6.5 Scatter Data

An analysis of the thermochemical state-space representation of the combustion model is performed by comparing correlations between $Y_{\mathrm{CO}}, X_{\mathrm{OH}}$ and temperature. Comparisons between simulations and experiments for all four cases and different axial flame locations are presented in Figs. 2.24 and 2.25. The scatter data are extracted along the radial direction until 4 D_{ref} away from the centerline. From Fig. 2.24 it can be seen that the experimental data exhibit a weak dependence on operating conditions: Specifically, while the peak CO mass-fraction increases with increasing jet exit condition at the first measurement location, the opposite trend can be observed for further downstream locations. Although this weak sensitivity is not fully captured by the simulations, the quantitative agreement with measurements improves with increasing downstream distance and increasing jet-exit velocities. Reasons for the apparent differences near the nozzle have been discussed previously and were partially attributed to inhomogeneities in the burner exit conditions, as shown by the excess fuel in the pilot stream.

Results for X_{OH}-T correlations are shown in Fig. 2.25. Overall, the simulation results are in good agreement with experiments, and discrepancies are confined to the nozzle-near region. Compared to the CO-profiles, it can be seen that OH exhibits a more pronounced sensitivity to the jet-exit velocity. While the peak OH concentration decreases continuously for the cases PM1-50 and PM1-100, a dramatic drop in the peak X_{OH}-value is apparent at the second measurement location for the other two cases, suggesting the presence of flame-quenching. The slight increase in the OH mole fraction (evident from the measurements) with increasing downstream distance suggests the occurrence of reignition events.

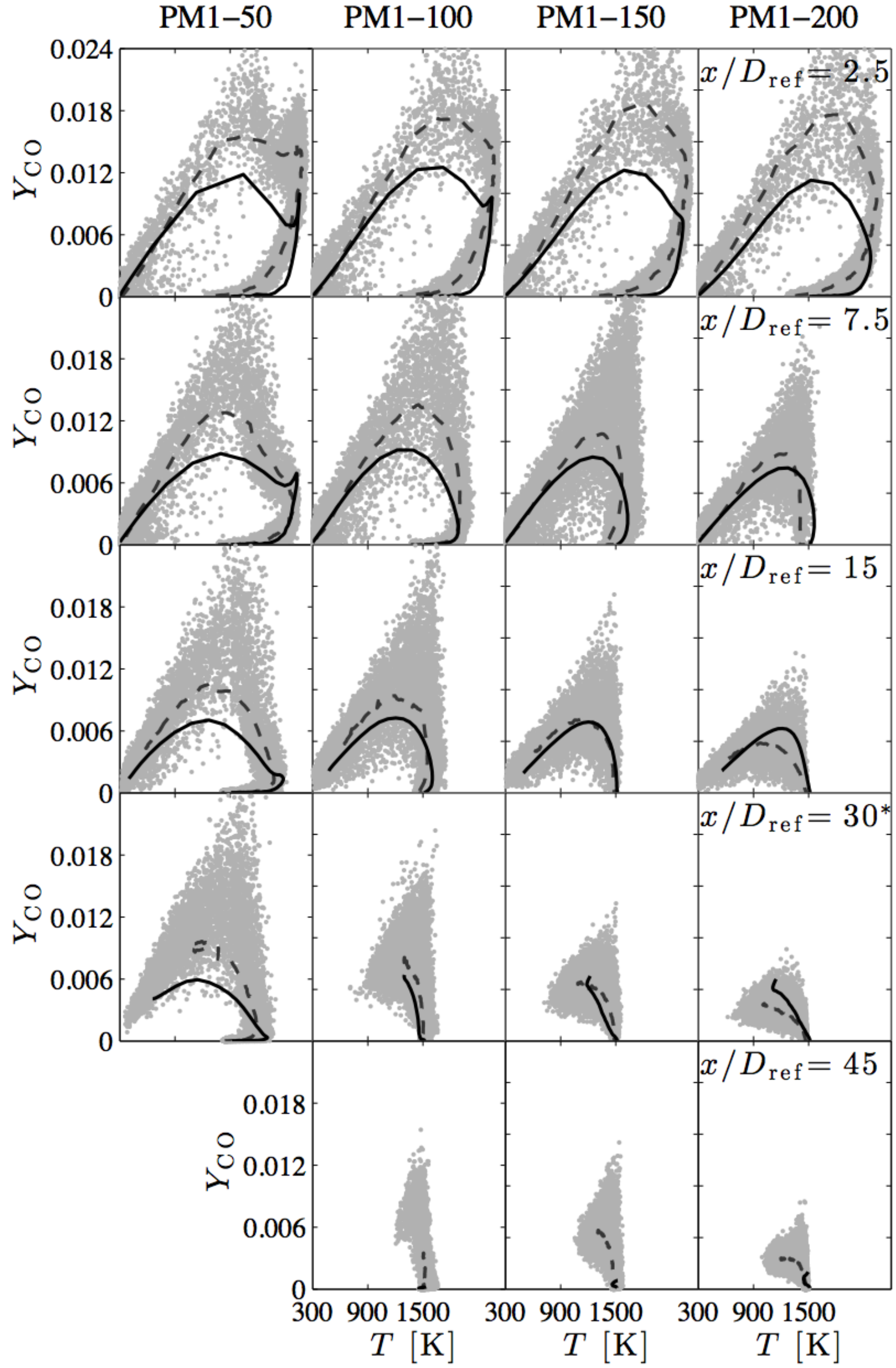

Figure 2.24: Comparison of Y_{CO}-T correlation data at different axial locations; gray symbols are experimental scatter data; dashed lines are experimental mean profiles, and solid lines correspond to simulation results; (*) data is measured at $x/D_{\mathrm{ref}} = 25$ for PM1-50.

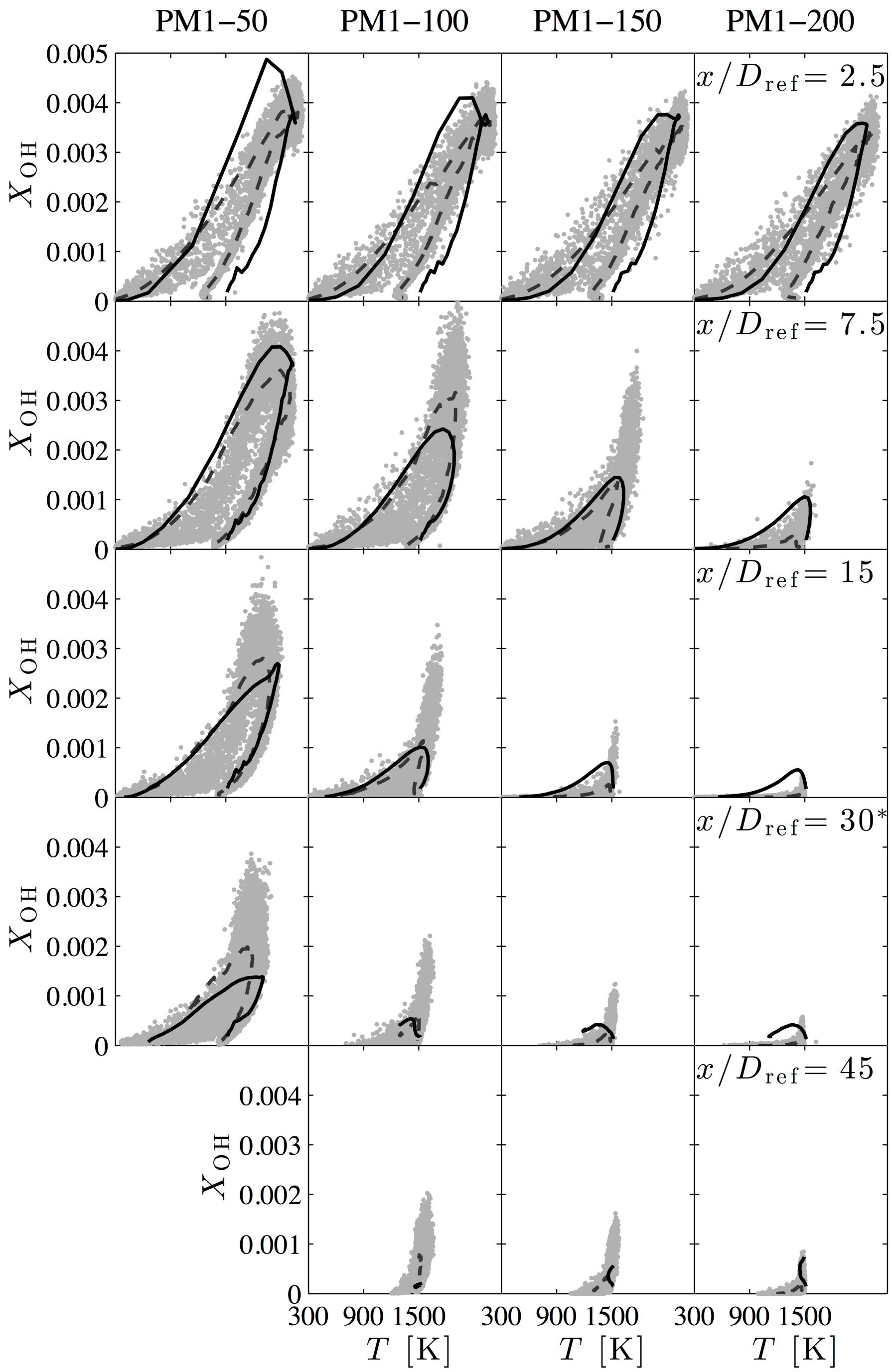

Figure 2.25: Comparison of X_{OH}-T correlation data at different axial locations; gray symbols are experimental data; dashed lines are experimental mean profiles, and solid lines correspond to simulation results; (*) data is measured at $x/D_{\mathrm{ref}} = 25$ for PM1-50.

2.7 Summary and Conclusions

A three-stream Flamelet/Progress Variable (FPV) model was applied to the Piloted Premixed Jet Burner (PPJB), which was experimentally investigated by Dunn et al. [3]. Simulations of all four operating conditions, designated as PM1-50, PM1-100, PM1-150, and PM1-200, were performed, and a prior model evaluation was conducted to assess the validity of critical modeling assumptions regarding the applicability of this formulation to partially premixed combustion, the statistical representation of the scalar mixing, and the joint PDF-closure. In this investigation:

- A Dirichlet distribution was introduced as presumed PDF closure for the two mixture fractions. This distribution is described by three parameters, and reduces to the marginal beta-PDF in the limit of two-stream mixing. Comparisons with experimental results showed that this presumed PDF-closure accurately represents the PDF-shape and covariance of the measurements.

- The representation of the flame thermochemistry using the three-stream flamelet formulation was assessed through direct comparisons with experimental scatter data. For the limiting cases PM1-50 and PM1-200 it could be confirmed that temperature, major species, and OH are well represented by the chemistry library, and only the carbon monoxide mass fraction deviates from the flamelet manifold near the nozzle.

- An analysis of the measured scalar inflow composition and comparisons with equilibrium computations showed the presence of excess fuel and species inhomogeneities in the pilot stream. By recognizing that the flame is sensitive to the scalar inflow-composition, the radial distribution of the scalar inflow profiles requires consideration in the simulation, adding only insignificant overhead to the computations.

- Comparisons with experimental results showed that the three-stream combustion model can predict the temperature and major species in the region that is controlled by the interaction between the pilot and the fuel streams with adequate accuracy (within ±5% in most cases). However, with increasing downstream distance, the model overpredicts the reactivity, which can be attributed to extinction and reignition processes (as shown in figure 2.23 for OH concentrations). These effects can be incorporated in this three-stream flamelet model by utilizing an unsteady flamelet formulation [44].

- A comparison of correlation data for Y_{CO}-T showed that the model underpredicts the peak CO location, but accurately captures the sensitivity of OH formation with respect to the operating conditions.

- Compared to previous studies, the extended FPV model is found to be more robust, and can provide predictions of temperature and species distributions that are closer to the experimental data. This is partly due to the proposed joint PDF better captures the scalar mixing process in this burner.

In the meantime, if we look at the general applicability of high-fidelity combustion models on partially premixed combustion regime, we can see that on one hand, these models could provide a comprehensive data set of temperature, velocity, and species with very high spacial resolutions simultaneously. Despite the best effort of experimentalists, this level of detail can yet be achieved by any experimental setup. Also, as the complexity of the configuration grows, the setup of numerical investigations are often cheaper and faster than an equivalent experimental effort. Those are the undeniable advantages of computations.

On the other hand, we noticed some discrepancies between simulation results and experimental data in some minor specie concentrations. The causes of these discrepancies can be a combination of experimental uncertainties, model assumption limitations, and the accuracy of boundary conditions. The PPJB is geometrically fairly simple and in our study it burns a chemically simple fuel. If complex flames like those encountered in real world engine environments require modeling, the challenges that we faced in this study will be more prominent. In that case, in addition to determining the sources of uncertainties, we also need to tackle the issues of generating complex mesh and accurately representing the chemical interactions with limited computational resources. Those are the aspects that we need to consider before applying these high-fidelity models.

CHAPTER III

Reduced-order Modeling of Combustion Instability – the Modular Reduced-order Model Framework (MRMF)

3.1 Introduction

Combustion instability is a challenging issue in the combustion sciences community. On one hand, it is a complicated process, being the result of the interactions between turbulence, combustion, and acoustics. As introduced in chapter I, we still do not have a closed form formulation of turbulent combustion, let alone adding acoustic fluctuations. On the other hand, combustion instability is a very important process that we have to understand. As we move from non-premixed combustion to partially premixed combustion, we can get dangerously close to the envelope where combustion instability may occur. The consequence of experiencing combustion instability in real life may be the loss of many lives and millions of dollars.

Hence we have no choice but to push ourselves to understand, and eventually to be able to predict and mitigate combustion instability. In section 1.3 we learnt that combustion instability is a result of heat release and pressure oscillation where they are in phase. Both of them may be quite geometry-dependent. As a result, if we want to study the instability process that we encounter in real world, we need a platform that contains the essential features of practical combustors. In the meantime, this platform has to be simple in structure that it is both reasonable in cost to operate in a academic institution and easy to apply diagnostics tools on.

Several such burners have been developed in many institutions, such as Cambridge University [49], DLR [7], and CNRS [50]. They provide very good access to diagnostic tools, hence it is advantageous to conduct experimental studies on these burners. However, in order to preserve the resemblance to their real world counterparts, these burners need to retain a minimal amount of geometrical complexity, such as swirl veins and nozzle injectors.

From our previous study in the Piloted Premixed Jet Burner (PPJB) in chapter II we learnt that accurately simulating burners that are geometrically and physically complicated with high fidelity models can be very challenging. See and Ihme [51] demonstrated that satisfactory simulation results could be achieved for certain operating conditions of a Gas Turbine Model Combustor (GTMC) designed by DLR in Stuttgart. However, the acoustically unstable cases have yet to be tackled. As well, these high-fidelity simulations require extensive mesh-generation expertise and a large amount of computational resources. It is hence attractive to develop a reduced order model that can capture the main physical processes in the combustor without too many computational complications.

Such approaches have been taken by several research groups on various experimental geometries. Notably, Hathout et al. [4] studied the case where a combustion chamber with an inlet and an outlet acts as a Helmholtz resonator. Heat release rate of the combustion chamber was related to flame surface area, which was determined by local flame speed and inlet velocity, with the latter being the deciding factor. Pressure and velocity were correlated in the inlet pipe through conservation of momentum. In this way a second-order ordinary differential equation was then derived for the pressure fluctuations. Through stability analysis of the equation, the stable operating envelop was determined.

Researchers from Laboratoire EM2C at École Centrale Paris studied another set of setups [52, 53]. Specifically, Schuller et al. [5] studied the acoustic coupling effects of a plenum-injector-combustor system using a reduced order model through matrix eigenvalue analysis. Palies et al. [6] studied the same setup with fluctuating heat release rate, using the Flame Describing Function (FDF) framework. Furthermore, this analysis was compared to a Helmholtz solver by Silva et al. [54], with good agreements.

In this chapter we will first review some of the available reduced order model in literature in section 3.2, we will then analyze their advantages and disadvantages. In section 3.3 we will discuss a newly proposed reduced order model for combustion instability, called the Modular Reduced-order Model Framework (MRMF) or the "Michigan model". After setting up the groundwork of this model framework, we will discuss the major parts of the model in the following sections: pressure modeling in section 3.4, heat release modeling in section 3.5, and velocity coupling modeling in section 3.6. In section 3.7, we will integrate the various parts of the framework for application in the DLR GTMC.

3.2 Review of Previous Models

3.2.1 The MIT Model

The first model that we will review is proposed by Hathout et al. [4]. Here we name it "the MIT model" because of the authors' affiliation. It was developed to model turbulent premixed flames. It assumes that at high Damköhler numbers and weak to moderate turbulence intensity, turbulent premixed flames can be modeled by wrinkled laminar flames. To derive this model, the following assumptions are made:

- The flame is very thin and insensitive to pressure fluctuations,
- The model can be applied in situations where Damköhler number is high and turbulence intensity is weak to moderate,
- The flame is weakly convoluted.

This model is composed of several modules, each of them describes a particular part of physics in the process. They are laid out in the following paragraphs.

3.2.1.1 Flame dynamics

The flame dynamics module of this model is derived in the setup of a conical flame anchored over a ring. Let the instantaneous radial location of flame to be $\xi(r,t)$, then it follows that:

$$\frac{\partial \xi}{\partial t} = u - v\frac{\partial \xi}{\partial r} - S_{\mathrm{u}}(\phi)\sqrt{\left(\frac{\partial \xi}{\partial r}\right)^2 + 1}. \tag{3.1}$$

The effects of fluctuations of velocity and equivalence ratio on the instantaneous flame surface location would be:

$$\frac{\partial \xi'}{\partial t} = u' + \overline{S}_{\mathrm{u}}\frac{\partial \xi'}{\partial r} + \frac{\partial \overline{\xi}}{\partial r}\left.\frac{dS_{\mathrm{u}}}{d\phi}\right|_{\overline{\phi}}\phi'. \tag{3.2}$$

The instantaneous flame location is related to the total heat release (Q) by:

$$Q = \kappa(\phi)\int_0^R \left[\sqrt{1 + \left(\frac{\partial \xi}{\partial r}\right)^2}\right] dr, \tag{3.3}$$

here $\kappa(\phi)$ is a function of density, laminar flame speed, and heat of reaction. So the fluctuation of ξ caused by u' and ϕ' will also result in the fluctuation of heat release rate (Q'):

$$Q'(t) = \overline{\kappa} \int_0^R \xi'(r,t)dr + d_\phi \phi'. \tag{3.4}$$

If we take the time derivative of Eq.(3.4), we will eventually arrive at the equation for heat release rate fluctuation $\dot{Q}'$ in terms the fluctuations of velocity and equivalence ratio:

$$\dot{Q}' = d_0 u' + d_1 \left[u'_{\tau_f}(t)\right] + d_2 \left[\phi'_{\tau_f}(t)\right] + d_3 \phi' + d_\phi \dot{\phi}', \tag{3.5}$$

where d_* are coefficients that depend on κ, mean values of laminar flame speed and equivalence ratio.

3.2.1.2 Pressure dynamics

The pressure dynamics of the model is analyzed in the context of a Helmholtz-type combustor with two openings. A schematic of this geometry is shown in figure 3.1.

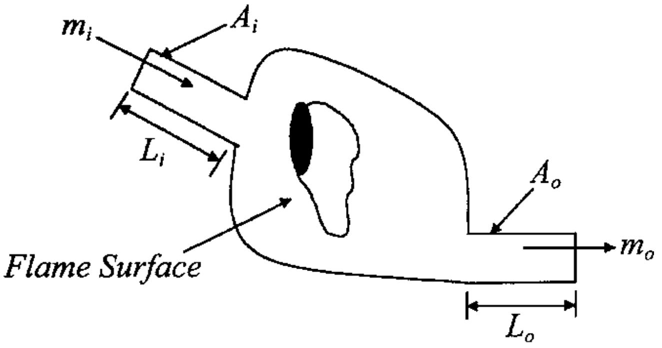

Figure 3.1: Schematics of combustor chamber in Hathout's model [4]

After a series of simplifications, the pressure equations can be shown to take the form:

$$\frac{d^2P'}{dt^2} + 2\zeta\omega\frac{dP'}{dt} + \omega^2 P' = \frac{\gamma-1}{V}\dot{Q}', \tag{3.6}$$

if the dominant mode of instability is Helmholtz mode, where P is the combustion chamber pressure and ω is the instability frequency. If the dominant mode is a standing wave, then the pressure equation would take the following form:

$$\frac{d^2P'}{dt^2} - \overline{c}^2\frac{d^2P'}{dx^2} = (\gamma-1)\dot{q}'(x,t). \tag{3.7}$$

where q is the heat release per unit volume. If the combustion chamber pressure exhibits a mix of multiple modes, the pressure fluctuations can be expanded by a base function η and its corresponding coefficient ψ as:

$$P'(x,t) = \overline{P} \sum_{i=0}^{n} \psi_i(x)\eta_i(t). \tag{3.8}$$

Then the pressure governing equations of Eq.(3.6) and Eq.(3.7) can be combined through differentiation into:

$$\ddot{\eta}_i + 2\zeta\omega_i\dot{\eta}_i + \omega_i^2\eta_i = \sum_{i=0}^{n} \overline{b}_i\dot{Q}'. \tag{3.9}$$

3.2.1.3 Heat release - Pressure Coupling

In the sections above we have described the flame dynamics and pressure dynamics in MIT model. In the flame dynamics module, Eq. (3.5) stated the resultant heat-release rate fluctuation due to equivalence ratio and velocity fluctuations. In the pressure dynamics module, Eq. (3.9) stated the effect of heat-release fluctuation on pressure oscillations. We know that combustion instabilities are governed by the interactions between pressure and heat-release oscillations, so the only missing link to connect Eqs. (3.5) and (3.9) would be the one that states the effect of pressure fluctuation on velocity and equivalence ratio fluctuations. This missing link is constructed by the following equations:

$$\phi_s = \overline{\phi}/(1+u_s'/\overline{u}), \qquad \phi' = -(\overline{\phi}/\overline{u})u', \qquad \phi' = \phi_s'(t-\tau_\mathrm{c}), \tag{3.10}$$

$$\frac{\partial u_i'}{\partial t} + \frac{1}{\rho_i}\frac{\partial P_i}{\partial x} = 0. \tag{3.11}$$

Equation (3.10) relates equivalence ratio fluctuation to that of inlet velocity with a convection time delay (τ_c). Equation (3.11) relates this velocity fluctuation with that of the combustion chamber pressure. By combining Eqs. (3.5), (3.9), (3.10), and (3.11), mathematical closure is achieved.

Lastly, if we substitute the aforementioned equations into Eq. (3.9), then we would obtain the pressure governing equation of combustion instability in the form:

$$\ddot{\eta} + 2\zeta_0\omega\dot{\eta} + (\omega^2 - k_1)\eta + k_2\eta(t-\tau) = 0. \tag{3.12}$$

The coefficients of Eq. (3.12) depends on the cause of instability and the mode of pressure oscillation. The section above only briefly introduced this model, for details

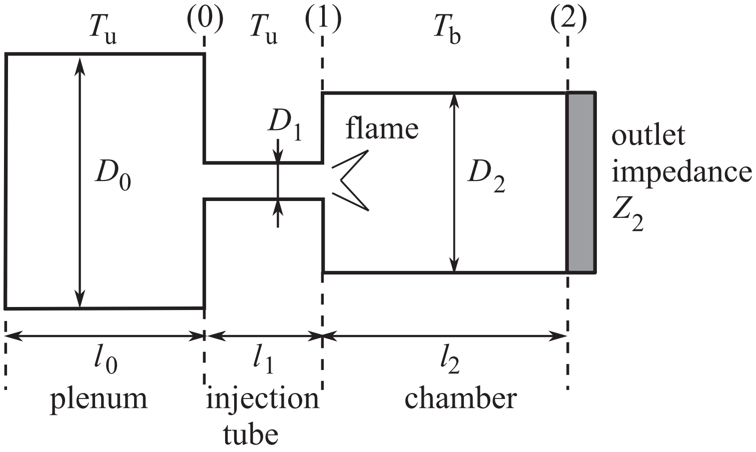

Figure 3.2: Schematic of reduced order model by Schuller et al.[5]

of the definitions of all parameters and mathematical derivations reader is referred to the original paper by Hathout et al. [4].

3.2.2 The EM2C Model

The second model that we survey is proposed by a group of researchers from Laboratoire EM2C at École Centrale Paris. The details of this model can be found in the references [5, 6, 54], here we briefly go over its basics. It considers an abstract system consisting of three connected bodies, as shown in figure 3.2.

The three major elements of the system correspond to plenum (0), injection tube/swirler (1), and combustion chamber (2). An acoustic analysis was carried out, with the assumptions of:

- Only one-dimensional harmonic plane waves are present,
- Flow field follows low Mach number approximation,
- Mean flow and damping effects are ignored.

This model is composed of two parts, one for the acoustic analysis and another for the flame-pressure interactions. Both will be presented in the following paragraphs.

3.2.2.1 Acoustic analysis

With the model assumptions it can be shown that any flow variable a, such as pressure or velocity, follows the form:

$$a(x,t) = \tilde{a}(x) \cdot exp(-i\omega t) \tag{3.13}$$

where $\tilde{a}$ denotes the complex magnitude of the corresponding variable and ω is the system oscillation frequency. With appropriate boundary conditions for pressure and velocity at the interfaces between plenum, injector, and combustor as shown in Eq. (3.14), a matrix containing the modes of this system can be formed. Frequency of instability ω is solved from taking the eigenvalue of this matrix.

$$\widehat{u}_0(0) = 0; \tag{3.14a}$$

$$\widehat{P}_1(l_0) = \widehat{P}_0(l_0); \tag{3.14b}$$

$$S_1\widehat{u}_1(l_0) = S_0\widehat{u}_0(l_0); \tag{3.14c}$$

$$\widehat{P}_2(l_0 + l_1) = \widehat{P}_1(l_0 + l_1); \tag{3.14d}$$

$$S_2\widehat{u}_2(l_0 + l_1) = S_1\widehat{u}_1(l_0 + l_1); \tag{3.14e}$$

$$\widehat{P}_2(l_0 + l_1 + l_2) = \mathcal{Z}_2\widehat{u}_2(l_0 + l_1 + l_2). \tag{3.14f}$$

The system instability mode can be decomposed into two parts. The first part consists of the contribution from the elements containing the unburnt mixture (plenum and injector), and the second part consists of the contribution from the element containing the burnt mixture (combustor). These two parts interact with each other and determine the resultant system instability frequency. The strength of this interaction is found to be characterized by the "acoustic coupling index" Ξ:

$$\Xi = \frac{S_1}{S_2} \cdot \frac{\rho_b c_b}{\rho_u c_u} \,, \tag{3.15}$$

where S is the cross section area. Specifically, for $\Xi \ll 1$, the two bodies are essentially decoupled, which would allow us to characterize the modes of plenum-injector and combustor separately.

Firstly, we consider the mode of plenum and injector. The two elements can be approximated to be a large volume (plenum) connected to a narrow neck (injector), which are known to exhibit a Helmholtz-type resonance. In the long wave limit ($k_u^2 l_0 l_1 \ll 1$), this combined system follows the relationship:

$$1 - \frac{S_0}{S_1} k_u^2 l_0 l_1 \left[1 + \frac{1}{2}\frac{S_1}{S_0}\left(\frac{l_0}{l_1} + \frac{l_1}{l_0}\right)\right] = 0 \,. \tag{3.16}$$

In the case where $l_0/l_1 \sim 1$ and $S_1/S_0 \ll 1$, Eq. (3.16) reduces to the classical definition of Helmholtz characteristic frequency (ω_{H})[55]:

$$\omega_{\mathrm{H}}^2 \approx \frac{c_u^2 S_1}{V_0 l_1} \ . \tag{3.17}$$

We now look into the acoustic mode in the combustor. This mode and its influences on the overall system instability are strongly affected by the exit acoustic impedance ($\mathcal{Z}_2$) of the combustor chamber.

If $\mathcal{Z}_2 \to 0$, which is the case when the combustor exit is open to surrounding environment (or with very large nozzles), the combustor will develop longitudinal modes around the Helmholtz mode of plenum-injector. With the additional assumption of large plenum-to-injector volume ratio ($V_0/V_1 \gg 1$), the instability frequency ω of the overall system is given by:

$$1 - \left(\frac{\omega}{\omega_H}\right)^2 - \Xi \cdot \left(\frac{V_0}{V_1}\right)^{1/2} \cdot \tan\left(\frac{\omega l_2}{c_b}\right) \cdot \frac{\omega}{\omega_H} = 0 \ . \tag{3.18}$$

If $\mathcal{Z}_2 \to \infty$, which corresponds to an acoustically equivalent wall at the burner exit, the combustor will develop modes of half-wave type. And the instability frequency of the overall system is given by:

$$\left(1 - \frac{\omega^2}{\omega_H^2}\right) \cdot \tan\left(\frac{\omega l_2}{c_b}\right) + \Xi \cdot \left(\frac{V_0}{V_1}\right)^{1/2} \cdot \frac{\omega}{\omega_H} = 0 \ . \tag{3.19}$$

3.2.2.2 Flame describing function

The acoustic analysis above is based on the condition that there is no heat release rate fluctuation. If the effect of unsteady heat release is taken into consideration, then the continuity equation at the intersection between injection tube and combustion chamber Eq.(3.14e) needs to be replaced with:

$$\mathcal{K} S_2 \widehat{u_2}(l_0 + l_1) = S_1 \widehat{u_1}(l_0 + l_1) \tag{3.20}$$

where $\mathcal{K}$ is related to the Flame Describing Function (FDF), which represents the complex ratio of heat release rate fluctuation to velocity fluctuation, defined as:

$$\mathcal{F}(|\widehat{u}|, \omega) = G(\widehat{u}, \omega) e^{i\psi(\widehat{u},\omega)} = \frac{\widehat{\dot{Q}}(\widehat{u}, \omega)/\overline{\dot{Q}}}{\widehat{u}/\overline{u}}. \tag{3.21}$$

where G is the gain of the FDF and ψ is the phase angle between heat release and velocity fluctuation.

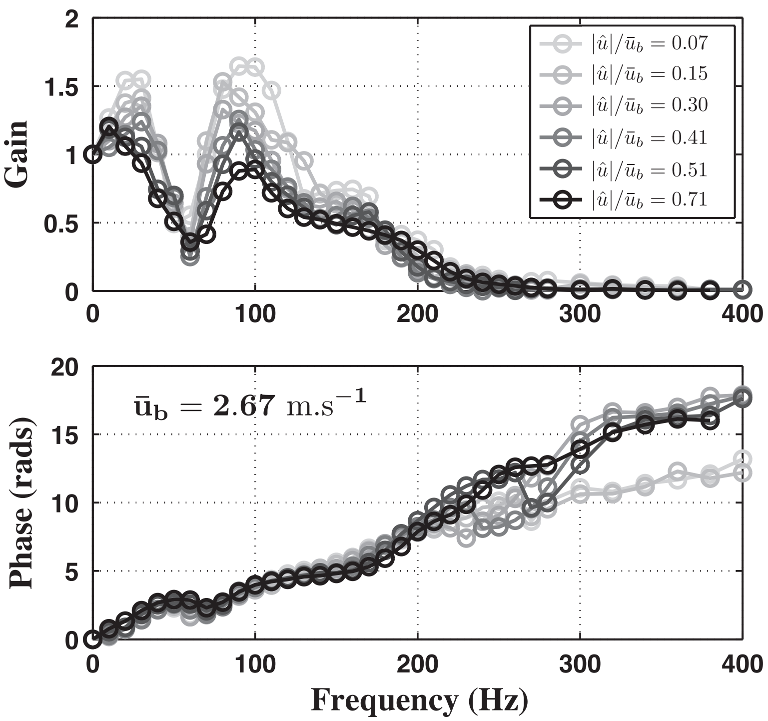

Figure 3.3: A sample Flame Describing Function (FDF) [6]

The FDF is usually obtained from experimental data. This is achieved by exciting a test burner over a wide range of frequencies with microphones, and measure the heat release and velocity fluctuations simultaneously. A sample FDF is shown in figure 3.3, with the gain (G in Eq. (3.21)) at the top and the phase angle (ψ in Eq. (3.21) at the bottom. We can see from figure 3.3 that the flame acts like a low pass filter. The heat release rate fluctuation induced by velocity fluctuation reaches maximum at the thermo-acoustic instability frequency. Afterwards the effect of velocity fluctuation decreases continuously as the frequency is increased. The phase angle between heat-release rate and velocity fluctuation on the other hand increases linearly as the excitation frequency increases.

3.2.3 Discussion of Reviewed Models

The two models reviewed in the previous sub-sections represent some of the most well developed reduced order models. They each have their own advantages as well as short-comings.

The MIT model is very general and comprehensive, it considers both the fluctuation of equivalence ratio and velocities. It also does not limit itself by any pressure fluctuation modes in the combustion chamber. However, because of its generality, the user has to pre-determine many parameters before applying this model. Additionally, the flame dynamics module of the model depends on the analysis of an anchored continuous flame, whereas in real world conditions the flame is mostly lifted and broken. Another issue is that the MIT model only considers the combustion chamber, in fact it assumes the upstream pressure disturbances are small. This may be challenged in a lot of configurations as well.

The EM2C model is discussed in the context of a more realistic configuration, where the combustion system is composed of a series of chambers (plenum, injector, combustion chamber, etc.). The acoustic analysis is elaborate and the flame describing function greatly increases its accuracy. However, in the current referenced work, the FDF has to be measured experimentally. Not all test burners are capable of installing the excitation mechanism and it only gets more difficult as the burner geometry gets closer to the real gas turbine engine configurations. The requirement of experimental calibration significantly impairs the model's practicality.

In view of the limitations of the two models reviewed, we realized that there is a need to develop a reduced order model that has the following capabilities:

- It should be established in a realistic configurations, namely it should consider not only combustion chamber but also upstream and downstream influences;
- It should depend on a minimal amount of input parameters and calibrations;
- It should be concise in formulation, ideally zero dimensional in space and quasi-steady in time.

It is to satisfy this set of goals, that we propose a new reduced order model in the next section.

3.3 The proposed "Michigan model" – Modular Reduced-order Model Framework (MRMF)

In view the of the areas that have the potentials to be improved in the reviewed models, here we propose a new reduced order model framework in an effort to address some of aforementioned issues. To distinguish it from the previously reviewed models ("MIT model" and "EM2C model"), we here name it as the Modular Reduced-order Model Framework (MRMF) or the "Michigan model". In this section we will talk about the general characteristics of this framework and some of the fundamental assumptions.

3.3.1 The modular approach

More often than not, a very good model developed for one burner configuration will lose its lure on another burner. This is usually caused by the fact that while developing a model, it is usually unavoidable to make some specific assumptions for particular physical processes associated with a specific part of the burner. When the model is applied to a different burner, which likely has different parts/geometry, those specific assumptions will be violated. As a result, the usefulness of the entire model is compromised.

In the meantime, if we take a close look at the different reduced order models, we can see that there are always some parts of each model whose assumptions are very reliable, hence are applicable to most of the applications. Therefore it seems a logical step to try to decompose a model into parts that are generally applicable and parts that are burner-specific. Then those generally applicable parts of the model can be reused to construct a new model for other burner configurations. This is less optimal because we still need burner-specific model, but at least we do not need to completely develop a new model each time.

However, even this is difficult. Traditionally models are developed in a layer by layer structure. What this means is that each part of the model depends on or is a result of the previous step (or layer). For example in the MIT model analysis reviewed in section 3.2.1.1, heat release rate fluctuation was given by:

$$Q'(t) = \overline{\kappa} \int_0^R \xi'(r,t)dr + d_\phi \phi'. \tag{3.4}$$

Both the validity of this equation and definition of its coefficient d_ϕ depends on the assumption made in the previous step, where the flame is assumed to be a continuous one anchored on a perforated plate, whose instantaneous flame location is given by:

$$\frac{\partial \xi}{\partial t} = u - v\frac{\partial \xi}{\partial r} - S_{\mathrm{u}}(\phi)\sqrt{\left(\frac{\partial \xi}{\partial r}\right)^2 + 1}. \tag{3.1}$$

If Eq.(3.1) does not hold true anymore, then the structure (dependent variables and order of differentiation) of Eq.(3.4) will be altered. Then the final equation of the MIT model (Eq.(3.12), originally shown in section 3.2.1.3) will take a different look. Now if we want to separate the flame dynamics analysis shown in Eq.(3.1) from Eq.(3.12) and still use other bits of the MIT model, the reader can understand the difficulty of doing it.

This example highlights the issue of adapting the existing models to newer setups. Because the assumptions of these models are tangled together with subsequent derivations, it is difficult to separate useful pieces out from the system. If we actually unwrap some of these models, we will realize that they are similar for the most part, with only one or two pieces different. But because of the way the model was presented in papers, they look quite different at the end. Therefore they are called "layer-by-layer" models for their overlapping structures.

This motivates us to develop the Modular Reduced-order Model Framework (MRMF). The core idea of this framework is being modular. Specifically:

- the framework shall consist of modules separated into several functional group, each functional group describe a key area of physics in instability, such as pressure fluctuation, heat release, etc.;
- each module represents a specific model for the functional group it belongs to, for example the pressure oscillation functional group may consist modules for standing wave, Helmholtz resonance, or vortex shedding;
- modules in each functional group should have the same interface in terms of input and output variables, to make themselves interchangeable;
- globally all modules across different functional groups should share minimal (or none at best) common assumptions, to be truly independent of each other;
- depending on the specific burner that the framework is applied to, appropriate modules are selected to fill in the seat of each functional group.

The differences between a "layer-by-layer" model and the proposed modular framework is further illustrated between figure 3.4 and figure 3.5.

A "layer-by-layer" model is like build a structure with different blocks of assumptions and models. In figure 3.4 the structure is similar to a pyramid with the governing equations being at the tip. The blocks are dependent on each other so much that if one block is removed, the entire structure will collapse. Moreover, after the structure is collapsed, we can't rebuild it if we replace one of the blocks with a new block of different size.

Such issues are not present in the modular framework shown in figure 3.5. If any module needs to be replaced, may it be an assumption or a primary/secondary model, another module or group of modules can be directly connected to the "branch". The re-integration process is greatly simplified.

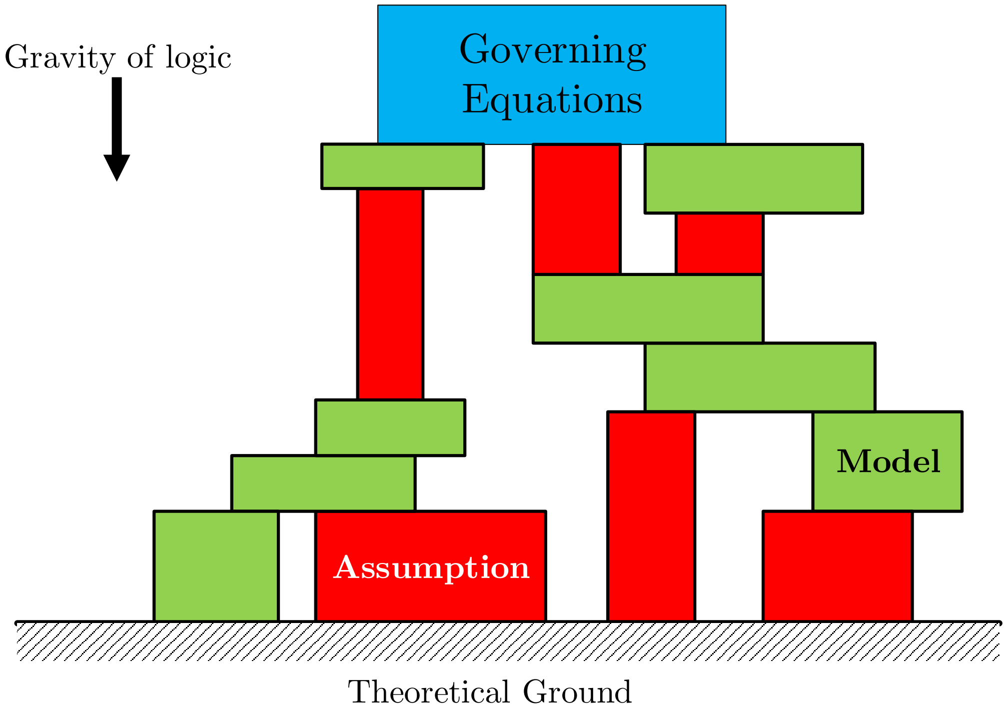

Figure 3.4: Illustration of traditional "layer-by-layer" model, red blocks represent assumptions and green blocks represent models.

If we take another example from the computer programming world, then a "layer-by-layer" model would be like writing a program that needs a million lines of code in one .c file. And in this file there is one main function (or driver) without any subroutine/functions. The readability of the code is impaired by the tangled internal referencing of variables, so that no parts of it can be used if another similar program needs to be written. On the other hand, if we have use a modular framework, we would divide the one million lines of code into numerous files each with a designated function. The functions that perform a specific job will be treated as a library. Next time if we need to write a new program, we only need to write a new driver that links different libraries. And that is the difference of writing 1 million + 50 lines of code instead of 2 million lines of code.

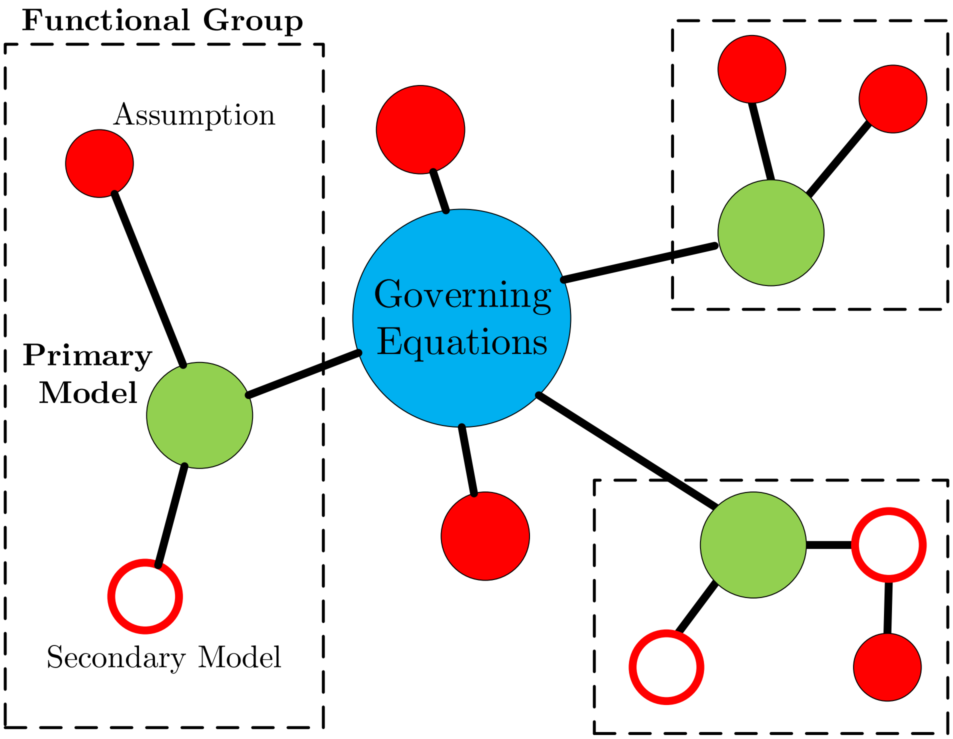

Figure 3.5: Illustration of proposed modular framework, green circles are primary models, white circles are secondary models, red circles are assumptions.

3.3.2 Configuration considered in this work – the DLR Gas Turbine Model Combustor (GTMC)

Next, we will try to construct this framework based on one specific problem. The burner that we will build our modular framework upon in this work is the Gas Turbine Model Combustor (GTMC) designed by Meier et al.[7] at DLRin Stuttgart. A schematic drawing of the GTMC is shown in figure 3.6, here we will only provide a qualitative description of the system, technical details of this burner will be provided in section 4.2.

The GTMC contains two swirling air streams, which surround an annular fuel stream, in a plenum-injector-combustor three component setup. It has the advantage of a canonical axisymmetric swirler-design, yet still exhibiting the fundamental physics associated with flames in gas turbine engine combustors. Comprehensive measurements have been conducted at DLR Stuttgart by Meier and colleagues. These measurements yield an elaborate database in terms of flow structures and flame characteristics for varying operating conditions, which makes this setup well calibrated for additional investigations. One key feature of the GTMC is that under certain

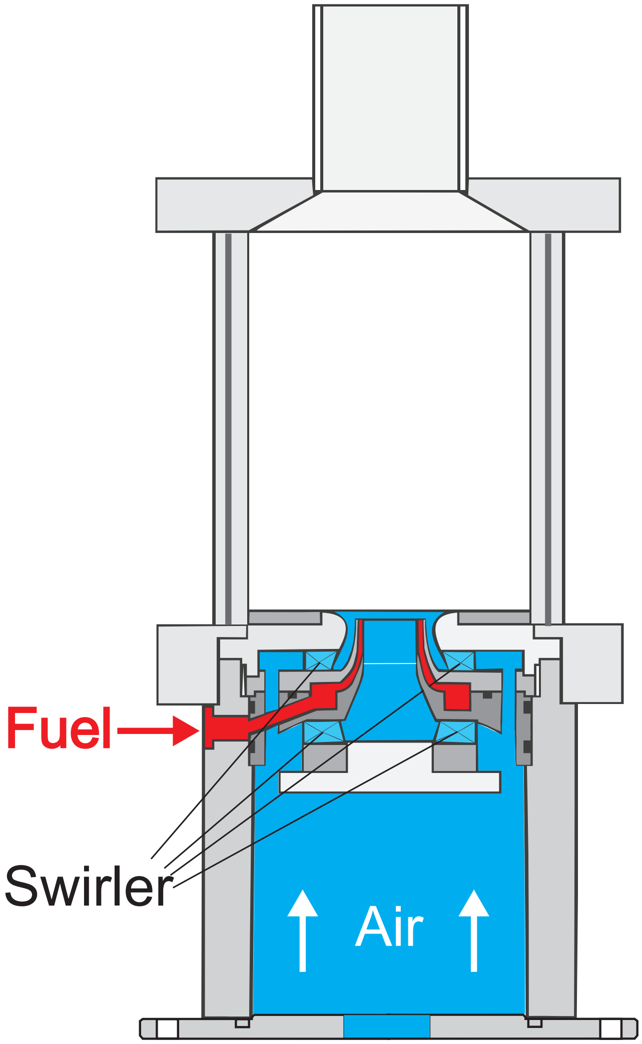

Figure 3.6: Schematic drawing of the GTMC[7]

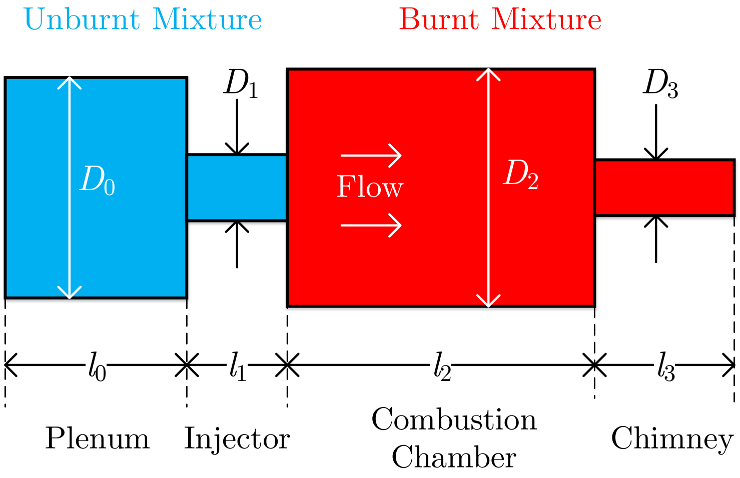

Figure 3.7: Schematic of the present reduced order model

fueling conditions, a self-sustained combustion instability would be established in the system. Hence the target of our framework is to model the combustion instabilities in the GTMC.

3.3.3 GTMC abstraction and framework setup

To be able to consider the complex GTMC in the view of a reduced order model, its complexity has to be reduced to a manageable form. Here GTMC is considered as a system consisting of four connected bodies, as shown in figure 3.7. Here the four major elements of the system correspond to (0) plenum, (1) injector/swirler, (2) combustion chamber, and (3) chimney. This configuration also resembles that of a real world gas turbine engine. Even though it is not a one-to-one correspondence, one can roughly regard plenum as the pre-mixing/buffer chamber after high pressure compressor in real engines, the injector and combustion chamber are similar to their counterparts in real engines, and the chimney corresponds roughly the veins leading to the turbines.

To construct our framework, we have to set a series of fundamental assumptions shared by all modules that are inviolable as long as the framework is used:

- the system elements are assumed to be zero dimensional in space. All gas properties (pressure, temperature, etc.) are uniform within each element;
- the system is operated at low Mach numbers, no compressibility effects are considered.

With these assumptions, we look into the physical processes of the instability. As reviewed in section 1.3, combustion instabilities are related to the coupling of pressure oscillations and heat release oscillation. In most cases, these two are not directly related, but linked via velocity instead. Hence our framework is constructed with three major functional groups: *i*) Pressure oscillation (P); *ii*) Heat release oscillation (Q); and *iii*) velocity coupling (V). A diagram of this framework is presented in figure 3.8. The modules occupying each functional group is discussed in the following sections of this chapter.

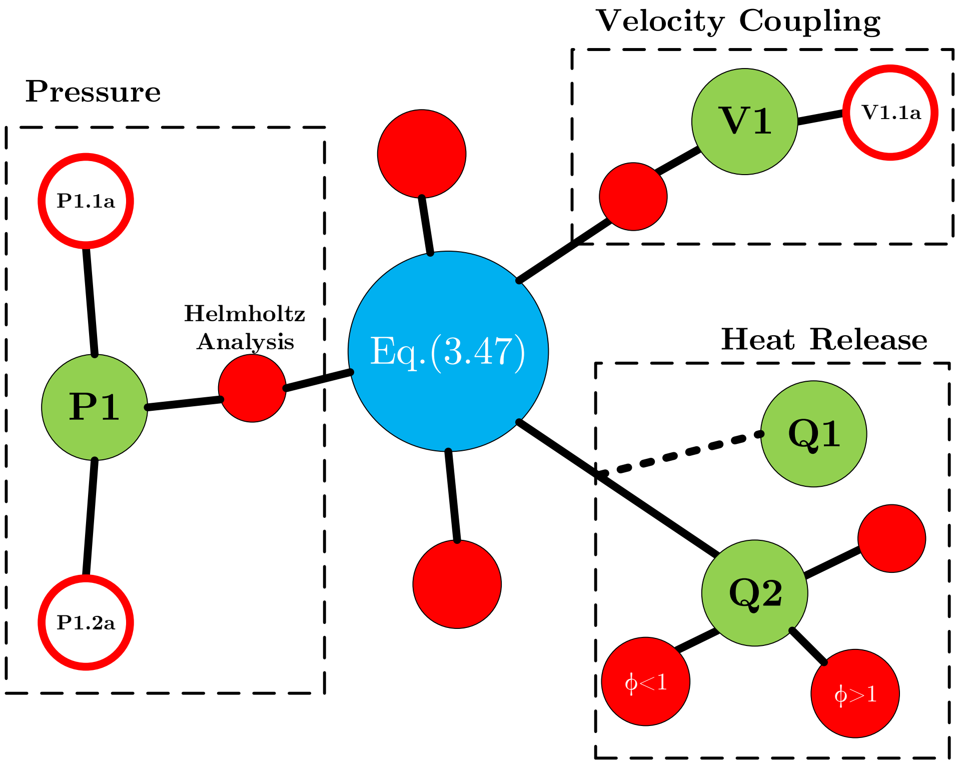

Figure 3.8: Framework schematics of MRMF applied to GTMC, legend follows that of figure 3.5

3.4 Pressure Modeling in MRMF

In this section we will introduce the modules in the pressure oscillation functional group. First we will present the Helmholtz analysis (*Module P1*) and then we will introduce two of its auxiliary modules for parameter estimation (*Module P1.1a* and *Module P1.2a*)

3.4.1 Pressure equations (*Module P1*)

Two of the larger elements of the system, plenum and combustion chamber, are assumed to be Helmholtz resonators. A simple Helmholtz resonator behaves like a forced oscillator, and we can write the governing equation for the pressure fluctuations (P') in the form (Eq.(10.8.6) in Kinsler et al. [55]):

$$\frac{d^2P'}{dt^2} + 2\zeta \cdot \omega_{\text{res}} \cdot \frac{dP'}{dt} + \omega_{\text{res}}^2 \cdot P' = f_{\text{ext}} \ , \tag{3.22}$$

where ω_{res} is the system resonance frequency and f_{ext} is the driving force. For example, in a chamber with internal heat release, the mass and energy conservation equations can be written as:

$$V\frac{d\rho}{dt} = \dot{m}_{\text{in}} - \dot{m}_{\text{out}} \ , \tag{3.23a}$$

$$V\frac{d(\rho e)}{dt} = \dot{m}_{\text{in}}\left(h_{\text{in}} + \frac{u_{\text{in}}^2}{2}\right) - \dot{m}_{\text{out}}\left(h_{\text{out}} + \frac{u_{\text{out}}^2}{2}\right) + V \cdot \dot{Q} \ , \tag{3.23b}$$

where the subscripts “in” and “out” indicate the inlet and outlet streams. If we substitute density ρ with pressure P, and substitute enthalpy h with temperature T, then linearize Eq.(3.23), we would have an equation in the form of Eq. (3.22) with the heat release rate fluctuation, which takes the form of $(\gamma-1)/V \cdot d\dot{Q}'/dt$, as the driving force [4, 56]. Follow the same line of logic, if we assume the combustion chamber pressure oscillations P_2' is the driving force for the plenum pressure fluctuations P_0', then the governing equations for P_0' and P_2' can be written as:

$$\frac{d^2P_0'}{dt^2} + 2\zeta_0 \cdot \omega_0 \cdot \frac{dP_0'}{dt} + {\omega_0}^2 \cdot P_0' = {\omega_0}^2 \cdot P_2' \ , \tag{3.24a}$$

$$\frac{d^2P_2'}{dt^2} + 2\zeta_2 \cdot \omega_2 \cdot \frac{dP_2'}{dt} + {\omega_2}^2 \cdot P_2' = \frac{\gamma_{\text{b}} - 1}{V_2} \cdot \frac{d\dot{Q}'}{dt} \ . \tag{3.24b}$$

3.4.2 Helmholtz frequencies (*Module P1.1a*)

The Helmholtz resonance frequencies of plenum and combustion chamber can be calculated from classical definitions of Helmholtz resonance frequencies [4]:

$$\omega_0 = \sqrt{\frac{c_\mathrm{u}^2 S_1}{V_0 l_1}} \tag{3.25a}$$

$$\omega_2 = \sqrt{\frac{c_\mathrm{u}^2 S_1}{V_2 l_1} + \frac{c_\mathrm{b}^2 S_3}{V_2 l_3}} \tag{3.25b}$$

Note that here the end correction to the characteristic length of the neck in typical Helmholtz analysis is not applied.

3.4.3 Damping ratios (*Module P1.2a*)

Next, we need to estimate the damping ratios ζ_0 and ζ_2. If we only consider the effects of acoustic radiation loss, then the damping ratio of a simple Helmholtz resonator can be estimated by [55]:

$$\zeta_0 = \frac{\omega_0 V_0}{4\pi C_\mathrm{u}^3} \cdot \omega^2 \,, \tag{3.26}$$

where C_u is the speed of sound of the unburnt mixture in plenum and injector.

An order-of-magnitude analysis reveals that the value of ζ_0 is in the range of 10^{-3}, so is ζ_2. It can be expected that at such small values, the precise value of damping ratios will have less effect on the system instability frequency magnitude.

3.5 Heat Release Modeling in MRMF

To solve Eq.(3.24), we need to relate the heat release rate fluctuation to pressure fluctuations. The total heat release rate $\dot{Q}$ can be related to the total mass flow rate ($\dot{m}_\mathrm{tot}$) and lower heating value ($\Delta h_\mathrm{g}^\circ$) of fuel-air mixture by:

$$\dot{Q} = \dot{m}_\mathrm{tot} \cdot \Delta h_\mathrm{g}^\circ \cdot \frac{\min(\phi, 1)}{\phi + AFR_\mathrm{st}} \,, \tag{3.27}$$

where equivalence ratio ϕ and stoichiometric air-fuel ratio (AFR_st) are related to fuel flow rate ($\dot{m}_\mathrm{f}$) and air flow rate ($\dot{m}_\mathrm{a}$) by:

$$\phi = \frac{\dot{m}_\mathrm{f}}{\dot{m}_\mathrm{a}} \cdot AFR_\mathrm{st} \,. \tag{3.28}$$

The "minimum" function (min) in Eq.(3.27) is used to consider the fact that at non-stoichiometric conditions, there will be unburnt fuel or air depending on ϕ. Eq. (3.27) follows a simple one step chemistry concept, partial decomposition of fuel and intermediate reactants are not considered for the simplicity of the model. From here we look into the fluctuations of heat release. To do this, we first define the decomposition of variables into mean ($\overline{x}$) and fluctuation(x') as:

$$x = \overline{x} + x' \ , \quad \text{with} \quad \overline{x'} = 0 \ . \tag{3.29}$$

Depending on the configuration of the device that we are modeling, the form of heat release rate fluctuation $\dot{Q}'$ will be different.

3.5.1 Premixed combustion (*Module Q1*)

In premixed combustion devices, fuel and air are normally well mixed in the upstream. In this case the equivalence ratio can be regarded as being constant. Then we can apply the decomposition method defined in Eq.(3.29) to Eq.(3.27), yielding:

$$\dot{Q}' = \left[\Delta h_{\mathrm{g}}^{\circ} \cdot \frac{\min(\phi, 1)}{\phi + AFR_{\mathrm{st}}} \right] \cdot \dot{m}'_{\mathrm{tot}} \ , \tag{3.30}$$

which indicates that the heat release rate fluctuation is directly proportional to fuel-air mixture flow rate fluctuation $\dot{m}'_{\mathrm{tot}}$.

3.5.2 Partially premixed combustion (*Module Q2*)

In most partially premixed combustion applications, the air still passes through chambers with large internal dimensions, but fuel is normally injected from narrow fuel lines by high pressure. In this case, we can consider the pressure fluctuations in the combustion chamber has minimal effect on fuel flow rate, i.e. $\dot{m}_{\mathrm{f}}$ is constant. If we recognize that the total mass flow rate $\dot{m}_{\mathrm{tot}} = \dot{m}_{\mathrm{f}} + \dot{m}_{\mathrm{a}}$, and combine Eq.(3.27) with Eq.(3.28), we will arrive at:

$$\dot{Q} = \frac{\Delta h_{\mathrm{g}}^{\circ}}{AFR_{\mathrm{st}}} \cdot \min(\dot{m}_{\mathrm{f}} \cdot AFR_{\mathrm{st}}, \dot{m}_{\mathrm{a}}) \ , \tag{3.31}$$

We can re-write Eq.(3.31) into a different form:

$$\dot{Q} = \frac{\Delta h_{\mathrm{g}}^{\circ}}{AFR_{\mathrm{st}}} \cdot \min(\phi, 1) \cdot \dot{m}_{\mathrm{a}} \ , \tag{3.32}$$

Apply the decomposition defined in Eq.(3.29) to Eq.(3.32), we will see that for partially premixed combustion, the heat release rate fluctuation $\dot{Q}'$ will be:

$$\dot{Q}' = \frac{\Delta h_{\mathrm{g}}^{\circ}}{AFR_{\mathrm{st}}} \cdot \left[\underbrace{\Big(\min(\phi,1) - \overline{\min(\phi,1)} \Big) \cdot \overline{\dot{m}_{\mathrm{a}}}}_{\substack{\text{Contribution of equivalence} \\ \text{ratio fluctuation}}} + \underbrace{\Big(\min(\phi,1) \cdot \dot{m}_{\mathrm{a}}' - \overline{\min(\phi,1) \cdot \dot{m}_{\mathrm{a}}'} \Big)}_{\substack{\text{Contribution of air flow} \\ \text{rate fluctuation}}} \right] . \tag{3.33}$$

As shown in Eq.(3.33), in partially premixed combustion, the heat release rate fluctuation is related to both air flow rate oscillation and equivalence ratio fluctuations. The effect of each has to be analyzed based on the instantaneous equivalence ratio ϕ. This is discussed next.

3.5.2.1 Fuel-rich mixture

The first case that we look at is a fuel-rich mixture in which the minimum point of the fluctuating equivalence ratio is still larger than unity ($\min(\phi) > 1$). In this case, we have $\min(\phi, 1) \equiv 1$, hence Eq.(3.33) can be simplified to:

$$\boxed{\dot{Q}' = \frac{\Delta h_{\mathrm{g}}^{\circ}}{AFR_{\mathrm{st}}} \cdot \dot{m}_{\mathrm{a}}'} \, . \tag{3.34}$$

which is equivalent to Eq.(3.30) in the case of $\min(\phi, 1) = 1$. This means that in a fuel rich mixture, the controlling factor of heat release rate is the air flow rate.

3.5.2.2 Fuel-lean mixture

The second case that we look at is a fuel-lean mixture in which the maximum point of the fluctuating equivalence ratio is always smaller than unity ($\max(\phi) < 1$). In this case $\min(\phi, 1) \equiv \phi$ and equivalently:

$$\min(\dot{m}_{\mathrm{f}} \cdot AFR_{\mathrm{st}}, \dot{m}_{\mathrm{a}}) \equiv \dot{m}_{\mathrm{f}} \cdot AFR_{\mathrm{st}} . \tag{3.35}$$

It is easier in this case to derive the heat release fluctuation from Eq. (3.31). If we substitute the minimum function in Eq. (3.31) with Eq. (3.35), then it would take the form:

$$\dot{Q} = \Delta h_{\mathrm{g}}^{\circ} \cdot \dot{m}_{\mathrm{f}} \, . \tag{3.36}$$

Because we assume in the partially premixed configuration that fuel flow rate is not affected by combustion instabilities, all quantities on the RHS of Eq. (3.36) are constants. This leads to the conclusion that:

$$\boxed{\dot{Q}' \equiv 0} \, . \tag{3.37}$$

This result states that when the mixture is very lean, the heat release rate is controlled by the fuel flow rate. And if the fuel flow rate is constant in combustors operating in the very lean regime ($\min(\phi, 1) \equiv \phi$), the heat release rate is constant under our current assumption.

3.5.2.3 Near-stoichiometric mixture

If a mixture whose equivalence ratio is close to unity ($\min(\phi) < 1$, $\max(\phi) > 1$), then there will not be a simplification available like the ones shown in previous two sub-sections. In this case, the full equation of Eq.(3.33) has to be solved at any instant. Heat release rate will stay constant in the instances of lean mixtures and vary in the instances of rich mixtures.

3.6 Velocity Coupling Modeling in MRMF

In the two sections above, we have stated the governing equations for pressure (section 3.4) and heat release (section 3.5). Now we need to relate these two quantities via velocity coupling.

3.6.1 Coupling of heat release with velocity (*Module V1*)

In the cases where we have non-zero heat release rate fluctuations, both Eq. (3.30) and Eq.(3.34) indicate that $\dot{Q}'$ is directly proportional to mixture or air mass flow rates. In the present model, the fluctuation of mass flow rate can be related to the fluctuation of swirler exit velocity (U_1') with a convection time delay (τ_c):

$$\dot{m}_*' = U_1'(t - \tau_\mathrm{c}) \cdot \rho_\mathrm{u} \cdot S_1 \, . \tag{3.38}$$

where $\dot{m}_*$ is $\dot{m}_\mathrm{tot}$ for fully premixed combustors or $\dot{m}_\mathrm{a}$ for partially premixed combustors that have dedicated fuel injection.

Additionally, through the continuity equation, injector velocity fluctuations are related to the pressure differences across the injector in a simple form [4]:

$$\frac{dU_1'}{dt} = -\frac{1}{\rho_\mathrm{u}} \frac{dP_1}{dx} \approx \frac{P_0' - P_2'}{\rho_\mathrm{u} \cdot l_1} \, . \tag{3.39}$$

Again, as stated in our assumptions in section 3.3.3, the complex flow pattern across the swirler veins in the injector are neglected. Combining Eq. (3.38) with Eq. (3.39), we will have a relation between the mass flow rates of mixture or air, to which heat release is related, and pressure fluctuations in the form:

$$\frac{d\dot{m}'_*}{dt} = \frac{S_1}{l_1} \cdot (P'_0 - P'_2)|_{t\, -\, \tau_c} \ . \tag{3.40}$$

3.6.2 Estimation of convection time delay (*Module V1.1a*)

One key parameter in Eq. (3.40) is the convection time delay τ_c. This time delay represents the time for the disturbance in the injector to travel to the flame location to affect the local mass flow rate. If the idea of zero-dimensional modeling laid out in section 3.3.3 is strictly adhered to, confusion may arise. In the case of zero-dimensional modeling all properties are uniform in each system element, i.e. the speed of sound is infinite, hence the disturbances at the injector should be communicated to the combustion chamber instantaneously. However, we shall be aware that a convection delay is a very reasonable assumption and an important part of the dynamic process of instability. So we have to create this concept using some of the multi-dimensional arguments in the context of a zero-dimensional framework. The time delay is just a single number without any spatial or temporal dependency, so in a dimensional sense it should be consistent with the other modules.

The convection time delay is estimated to be the ratio between mean flame lift off height ($\overline{H_{\text{fl}}}$) and mean axial velocity in the combustion chamber ($\overline{U_2}$):

$$\tau_c = \frac{\overline{H_{\text{fl}}}}{\overline{U_2}} \ . \tag{3.41}$$

We acknowledge that in a turbulent flame, the lift off height and velocity are highly unsteady spatially and temporally. But for the simplicity of the model, here the average of both are used for estimation.

3.7 Framework Integration for Application to GTMC

In the preceding sections we have presented the basic modules that are currently developed for application in the GTMC. In this section we will integrate them together to build an organic prediction tool for later use.

The modules that we selected for this study is:

- Pressure oscillation: *Module P1*: Eq.(3.24) + *Module P1.1a*: Eq.(3.25) + *Module P1.2a*: Eq.(3.26);
- Heat release oscillation: *Module Q2*: section 3.5.2;
- Velocity coupling: *Module V1*: Eq.(3.40) + *Module P1.1a*: Eq.(3.41)

Notice that in heat release modeling part, we choose the partially premixed combustion formulation (*Module Q2*, section 3.5.2) over the premixed combustion formulation (*Module Q1*, section 3.5.1). This is because the fuel nozzles in the GTMC have very small diameters, hence the acoustic impedance of the fuel nozzles are large compared to that of the air swirler. In real experiments there are also one-way valves placed on the fuel line input ports, which prevents any reversed flow in the fuel line. As a result, the reality of GTMC fits the condition of partially premixed combustion with fuel injection as assumed in *Module Q2*.

If we combine the velocity coupling (Eq.(3.40)) with the heat release equations (section 3.5.2), then we have:

$$\frac{d\dot{Q}'}{dt} = \begin{cases} 0 & \text{if } \max(\phi) < 1 \\ \text{intermittent} & \text{if } \min(\phi) < 1,\ \max(\phi) > 1 \\ \frac{\Delta h_{\text{g}}^{\circ}}{AFR_{\text{st}}} \cdot \frac{S_1}{l_1} \cdot (P_0' - P_2')|_{t\,-\,\tau_{\text{c}}} & \text{if } \min(\phi) > 1 \end{cases} \tag{3.42}$$

The dependency of the heat release rate fluctuation rate on equivalence ratio is discussed in section 3.5.2. Now we consider only the last case of Eq. (3.42), where we have consistently lean mixture. Then substitute Eq. (3.42) into Eq. (3.24), we have:

$$\boxed{\begin{aligned} &\frac{d^2P_0'}{dt^2} + 2\zeta_0 \cdot \omega_0 \cdot \frac{dP_0'}{dt} + {\omega_0}^2 \cdot P_0' = {\omega_0}^2 \cdot P_2' \,, \\ &\frac{d^2P_2'}{dt^2} + 2\zeta_2 \cdot \omega_2 \cdot \frac{dP_2'}{dt} + {\omega_2}^2 \cdot P_2' = \mathcal{L} \cdot \Theta \cdot (P_0' - P_2')|_{t\,-\,\tau_{\text{c}}} \,, \end{aligned}} \begin{matrix} (3.43\text{a}) \\ (3.43\text{b}) \end{matrix}$$

with $\mathcal{L}$ representing all parameters that are burner specific:

$$\mathcal{L} = \frac{\gamma_{\text{b}} - 1}{V_2} \cdot \frac{S_1}{l_1} \,, \tag{3.44}$$

and Θ representing all parameters that are fuel specific:

$$\Theta = \frac{\Delta h_{\text{g}}^{\circ}}{AFR_{\text{st}}} \,. \tag{3.45}$$

Now we make the assumption that the pressure in the plenum and the combustion chamber are sinusoidal:

$$P'_0 = \widehat{P'_0} \cdot \exp(\jmath\omega t)\ , \quad P'_2 = \widehat{P'_2} \cdot \exp\left(\jmath(\omega t - \psi_{20})\right)\ , \tag{3.46}$$

where ψ_{20} is the phase angle between P'_0 and P'_2. This should be reasonable for a normal Helmholtz analysis, and this will be verified in the later sections. Substitute Eq. (3.46) into Eq. (3.43), we would obtain:

$$\boxed{\begin{aligned} -\omega^2 + 2\zeta_0 \cdot \omega_0 \cdot \jmath\omega + {\omega_0}^2 &= \frac{{\omega_0}^2}{\Pi}\ , \\ -\omega^2 + 2\zeta_2 \cdot \omega_2 \cdot \jmath\omega + {\omega_2}^2 &= \mathcal{L} \cdot \Theta \cdot \exp(-\jmath\omega_{\mathrm{r}}\tau_{\mathrm{c}}) \cdot (\Pi - 1)\ , \end{aligned}} \qquad \begin{aligned} &(3.47\mathrm{a}) \\ &(3.47\mathrm{b}) \end{aligned}$$

where Π is the complex ratio of the two pressure fluctuations defined as:

$$\Pi = \frac{P'_0}{P'_2} = \frac{\widehat{P'_0}}{\widehat{P'_2}} \cdot \exp(\jmath\psi_{20})\ . \tag{3.48}$$

In Eq. (3.47) the only unknowns are the system instability frequency ω and complex pressure ratio Π, all other parameters can be estimated from the configuration and operating conditions that this model is applied to. Hence mathematical closure is achieved.

Equations (3.43) and (3.47) take a similar level of complexity to the MIT model and EM2C model that we have reviewed. However, what sets the MRMF apart is not the end result, but rather the way of constructing these equations. Our claim of modular concept is fulfilled by the fact that if one of our modules is proved to be inadequate, only that specific part needs to be taken out, without affecting any other module in our model. Even though the end result – the governing equations may change accordingly, the process of switching modules should take minimal time.

Now we have laid out the framework and derived the governing equations for the application of MRMF on GTMC, the capability of this model in predicting key parameters and describing experimental observations still remains to be seen. This will be addressed in the next chapter.

CHAPTER IV

Assessment of MRMF on the Gas Turbine Model Combustor (GTMC) – Part 1: frequency and amplitude of pressure

4.1 Introduction

Models and theories are the brain-children of combustion researchers. They can only reach their intellectual "adulthood" after being examined by real world experiments. In the previous chapter we have indicated that the example framework that we have developed in this thesis is tailored to model the combustion instability of the DLR Gas Turbine Model Combustor. In section 3.3.2 we also had a brief introduction of the GTMC. The key features of the GTMC, as previously mentioned, are its inherent combustion instability at certain conditions and its great accessibility for optical diagnostic tools.

Another advantage of the GTMC is that it is very well calibrated. Comprehensive measurements have been conducted at DLR Stuttgart by Dr. Wolfgang Meier and colleagues. These measurements yield an elaborate database in terms of flow structures and flame characteristics for various operating conditions, which makes this setup suitable for comparisons with models or additional investigations.

Since the design of the GTMC was generally shared, the research group headed by Prof. Driscoll replicated the burner and installed it at Michigan. Now besides the existing data-base that the DLR group has published, we have the additional flexibility to investigate aspects of the burner that has not been previously examined. This was the rationale behind our selection of the GTMC as our modeling target.

One of the remaining issues of the GTMC is to determine the mode of instabilities in the combustion chamber. Both Steinberg et al. [8, 57] (at DLR) and Allison et al. [9] (at Michigan) have made extensive investigations on the thermal acoustic instabilities shown in the GTMC, and most evidences have indicated that the combustion chamber exhibits a Helmholtz mode. Steinberg[8] showed that measurements at three points along the pole of the combustion chamber returns identical pressure traces. However, the spacial distribution of pressure signals, such as in the azimuthal direction, was not further investigated. In the meantime, Allison et al.[9] showed that the combustion instability has a dependency on the geometry of the burner that was not entirely explainable by the Helmholtz theory.

In this chapter, we set out to tackle these unresolved issues. Specifically, in section 4.2 and section 4.3 we will provide further technical information of the GTMC geometry as well as key results of the studies done by Steinberg et al. and Allison et al. Then in section 4.4 we will present our experimental characterization of the pressure mode of the combustion chamber. This is very important because our MRMF constructed in last chapter was based on Helmholtz analysis, this experimental study will assess the validity of our key model assumptions. In section 4.5 we will use our MRMF model to predict the trends of the changes of frequency and amplitudes of pressure in GTMC when certain parameters are varied. These predictions will be compared with the experimental data in literature. This chapter will close with conclusions of our investigations of pressure oscillations.

4.2 Details of the DLR Gas Turbine Model Combustor

The GTMC contains two swirling air streams, which surround an annular fuel stream in a plenum-injector-combustor three component setup. The injector of the GTMC consists of a central air nozzle, an annular fuel nozzle, and a co-annular air nozzle. Both air nozzles supply swirling dry air at atmospheric pressure and temperature from a common plenum. The inner air nozzle has an outer diameter of 15 mm and the annular nozzle has an inner diameter of 17 mm and an outer diameter of 25 mm. The measured swirl number is approximately 0.55. Non-swirling fuel is provided through three exterior ports fed through the annular nozzle which is subdivided into 72 channels of dimension 0.5 mm × 0.5 mm. The exit plane of the central air nozzle and fuel nozzle lies 4.5 mm below the exit plane of the outer air annulus. The exit plane of the outer air annulus will be referred to as the burner surface. The combustion chamber has a square cross section of 85mm in width and 110 mm in height. The exit of the burner has a tapered lid which leads to an exhaust chimney with a diameter of 40 mm and a height of 50 mm. The burner is operated with fused silica windows, with a thickness of 1.5 mm, for flame visualization. In the

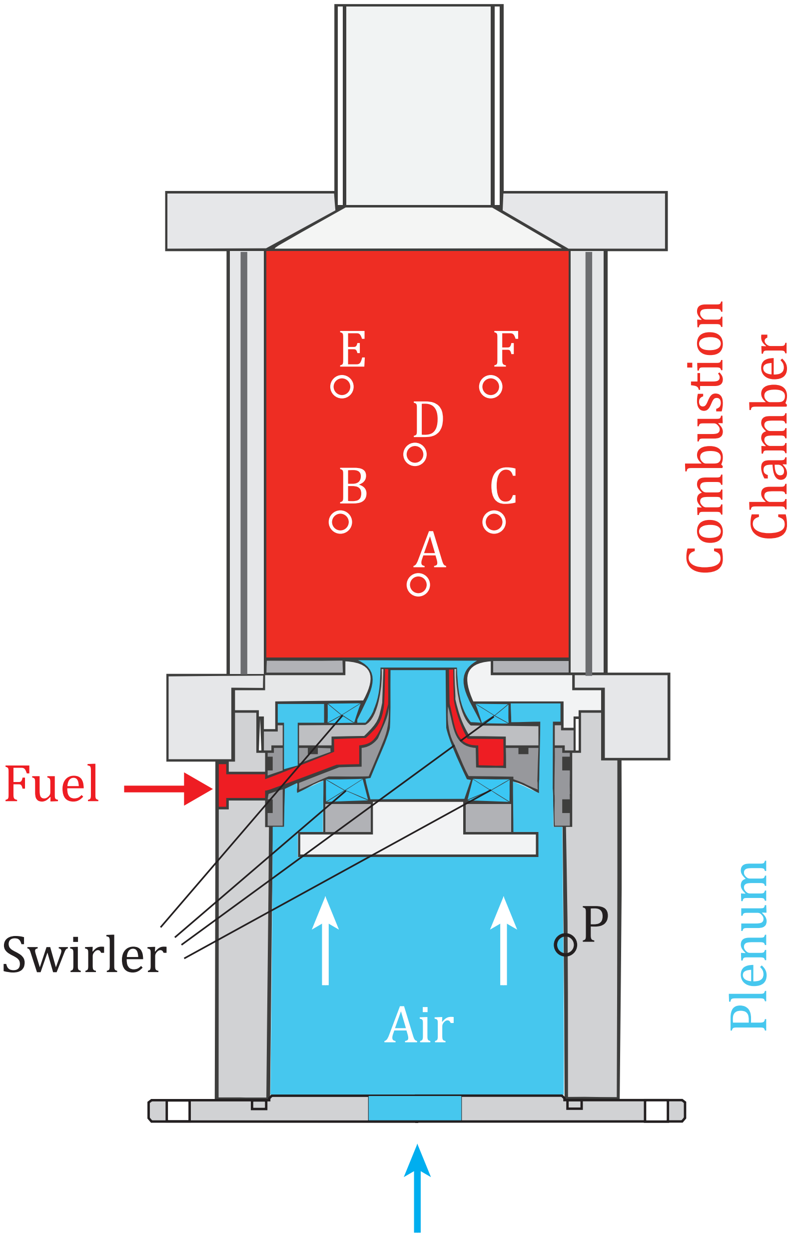

Figure 4.1: Schematic drawing of the GTMC[7], with the pressure measurements points labeled

present study the burner uses Dimethyl Ether (DME) as fuel. An external cylindrical chamber is used for the equal division of the fuel flow into three separate lines which lead to the fuel ports on the burner. Mass flow rates for air and fuel lines are controlled by sonically choked orifices.

4.3 Review of Previous Pressure Measurements on the GTMC

Published literature of investigations on GTMC date back as far as 2003 [58, 59]. Since then a long list of DLR publications have addressed some aspects of the GTMC. These include species and velocity fields [7, 60], flame-flow interactions [61], precessing vortex core structures [62], vortex-flame interactions [63], and thermal-acoustic coupling [64, 8]. For a more detailed review of these DLR, please refer to Section 1.3 (pp. 28) of Dr. Patton Allison's thesis [65]. Here we discuss some of the results that are relevant to our current studies of thermo-acoustic instability mode.

4.3.1 Previous measurements at DLR

In Steinberg et al.'s 2010 studies [64] two microphones were mounted onto the GTMC to measure the phase differences between combustor and plenum. It was reported that the instability frequency measured in these two locations were identical and the two pressure signals had a phase shift of about 85°.

In a later study in 2012 [8], Steinberg et al. revised the phase differences between plenum and combustion chamber to about 60°. Three additional pressure ports were drilled onto the combustion chamber pole at different heights. The traces of pressure measured in combustion chamber and plenum separately are said to "follow similar" trends. Steinberg et al. claimed that this agrees with a multi-chamber Helmholtz analysis, which was further proved by Comsol simulations. Figure 4.2 shows the pressure traces of combustion chamber and plenum in the work of Steinberg et al. [8].

4.3.2 Previous measurements at Michigan by Allison

The investigation of combustion instability mode on GTMC was later thoroughly carried out in Michigan by Allison et al. [9]. Specifically he investigated the effect of varying geometry parameters, flow rates, and equivalence ratio for various fuels. One of his discoveries is that the instability frequency has a strong dependence on plenum volume as well as exhaust tube (chimney) dimensions. The dependence of resonance frequency on geometrical parameters are detailed in figure 4.3.

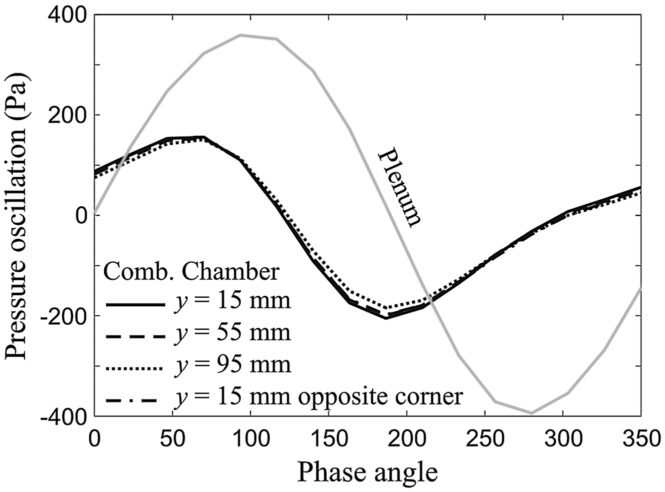

Figure 4.2: Pressure measurements in both combustion chamber and plenum in Steinberg et al.'s work [8]

In a later work, Allison et al. investigated those parameters on a DME flame [10]. The results show that DME flames behave similar to other fuels in terms of dependency of frequency on equivalence ratio and mass flow rates. The instability frequency of all fuels is shown to be mostly proportional to the air mass flow rate, as shown in figure 4.4. Another important aspect of this later work is the investigation of a quiet flame at $\phi = 0.75$ and a resonating flame at $\phi = 1.2$. This is detailed in table 4.1. At $\phi = 0.75$ the pressure oscillation amplitude is very small that an accurate determination of instability was not quite possible.

Table 4.1: Flame surface response at different equivalence ratio by Allison et al. [10]

Fuel Type	DME	DME	DME
Air flow rate [g/min]	282	282	282
ϕ	0.75	1	1.2
Instability present	No	Yes	Yes
Acoustic Frequency [Hz]	N/A	310	320
FSD Frequency [Hz]	10	310	320

4.4 Current Pressure Measurement on the GTMC: Mode, Correlations, and Frequencies

As discussed in the previous sections, one of the key remaining issues of GTMC was to confirm the pressure mode of the combustion chamber. Before we can use our MRMF to describe the trend observed in Allison et al.'s work in previous section,

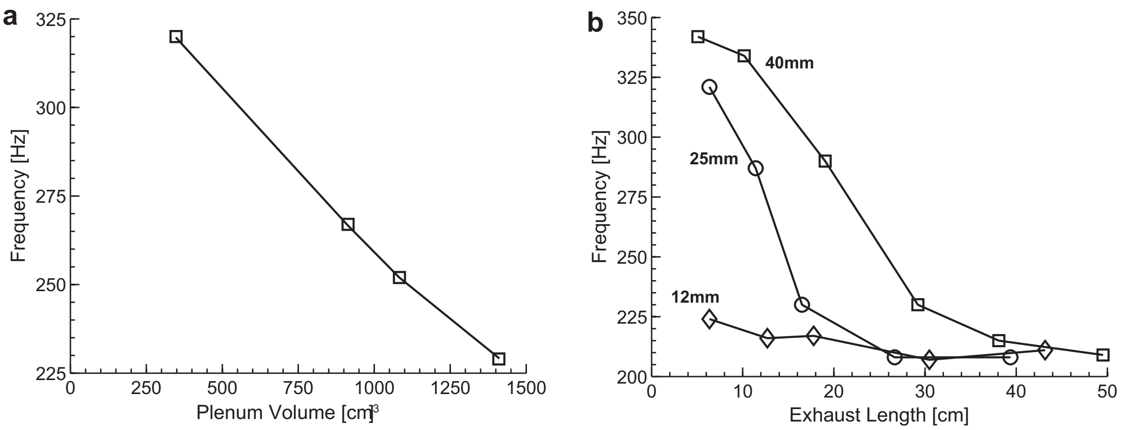

Figure 4.3: Frequency response to burner configuration variations in Allison et al.'s work [9].(a) Effect of varying plenum volume; (b) effect of varying exhaust tube length with varies tube diameters: 40 mm, 25 mm, and 12 mm.

we will have to experimentally determine, with confidence, the pressure mode of the combustion chamber to verify that it is indeed a Helmholtz mode, as assumed in the pressure formulations of MRMF (section 3.4).

The approach we took was two point simultaneous pressure measurements. Experimental data was compared with the characteristics of several potential candidates of pressure modes. And finally we will see whether our experimental data support our model assumption.

4.4.1 Experimental Setup

For the multipoint pressure measurements the air flow rate was set to 282 g/min, which corresponds to case B flame in the work of Weigand et al. [7]. The fuel flow rate was set to 38 g/min, resulting in an equivalence ratio of 1.2.

To perform multi-point pressure measurements of the combustion chamber, one of the glass walls of the combustion chamber was replaced with a 9.5mm thick steel plate. Six pressure taps were drilled into the wall so that pressure transducers could be mounted. Figure 4.1 shows the location of these pressure ports in the combustion chamber (point "A" through "F"). The locations of these points on the combustion chamber wall are shown in table 4.2. Here the symmetric axis of the burner is taken as $x = 0$ and the burner surface is taken as $y = 0$.

An additional pressure port was drilled into the plenum wall and labeled point "P", also shown in figure 4.1. Two PCB piezoelectric pressure transducers were used to make the measurements. Measured signals were passed on to an oscilloscope (LeCroy

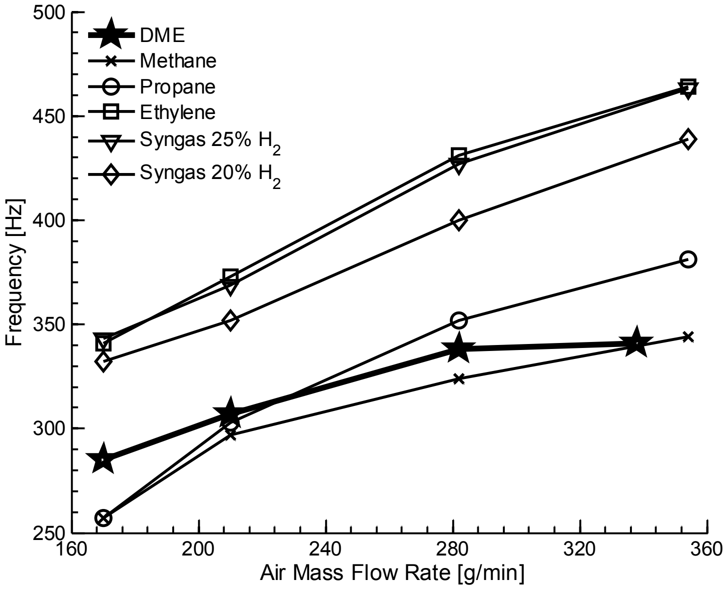

Figure 4.4: Frequency response to variations of air flow rates for various fuels in Allison et al.'s work [10].

Waverunner 6100A) for digital recording. The sampling rate of the oscilloscope was set to 25,000 samples per second and 5 seconds of data were recorded during each run. To eliminate hardware errors, one pressure transducers was fixed at point "B" while the other transducer rotated its location on all other pressure ports. Further calibration was provided by switching the two pressure transducers while measuring the phase differences between point "B" and "C". Pressure traces were recorded at a fixed burner surface temperature of 322 K (120 °F).

Table 4.2: Pressure measurement point locations*.

Point	A	B	C	D	E	F
x [mm]	0	-19	19	0	-19	19
y [mm]	19	38	38	57	76	76

* x = 0 at burner symmetric axis and y = 0 at burner surface.

4.4.2 Results

In the present study, it is found that pressure signals returned from two pressure ports always fluctuate at the same frequency, with a very sharp peak in the frequency spectrum (as shown in figure 4.5b). At the current operating condition, the instability frequency was determined to be 330 ± 2 Hz.

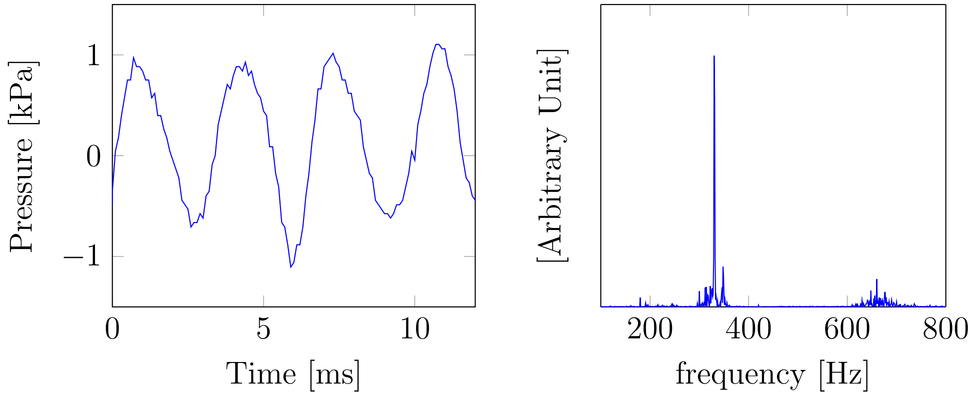

(a) Temporal pressure trace (b) Pressure Power Spectral Density

Figure 4.5: Typical pressure measurement result in combustion chamber

Relative phase differences between each measurement point and point "B" were calculated by Fourier transformation and shown in table 4.3. It shows that almost all the pressure ports inside the combustion chamber were in phase with each other. And the pressure inside the plenum was lagging by 0.44 ms. Similar behaviors have also been observed by Steinberg et al. [8].

Table 4.3: Relative phase between each measurement point and point B, based on $\omega = 330\text{Hz}$

	P	A	C	D	E	F
Phase difference w.r.t. B $(\psi_B - \psi_*)$	50°±5°	-10°±5°	0°±5°	0°±5°	0°±5°	0°±5°

The correlation factors between each point and point "B" are shown in figure 4.6. As mentioned above, the frequency spectrum of pressure measurements shows a very sharp peak at the instability frequency. This indicates that the temporal trace of pressure is close to a harmonic wave. For two of such waves, the correlation factor is given by $\cos(\Delta\psi)$, where $\Delta\psi$ is the relative phase difference between the two waves. In our case, since the phase differences between "B" and all other points in the combustion chamber are close to zero, we would expect a near unity correlation factor. What figure 4.6 tells us instead, is that there are still irregularities and noises within the time window during which we took the data. This resulted in a correlation factor that is lower than unity (about 0.8). Figure 4.6 nonetheless shows again that pressure inside the combustion chamber is strongly correlated across the volume, and the correlation with plenum is relatively weak.

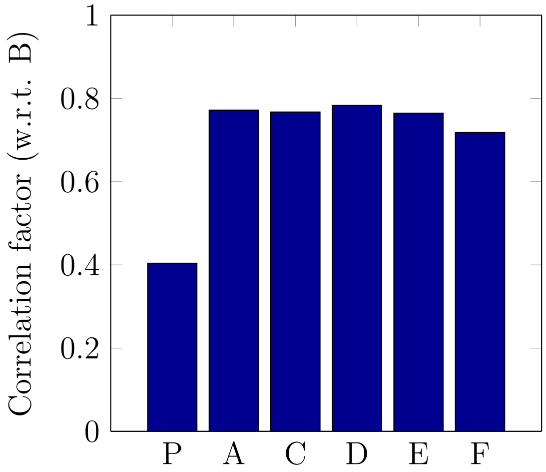

Figure 4.6: Correlation factors between each measurement point and point B

Pressure oscillation amplitudes at each point inside the combustion chamber are plotted in figure 4.7.We see that even though the pressure amplitudes decrease slightly as the distance from the burner surface increases, the change is less than 10%.

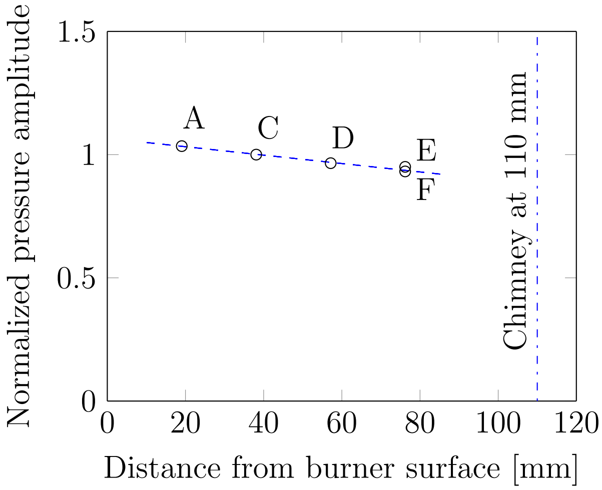

Figure 4.7: Normalized pressure amplitude in combustion chamber w.r.t. point B

4.4.3 Discussion

By far the most widely accepted mode of instability in this combustor is of Helmholtz type. However standing waves have been observed previously in combustion systems with large aspect ratios [66]. And it was shown that there are inner and outer recirculation zones generated by the injector in the combustion chamber of the GTMC [7]. These recirculation zones are prone to vortex shedding, which can also generate instabilities. Each of these modes has its own characteristics, which are summarized in table 4.4.

Table 4.4: Possible pressure modes in the combustion chamber and their characteristics

Mode	Key parameter	Characteristics
Helmholtz	Phase differences	Pressure in phase across the volume
Standing wave	Pressure amplitude	Pressure amplitude varies from max to 0
Vortex shedding	Strouhal number (St)	Instability frequency controlled by St

If vortex shedding caused instability inside the chamber, then its frequency would be determined by the Strouhal number:

$$\mathrm{St} = \frac{2\pi f \cdot L}{u} \ , \tag{4.1}$$

where f, L, and u are characteristic frequency, length, and velocity respectively. If we choose L to be 8.5 cm (burner surface edge length), u to be 10 m/s (average axial velocity [7]), and St to be 0.2 [67], we can estimate the vortex shedding frequency (f_{vtx}) to be:

$$f_{\text{vtx}} = \frac{\mathrm{St} \cdot u}{2\pi L} \approx 4\,\mathrm{Hz} \ . \tag{4.2}$$

The result is two orders of magnitude smaller than what we observed in the experiment. Even though this is a very rough estimate, the discrepancy can not be explained by merely the error of estimation. This leads us to the conclusion that the observed instability at 330 Hz is not caused by vortex shedding.

If a longitudinal standing wave is present in the combustion chamber, we would see the pressure oscillation amplitudes fluctuate from maximum to zero at least once across the combustion chamber height. If the standing wave is a quarter wave, then near the chamber exit (chimney) the pressure oscillation should be close to zero, and the acoustic frequency f_{std} should be:

$$f_{\text{std}} = \frac{c}{4\, l_2} \approx 2\,\mathrm{kHz} \ . \tag{4.3}$$

This frequency is again far off our measured instability frequency of 330 Hz. The results shown in figure 4.7 also contradict the quarter wave theory because pressure amplitudes stay fairly constant across the height of the burner instead of showing a sinusoidal pattern.

Hence the presence of a standing wave in the combustion chamber is also very unlikely. On the other hand, this figure does show that the presence of the chimney with large diameter has some effects on the pressure oscillation amplitudes. The damping effect is more evident as we get closer to the chimney.

Lastly, both the small relative phase angles shown in table 4.3 and the large correlation factor inside the combustion chamber shown in figure 4.6 indicate that the pressure inside the chamber are mostly in phase with each other. As mentioned above, their amplitude are also very close. All of these evidences are in line with the Helmholtz resonator behaviors.

Hence we reach the conclusion that the dominant instability mode of the combustion chamber is indeed a Helmholtz mode, which validated our model assumption for MRMF pressure module in section 3.4. However, experimental data also shows that the instability mechanism deviates from a perfect Helmholtz mode, caused by flow features, geometry constraints, as well as heat release and damping effects.

4.5 Comparison of MRMF Predictions to Experimental Data

In the previous section we have assessed the validity of one of our key assumptions for MRMF, which is that the system is dominated by a Helmholtz-type oscillation. In this section, we will explore the accuracy of our model predictions through comparisons with experimental data in section 4.3 and section 4.4

4.5.1 Parameters of MRMF in present study

Before we can use the MRMF, we still need to provide several input parameters. The geometry and flow parameters of the GTMC that we used are provided in table 4.5.

In addition to these geometry and flow parameters, we also need to calculate the Helmholtz resonance frequencies of plenum and combustion chamber. Both frequencies can be calculated from Eq.(3.25):

$$\omega_0 = \sqrt{\frac{C_\mathrm{u}^2 S_1}{V_0 l_1}} = 2129 \text{ rad/s} \approx 339 \text{ Hz} ,$$

$$\omega_2 = \sqrt{\frac{C_\mathrm{u}^2 S_1}{V_2 l_1} + \frac{C_\mathrm{b}^2 S_3}{V_2 l_3}} = 5048 \text{ rad/s} \approx 803 \text{ Hz} .$$

The lower heating value of DME is chosen to be $\Delta h_\mathrm{g}^\circ = 27.6$ MJ/kg [68]. The other parameter left to be determined is the convection time scale. From previous studies

Table 4.5: Model parameters used in this calculation

Component Subscript	Plenum 0	Injector 1	Chamber 2	Chimney 3
Length (l) [cm]	6.5	3.6	11.0	5.0
Diameter (D) [cm]	7.90	2.37*	8.50†	4.00
Cross-sectional area (S) [cm^2]	49.0	4.4	72.3	12.6
Volume (V) [cm^3]	319	16	795	63
Temperature (T) [K]	294	294	2000	2000
Ratio of heat capacities (γ)	1.4	1.4	1.3	1.3
Speed of sound (c) [m/s]	344	344	864	864

* D_1 is calculated as the equivalent diameter combining both the inner and outer swirler.

† The combustion chamber has a square cross section and D_2 is the length of its edge.

we estimated that flame lift-off height is 5 mm and the horizontal displacement is about 10 mm. The injector exit velocity is estimated from reference [7] to be about 12 m/s. This results in a convection time scale $\tau_c \approx 1$ ms.

4.5.2 Effect of combustion chamber damping (ζ_2)

In the previous section we have provided all parameters needed to solve Eq. (3.47), except one. This is the damping ratio (ζ_2) in Eq.(3.47b). Its counter-part, the damping ratio ζ_0 in Eq.(3.47a), was estimated to contain only the acoustic radiation loss in Eq.(3.26) in section 3.4.3. This is a reasonable assumption for plenum, which was constructed with solid steel all around and only has minimal acoustic loss.

However, this can not be assumed for the combustion chamber. The combustion chamber has a large amount of thermal and acoustic dissipation generated by the turbulent flame inside. Moreover, experimentally it has been found that the configuration of the walls affects the resulting frequency. For example, in the study of Allison et al. [10] (figure 3), the pressure measurement was done with three steel walls and one glass wall, and at $\phi = 1.2$ the frequency was about 360 Hz. In the pressure measurements presented in section 4.4 the configuration consisted of three glass walls and one steel wall, and the resultant frequency was around 330 Hz.

This means that it would not be a simple matter to estimate the value of ζ_2. Our estimation of ζ_0 is about 5×10^{-3}, the value of ζ_2 should be larger, but we are not sure about the range of estimation. So we solved Eq. (3.47) for the mathematical limit of ζ_2 from 0 to 1. The results are shown in figure 4.8a.

Here we can see that from a very small value of ζ_2, the instability frequency originally increases fairly monotonic until ζ_2 goes to about 0.2 and start to rise sharply.

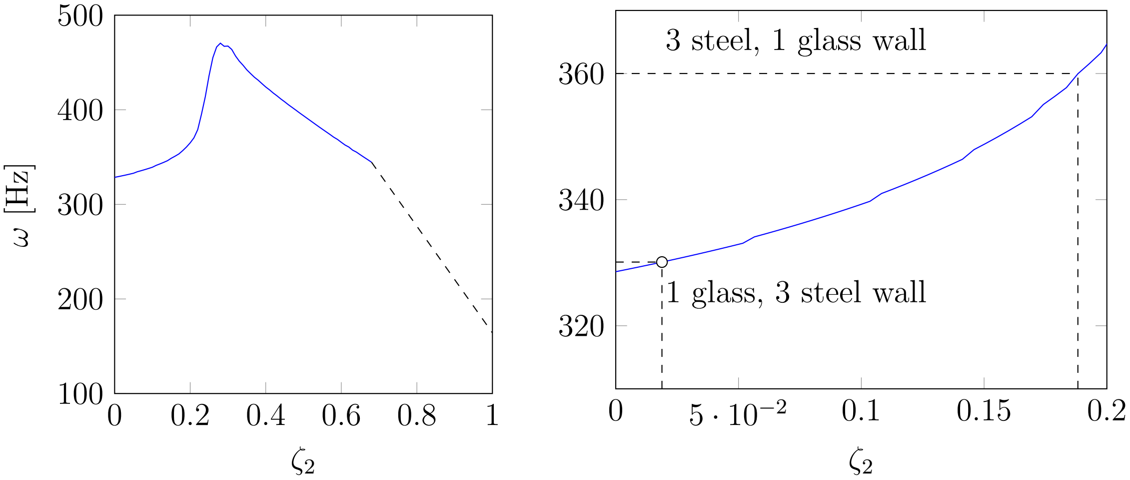

(a) Solution for ζ_2 from 0 to 1. Unstable solutions are shown in dashed line.

(b) Zoomed in to the range of $\zeta_2 \leq 0.2$. Black circle indicates the current estimated ζ_2 value of 0.02.

Figure 4.8: Dependence of predicted instability frequency ω over damping ratio ζ_2.

Afterwards it steadily decreases to about $\zeta_2 = 0.7$. Beyond this point the solution is very unstable and is indicated with dashed line. At the critically damped case ($\zeta_2 = 1$) the frequency is in the sub-200 Hz range. From this figure it is fair to assume that the value for ζ_2 should be in the initial range, where the relation is still quasi-linear. We can also see that all observed frequencies ($330 \sim 360$ Hz) fall into our predicted range.

If we zoom into this linear region, as shown in figure 4.8b, we can use the two frequencies that we previously measured with different combustion chamber wall configurations and look up the corresponding ζ_2 values. We see that the corresponding values of ζ_2 is in the range of 0.02 to 0.2. This is about one order of magnitude larger than our estimated value of ζ_0. Firstly, this is plausible, because the aforementioned damping effect in the combustion chamber is much larger than that of plenum. In the meantime, the lower end of the range (0.02) is close to our estimation of ζ_0 (0.005), this indicates that our original estimation of ζ_0 was not far off. Secondly, we have to treat this looked-up value of ζ_2 with caution. The values looked up here are under the assumption that our reduced order model can precisely predict the instability frequency, which should not be expected to be true despite our best wishes. Hence there are inherent errors in this estimation process. Nonetheless, this is a useful aid for us and provids us with a base for estimation – ζ_2 is estimated to be 0.02 for the present study.

Furthermore, we can look at the predicted phase relations between combustion

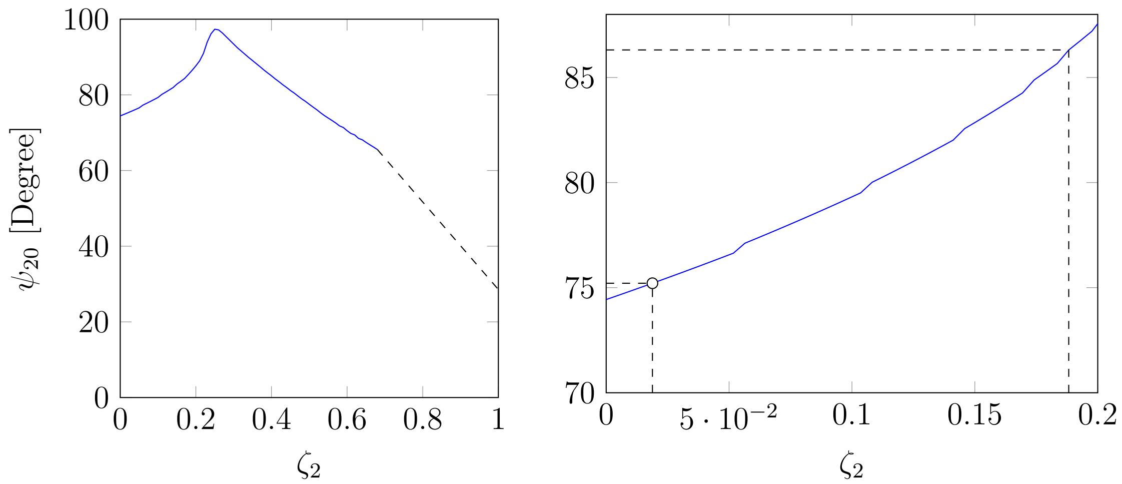

(a) Solution for ζ_2 from 0 to 1. Unstable solutions are shown in dashed line.

(b) Zoomed in to the range of $\zeta_2 \leq 0.2$. Black circle indicates the current estimated ζ_2 value of 0.02.

Figure 4.9: Dependence of predicted phase difference ψ_{20} over damping ratio ζ_2.

chamber and plenum, as shown in figure 4.9. Here the we follow the same sequence as in figure 4.8. In figure 4.9a we can see the dependence of ψ_{20} over ζ_2 follows a very similar trend to that of ω. Specifically in the zoomed in region of $\zeta_2 \leq 0.2$ shown in figure 4.9b, we can see that in the range of $\zeta_2 = 0.02 \sim 0.2$, the predicted phase angle is 75° to 85°. These values deviate from our measured value of $\psi_{20} = 50° \pm 5°$, but it is close to the values reported by Steinberg et al. ($60° \sim 80°$) [64, 8].

We can also compare the predicted phase difference with some of the studies of classical Helmholtz analysis. One of such study is done by Hersh and Walker [11]. They developed a model for Helmholtz resonators which also considers the complex flow patterns near the nozzle of a Helmholtz resonator. Their predictions of relative phase difference is shown in figure 4.10.

We can see that in the ideal Helmholtz theory, the relative phase angle should be 90° near the Helmholtz resonance frequency. Hersh & Walker's study gave a lower value at practical conditions. Consider that the system instability frequency is very close to the Helmholtz resonance frequency of plenum-injector (ω_0, 342 Hz), our observed instability is likely to be caused by or result in the resonance of plenum. In such case, our predicted value of ψ_{20} (75° to 85°) is actually very close to the predicted value of Helmholtz theory. In the meantime, our measured value is very close to the theory by Hersh & Walker.

As a conclusion, we can see that both the system instability frequency ω and phase difference predicted by our MRMF model are in agreement with the corre-

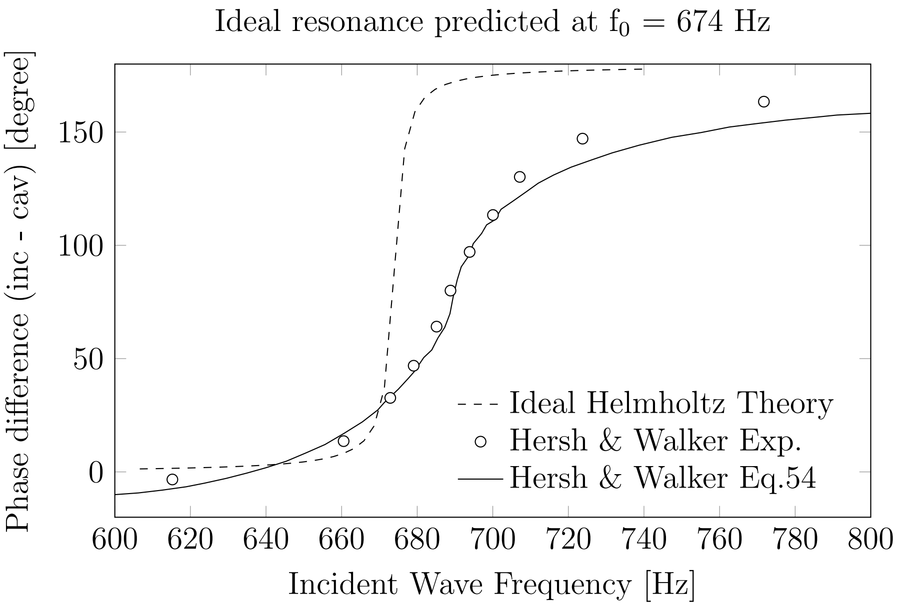

Figure 4.10: Comparison of relative phase angles across the neck between ideal Helmholtz theory and Hersh & Walker results [11]

sponding measured values and are comparable to the Helmholtz theories. This shows the capability of the present model to capture important physical processes in the system. Through comparison with experimental data, ζ_2 is estimated to be 0.02 in the following studies.

4.5.3 Effect of varying the geometric parameters

With all the parameters estimated at the reference point (DME flame, $\phi = 1.2$, $\dot{m}_\mathrm{a}$ = 282 g/min), we can start to explore the effect of changing geometric parameters of the GTMC in our model and compare the results with the experimental data provided by Allison et al. [9].

The first parameter we explore is the plenum volume V_0. The model is evaluated for a range of different plenum volumes as determined by the experimental data shown in figure 4.3. The normalized result is shown in figure 4.11.

In figure 4.11 it shows that our prediction follows the same trend as the experimental data. Specifically the instability frequency decreases as the volume of plenum increases. This is expected because from Helmholtz analysis we know that as plenum volume increases, the characteristic frequency will decrease. Since our combustion instability frequency is dependent on the Helmholtz frequency of the plenum, it should also decrease.

For reference, in figure 4.11 the prediction of an ideal Helmholtz resonance fre-

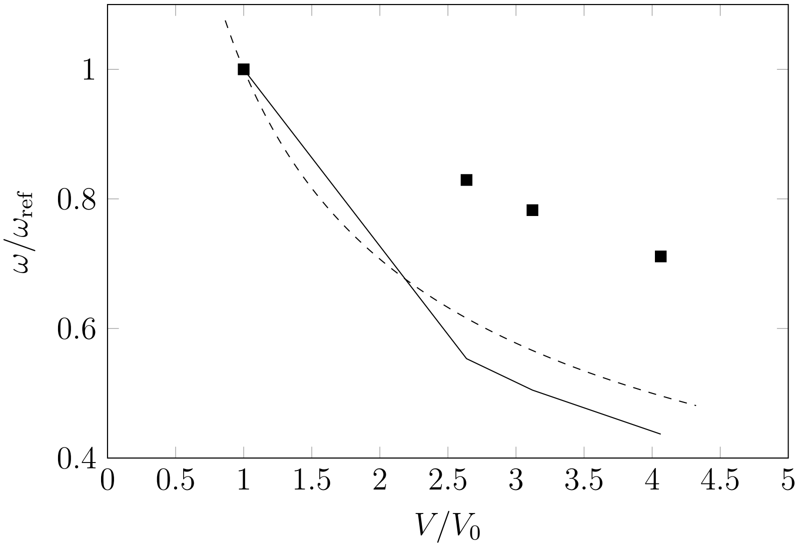

Figure 4.11: Effect of varying plenum volume V_0 on the instability frequency: solid squares are experimental data by Allison et al. [9], solid line is prediction made by MRMF, dashed line is predictions of classical Helmholtz theory.

quency for plenum is also plotted (the dashed line). We can see that our prediction is closer to the ideal Helmholtz resonator than experimental data. The remaining difference between our model prediction and the Helmholtz theory lies in the fact that the predicted instability is affected not only by the plenum, but also by the combustion chamber. Also, in most of the time the instability frequency is not at the resonance frequency of either chamber, hence its deviation from Helmholtz resonance frequency prediction of plenum is understandable.

The difference between our model prediction and experimental data lies at the slope of the curve. Our model as well as Helmholtz theory predicts that frequency decreases at a rate of $V_0^{-0.5}$ whereas in the experimental data the frequency decreases at a rate of $V_0^{-0.25}$. Sensitivity analysis has been conducted and we found that varying ζ_2 would not mitigate this discrepancy. We have also varied the value of τ_c from 1 ms to 2 ms. Even though the magnitude of the predicted frequency gets closer to the corresponding experimental value, the difference of slope is still evident. We suspect experimental uncertainty may play a part in this disagreement.

Next we examine the effect of changing the dimensions of the chimney over the instability frequency. Allison et al. [9] stated that the instability frequency has a dependence over the geometry of the chimney, as shown in figure 4.3 (b). In figure 4.12 the predicted results of MRMF are compared against Allison's data on a normalized base.

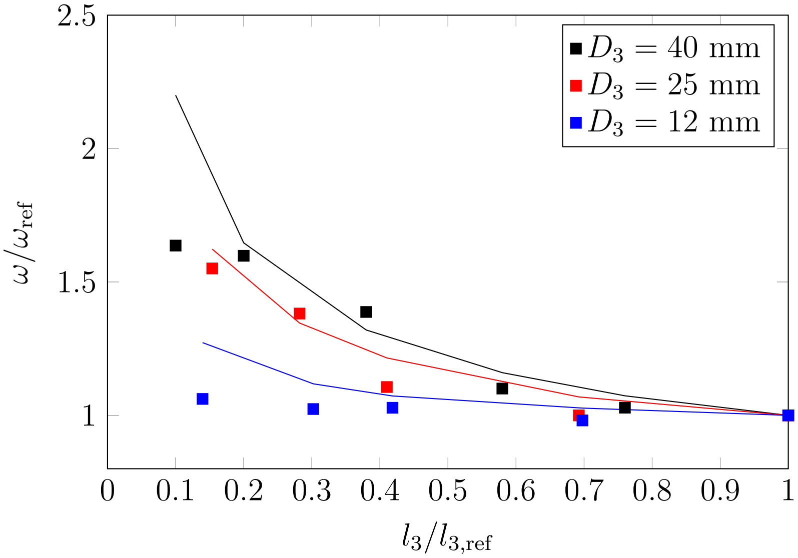

Figure 4.12: Effect of varying chimney length l_3 on the instability frequency at different chimney diameter (D_3): solid squares are experimental data by Allison et al. [9], solid line is prediction made by MRMF.

If the combustion instability frequency is purely attributed to the influence of the plenum, then the change in chimney would have no effect on the instability. From experimental data we can see that this is clearly not the case, and because our MRMF model considers the interaction between plenum and combustion chamber, the effect of the chimney is captured. We can see from figure 4.12 that our model predictions adequately captured the trend when chimney diameter and length are changed.

4.5.4 Effect of varying equivalence ratio

One of the focus of the previously reviewed work by Allison et al. [10] is to compare DME flames of different equivalence ratios in terms of their dynamic structure. As shown in table 4.1, the fuel-lean flame with $\phi = 0.75$ was considered to be "quiet" because of its very small pressure oscillation. The flame with $\phi = 1.0$ was considered as "weakly resonating" because of its intermittent pressure fluctuations, while the flame with $\phi = 1.2$, the same as the condition we operated in section 4.4 above, is considered as "resonating" because of its very large pressure fluctuations.

To predict the influence of equivalence ratio on combustion instability, we need to look back to the governing equations of the MRMF model in chapter III. In section 3.7 we summarized the heat release model for partially premixed flame with direct fuel injection (MRMF *Module Q2*) in Eq.(3.42):

$$\frac{d\dot{Q}'}{dt} = \begin{cases} 0 & \text{if } \max(\phi) < 1 \\ \text{intermittent} & \text{if } \min(\phi) < 1,\ \max(\phi) > 1 \\ \frac{\Delta h_{\mathrm{g}}^{\circ}}{AFR_{\mathrm{st}}} \cdot \frac{S_1}{l_1} \cdot (P_0' - P_2')|t - \tau_{\mathrm{c}} & \text{if } \min(\phi) > 1 \end{cases} \tag{3.42}$$

This equation states that when the mixture is very lean ($\max(\phi) < 1$), the heat release rate is constant, and its fluctuation is zero. Considering that the heat release rate fluctuation is the driving force for combustion chamber pressure fluctuation, which in turn drives plenum pressure fluctuations, $\dot{Q}' = 0$ means that Eq. (3.47b) will have a trivial solution of $P_*' = 0$. This in reality means that there will not be combustion instability present.

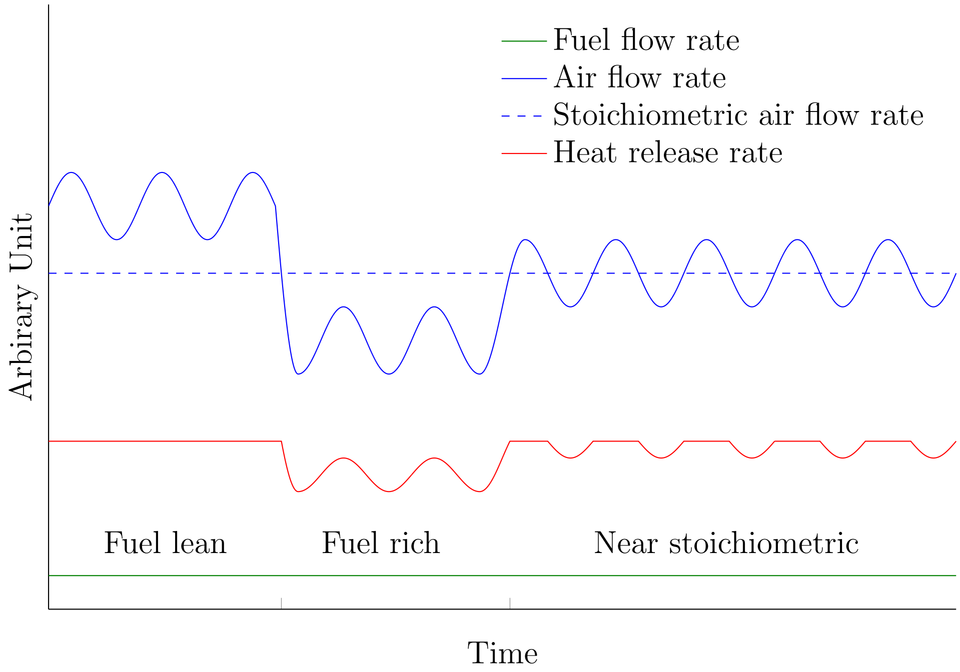

Figure 4.13: Prediction of Eq.(3.42) on the existence of combustion instability under different equivalence ratio values

By the same logic, Eq. (3.42) predicts that if the mixture is near stoichiometric, the flame will be unstable in the instances when it is fuel rich, while the flame stays stable in the instances when it is lean. Hence this will produce a "intermittently" unstable flame. Lastly, if the mixture is very rich in fuel, the flame will be continuously driven by the fluctuating heat release rate and become unstable. This difference is illustrated in figure 4.13.

Our model prediction describes precisely what we were observing in our experiment. In other words, from our model we propose the hypothesis that the flame instability in GTMC is controlled by the deficient stream (fuel or air) flow rate. At the same time, we have to fully understand that such hypothesis is based on the assumption that: *i*) the chemistry involved is a one-step reaction, there is no partial fuel decomposition; *ii*) all chemical reactions are much faster compared to the flow residence time (Damköhler number is infinite); *iii*) heat release is not affected by the mean flow rate or turbulence levels, for example blow-out is not considered; and *iv*) the incoming fuel flow rate is constant and there is no fuel-trapping near the injection nozzle due to complex flow interactions. Some of these assumptions are very likely violated in the GTMC, but our proposed model nonetheless provides a theoretical base to understand fundamental physical processes in this burner.

4.5.5 Effect of varying mass flow rate

If we look into the governing equations of our model (Eq.(3.47b)), there is no explicit dependence on the mass flow rates. However mass flow rates play a role implicitly in our system.

The first effect of mass flow rate is on the damping ratio of combustion chamber and plenum. In the literature [55, 69] we can see that damping ratio will increase when mass flow rates are increased, meaning that more damping effect will be present when the gas mixture has to flow through narrow passages faster. In figure 4.8 we already showed that the predicted instability frequency will increase with increased damping. This is in agreement with the trend observed by Allison et al. in figure 4.4.

Moreover, as the mass flow rate increases, the convection time τ_{c} will be altered. However, the relationship between mass flow rate and convection time delay is more complicated. From Eq. (3.41) we can see that in our model the convection time is assumed to be the ratio of mean lift-off height $\overline{H}_{\mathrm{fl}}$ and mean axial velocity $\overline{U}_2$. On one hand, with larger mass flow rate comes larger mean velocity. But on the other hand, the larger velocity will likely push the flame stabilization point further downstream, thus increaseing the flame lift-off height.

Without determining the exact dependence of τ_{c}, we in turn look at the effect of τ_{c} on the instability frequency, as shown in figure 4.14. The pattern shown in figure 4.14 is periodic, hence here only one period is shown. We can see that with modest time delay (within ± 10% of estimated value) its effect of altering the instability frequency is still limited.

However, we do encounter unstable solutions for our governing equations in the region near $\tau_{\mathrm{c}} \cdot \omega_{\mathrm{ref}} = \pi$. When the heat release rate is 180° away from the velocity

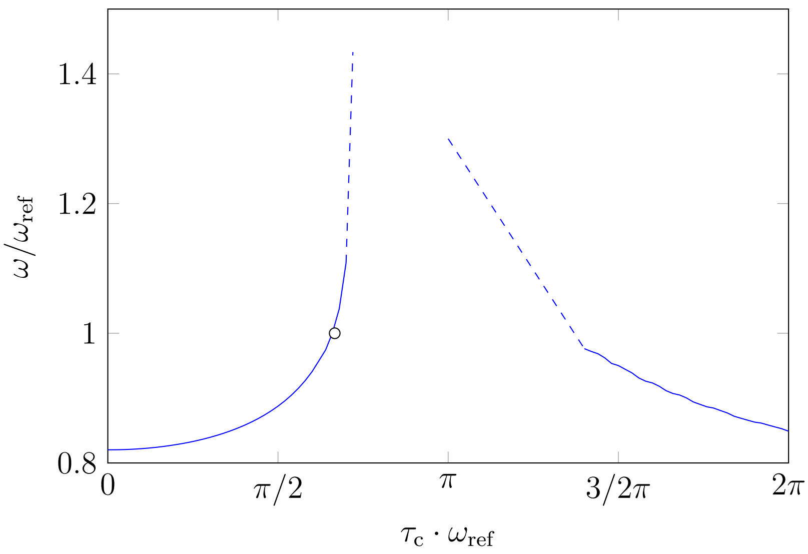

Figure 4.14: Effect of convection time delay τ_{c} on system instability frequency. The pattern is periodic, here it is shown in only one period at reference frequency ω_{ref}. Black circle indicates the current estimated τ_{c} value of 1 ms. Unstable solutions are shown by the dashed lines.

fluctuates in phase, its derivative $d\dot{Q}'/dt$ will be 90° away from velocity fluctuations at injector exit (U_2'). U_2' is related to the pressure fluctuations by Eq.(3.39). This means that when heat release fluctuation is 90° from the difference of fluctuating pressure our system of equations is unstable.

4.6 Summary and Motivations for Further LASER Studies

In this chapter we first presented the related information about the DLR GTMC. We then surveyed previous studies conducted on GTMC to characterize its thermoacoustic instabilities. Through this literature review we noticed the need to deterministically assess the mode of the instability in the combustor. This motivated us, in the following section, to present our experimental study on determining the instability mode inside the GTMC. The pressures at different locations inside the combustor are found to be in phase (table 4.3) and pressure amplitude is nearly constant within the combustor (figure 4.7), both of which are indicative of a bulk mode. The result of this experimental study confirmed our earlier assumptions for MRMF, which stated that the system is dominated by a Helmholtz-type instability. We then used this MRMF model to make a series of predictions of the combustion instability of GTMC. The results of our predictions in most part agree well with the experimental data obtained by present study as well as previous studies by Steinberg and Allison et al. That is, the measured frequency of our combustion instability (330 Hz) agrees with the model predictions using Eq.(3.47). The phase difference measured between plenum and combustor ($50 \sim 60^\circ$) is consistent with the prediction made by MRMF if a reasonable damping ratio (ζ_2) of 0.02 is assumed for the combustion chamber. The proposed model is also found to be capable of explaining a series of experimental observations where the instability frequency changed with burner geometry and fueling conditions.

In the meantime, to make these predictions with our model, we have to make several assumptions to simplify the physical processes. For example, we hypothesize that the existence of combustion instability depends on the equivalence ratio, under the assumption that the flame dynamics is controlled by the flow rate of the deficient stream (either air or fuel). Also, we saw in section 4.5.5 that τ_c is affecting directly the stability of the solution of our system. This effect is due partly to our simple estimation scheme for τ_c in Eq.(3.41).

The validity of these important assumptions and hypothesis of our model can not be assessed using the pressure measurements that we presented in this chapter. Hence a temporally and spatially resolving method for determining the relationship between heat release, velocity, and pressure fluctuations has to be used in experiment to complete the assessment. This motivates us to setup the kilo-Hertz simultaneous PIV-PLIF-pressure measurement, which will be discussed in detail in the next chapter.

CHAPTER V

Assessment of MRMF on GTMC – Part 2: interactions between heat release, velocity, and pressure

5.1 Introduction

In chapter IV we presented comparisons between predictions made by the proposed Modular Reduced-order Model Framework (MRMF) and pressure measurements. Considering the degree of simplification, we had a good agreement between our model and experimental data. However, we also realized that for a complex burner like the GTMC, without knowing the temporal and spatial details it will be impossible for us to analyze the discrepancies between our model predictions and experimental results.

Hence in this chapter we will use a range of laser diagnostic tools to assess the model assumptions and predictions. In chapter III we conceptually separate the combustion instability into three interactive components: pressure fluctuation, heat release oscillation, and velocity oscillation. In this chapter, we will experimentally characterize all three of these quantities. Pressure measurement is achieved through a microphone installed on the plenum, heat release fluctuation is related through CH_2O PLIF signal, and velocity is directly measured from PIV.

In the next section we will first discuss the experimental setup, then we will go over the data processing procedures. Afterwards the results from current measurements are presented and lastly conclusions related to model assumptions are discussed.

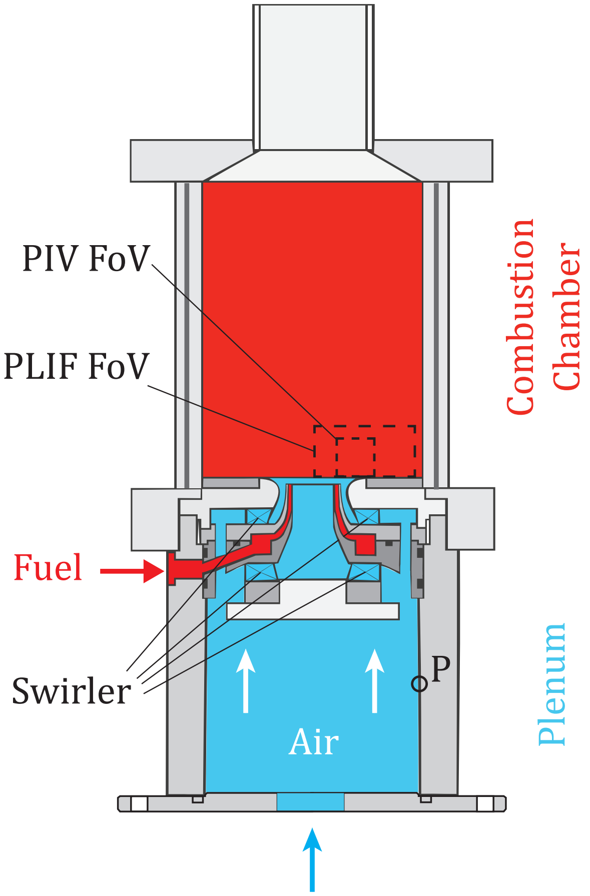

Figure 5.1: Schematics of the GTMC, with the FoV of both PLIF and PIV system

5.2 Experimental Setup

To accomplish our said goals, a system of high speed simultaneous laser diagnostics is constructed. In this section, we will discuss the setup of this system.

5.2.1 Diagnostic system overview

The center piece of this laser diagnostic system is the GTMC burner that has been introduced in chapter III and in detail in chapter IV. Without mentioning the detailed parameters again, we will present the burner here again in figure 5.1, with the Field of View (FoV) of both the PIV and PLIF system overlaid.

The two major sub-systems of our experimental setup, that of PIV and PLIF are laid our around the burner. Each system contains a laser light source, a set of optics for beam forming, and light detection system for collecting the optical signal.

Other than these two major sub-systems, we also have a sub-system for simultaneous pressure measurements and a series of timing/control units that coordinate the components in each system to achieve desired temporal precision. In figure 5.2 the schematics of all major components of the experiment are shown.

In the present study, the high speed system is operated at a data acquisition rate of 4 kHz. We first introduce the two laser imaging systems: the Digital Delay Generator (DG) #2 (Stanford Research Systems DG645) gives out a time-base signal (through F-sync) at 8 kHz to the PIV camera (Phantom v9.1), because PIV measurements require two frames of data to create one frame of velocity vectors. In the meantime, through internal frequency division, DG #2 also gives out a 4 kHz time-base signal (through F-sync) to the PLIF camera (Phantom v711) and (through EXT-TRIG) to DG #1 (Stanford Research Systems DG645). Hence DG #1 becomes another source of 4 kHz time-base signal, externally triggered by DG #2. The time delay for the triggering process between the two DGs is determined by measuring the output signal of both DG simultaneously on a oscilloscope, and this time delay is compensated by setting a small delay to all other channels of DG #2.

DG #1 is responsible for providing a 4 kHz time base to all other components of the system that needs it. One of them is the PIV laser (Continuum Hawk-Duo, 532 nm/120 W). Even though this PIV laser outputs laser pulses at 8 kHz, internally it consists of two separate laser cavities who requires two separate channels of 4 kHz time signal. DG #1 also sends 4 kHz time base signals to PLIF laser (Continuum Hawk-HP, 355 nm/40 W) and the intensifier for PLIF camera (LaVision HS-IRO). With this setup, the two laser-imaging sub-systems are coordinated temporally so that the PIV and PLIF systems are measuring at the same instance. The detailed information regarding the timing procedure will be discussed in section 5.2.3.

Other than these two major sub-systems, we have another sub-system for pressure measurements. This sub-system consists of two piezoelectric microphones (PCB 378C10, factory custom calibrated) and their signal conditioner (PCB 482C05). One of the microphones is mounted on the plenum of GTMC while the other one is mounted in open air facing the burner at a distance of about 10 cm. The signal conditioner provides power supply to the microphones and returns their signal to an oscilloscope (LeCroy Waverunner 6100A).

The pressure measurements are continuous at 1 MHz and once the laser is powered up, the imaging system is also continuously acquiring data at 4 kHz. Unfortunately the on board storage space on the oscilloscope and the cameras are limited, so only one second of data can be recorded every run. This creats a need to synchronize the laser imaging system (which is already internally synchronized between PIV and PLIF by the two DGs) with the pressure measurement system. Hence one channel of 8 kHz time base signal that goes to the PIV camera from DG #2 is branched off and connected to the oscilloscope as well. In this way the laser imaging time base can be correlated to the pressure measurement time base.

The only remaining piece is a triggering source that can start data acquisition simultaneously between the two cameras and the oscilloscope. This is achieved with the addition of a third DG (Stanford Research System DG 535). Once manually activated, DG #3 gives out a triggering pulse to both the cameras (through TRIG) and the oscilloscope every 5 seconds. DG #3 also gives a square wave signal to the intensifier controller in the PLIF system to enable ICCD Relay Optics (Optical Intensifier) (IRO) for only 1.2 seconds. We installed this function (following Prof. Gamba's advice) so that the intensifier (IRO) is only firing within the data acquisition window (with a small amount of extra time to account for potential timing errors). Otherwise the IRO will be continuously firing at 4 kHz (triggered by DG #1), which will decrease its useful life. The 5 seconds interval of DG #3 is selected so that it will leave fairly small amount of time between we manually activate it and it actually gives out the trigger signal, while leaving us enough time to switch it off before it starts to enable the IRO again in the next cycle.

The sequence of actions in one run is as follows:

1. The lasers are powered up to warm up, DG #1 and DG #2 are started and the laser imaging system starts to acquire data, in the meantime, pressure data from two microphones start to flow into oscilloscope;

2. Flame is ignited, at the right moment, the lab operator activates DG #3, a trigger signal is sent to both cameras and the oscilloscope, three of them start to record data, at the same time a enabling signal is sent to IRO so that IRO starts to work, amplifying the signal that goes into PLIF signal;

3. After about 1.2 seconds, the storage in PLIF camera will be full, at the same time the enabling signal from DG #3 to IRO ends, IRO stops firing;

4. DG #3 is manually deactivated to prevent it from enabling IRO again;

5. 3 seconds after the initial trigger, the storage in both PIV camera and oscilloscope will be full, the recording process is finished;

6. Flame is extinguished, and data in the cameras are transmitted back to control computers.

5.2.2 Optical properties of the system

As shown in figure 5.2, the PIV system operates a 532 nm beam generated from the high speed diode-pumped Nd:YAG laser while the PLIF system operates a 355 nm beam from a similar laser. After being emitted from both lasers, the laser beams first separately enter two periscopes to be raised from table level to the height of the burner surface. Then each of them passes through a cylindrical lens (CVI-SCX-50.8-254.3-UV-355-532) that contract them horizontally and forms a thin sheet with the waists fall at the centerline of the burner. It has to be noted that because of the natural divergence of the beam is large, we do not need a separate spherical lens to expand the beam. Before reaching the burner, the 532 nm beam is reflected 90° and merged with the 355 nm beam at a dichroic mirror (CVI BSR-35-2025) that transmits 532 nm light and reflects 355 nm light. When the laser beams reach the burner surfaces, the beam height is 20 mm.

Two sets of filters are placed in front of the cameras. For the PIV camera, the filter is a narrow-band pass 532 nm filter (Andover 532FS02-50) that only lets the PIV signal (at 532 nm) passes through. For the PLIF camera, the filter set consist of a CG-385 filter that blocks light below 380 nm and another BG-3 filter that blocks light in the range of 480 nm to 680 nm. From figure 1.4 we know that the majority of the CH_2O PLIF signal is in the range of 400 nm to 500 nm. So such a combination of filters for PLIF camera can block the incident laser light at 355 nm and black body radiation at high wavelengths while retaining the PLIF signal.

The lens on both cameras are Nikkor 105mm f2.8 macro lens. The macro capability of these lenses enabled us to move the cameras to a minimum distance of 30 cm from the focusing plane. During the experiment, the aperture of the lens is opened to f2.8 to ensure maximum signal level. The field of view (shown in figure 5.1 for both systems) of the PIV system is 15 mm × 15 mm while that of the PLIF system is 20 mm × 40 mm. The PIV image is represented by 384× 384 pixels, yielding a scale of 39 μm per pixel. The PLIF image is represented by 508 ×1016 pixels (cropped from a 720 × 1280 raw image), yielding a scale of 39 μm per pixel as well. Both systems are tested with a standard 1951 USAF target for resolving power. The PIV camera returns a revolving power of 9 lpmm (line pairs per millimeter), which means that it can resolve a line no thinner than 56 μm. And the PLIF camera + IRO combination has a resolving power of 7 lpmm (70 μm resolution). The resolving power of the PLIF camera (Phantom v711) itself is impaired after its coupling with the intensifier (IRO). This coupling between camera and IRO has been manually adjusted to obtain the best resolving power possible.

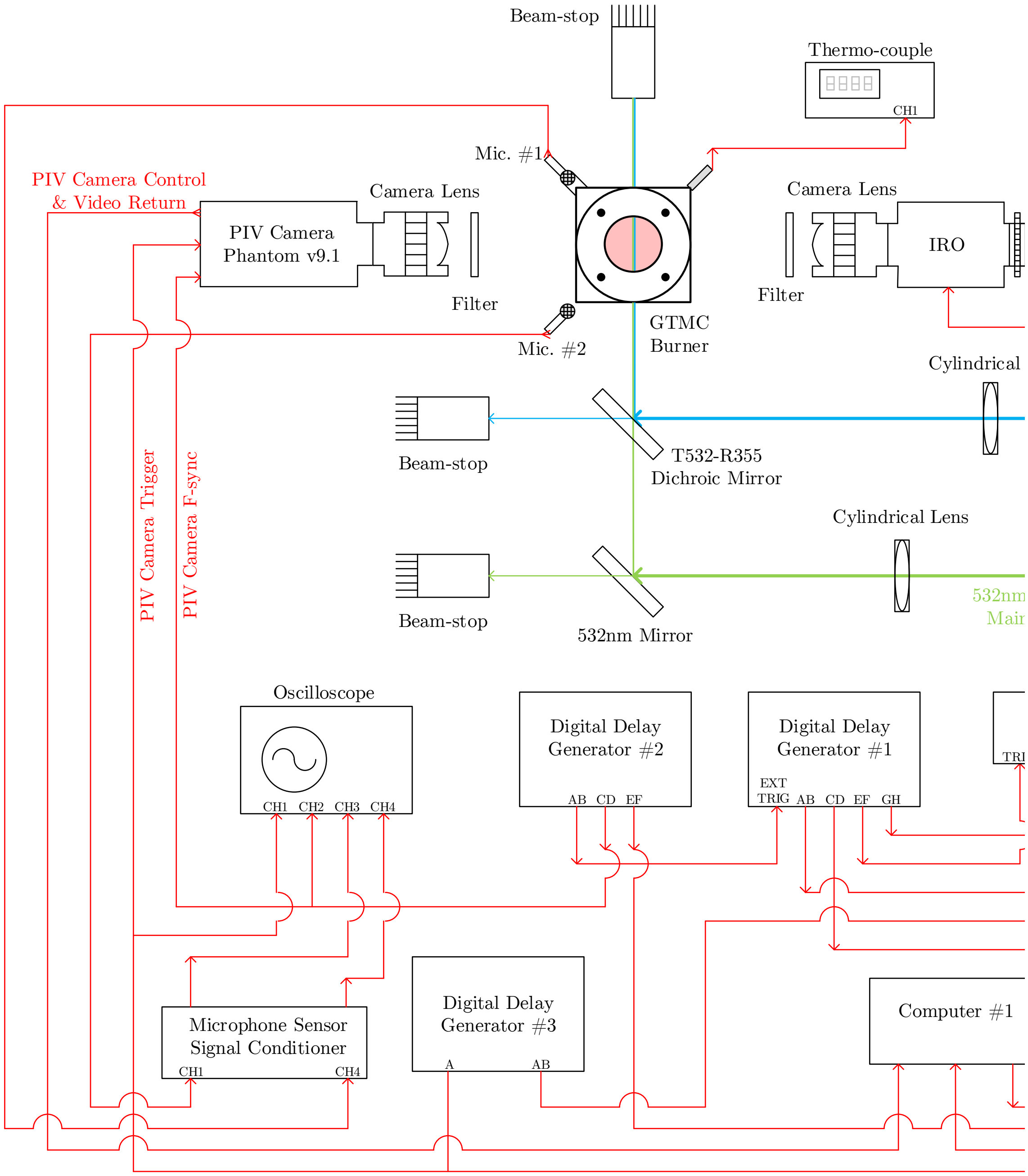

Figure 5.2: High speed simultaneous measurements system layout (Part 1/2), part of the figure is duplicated in the overlapping region between the two parts.

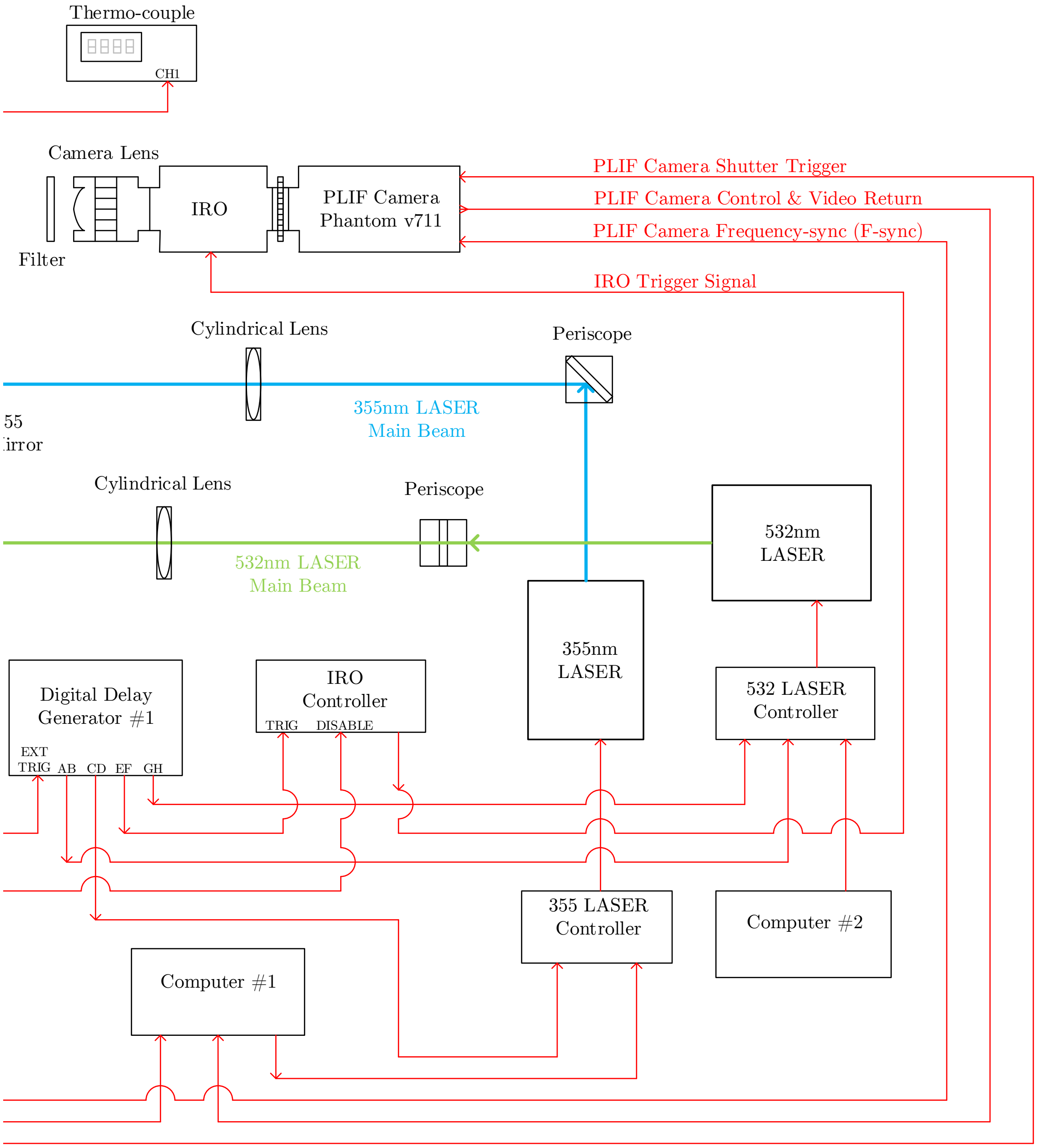

Figure 5.2: High speed simultaneous measurements system layout (Part 2/2), part of the figure is duplicated in the overlapping region between the two parts.

5.2.3 Calibration of timing scheme for laser imaging systems

The simultaneous system consist of components and equipment that work over a wide range of time scales. At the largest scale, the time for recording one run is about 1 second; at the smallest scale, the laser pulse lasts on average about 100 ns, with a rise time of about 10 ns. These two scales are different by a factor of $10^7 \sim 10^8$. Hence detailed timing setting in the DG is required so that multiple components are properly working at the same time in the very short time of data acquisition. This requires a lot of manual calibration as well, because in the $\mathcal{O}(100 \text{ ns})$ range (IRO gate opens 200 ns per pulse) that we are working with, even the speed of the light has to be considered. For example, the time for electrical signal to travel through 10 feet of cable is about 15 ns, which is about 10 to 20 % of the duration of one pulse of our signal. Considering time delay at each connection and within a range of electronic components, the system has to be calibrated such that cables are not to be replaced once installed. Even in such conditions, after a period of time, the timing scheme has to be checked again for potential shifting.

Figure 5.3 shows the timing scheme that was used to acquire the data that will be discussed in this work. This diagram shows the sequence of events happening in each cycle of data acquisition, taking the instant when one pulse of the 4 kHz time base signal arrives at both cameras as $t = 0$. The parameters shown are obtained through a series of calibration and tests, sometimes separately before the system was assembled.

For example, the time between a time base signal is sent out by DG and a laser shot actually arrives at the burner is determined to be around 4.4 μs (for both PIV laser and PLIF). This is obtained by placing a solid reflective object over the burner and a photo-diode facing this object. In the oscilloscope the time between the signal sent out by DG and the signal returned from the photo-diode is measured. This time delay has to be more precisely determined for PLIF system because the IRO gate time is very short. So based on the previous estimation, in another test run, we ignited the flame and adjusted the time window of IRO opening (which lasts 200 ns) back and forth around the predicted laser pulse arrival time. The time window of the PLIF signal arrival is determined by the time between the initial rise and the maximum saturation of PLIF signal level. After determining this time window, the timing is set such that the PLIF signal (about 100 ns long) falls in the middle of the IRO opening window, leaving 50 ns on each side to allow for potential small time drifting later.

Care has also been taken to ensure that no light from CH2O PLIF signal gets into the PIV camera (even though it would be small anyway because of the narrow pass

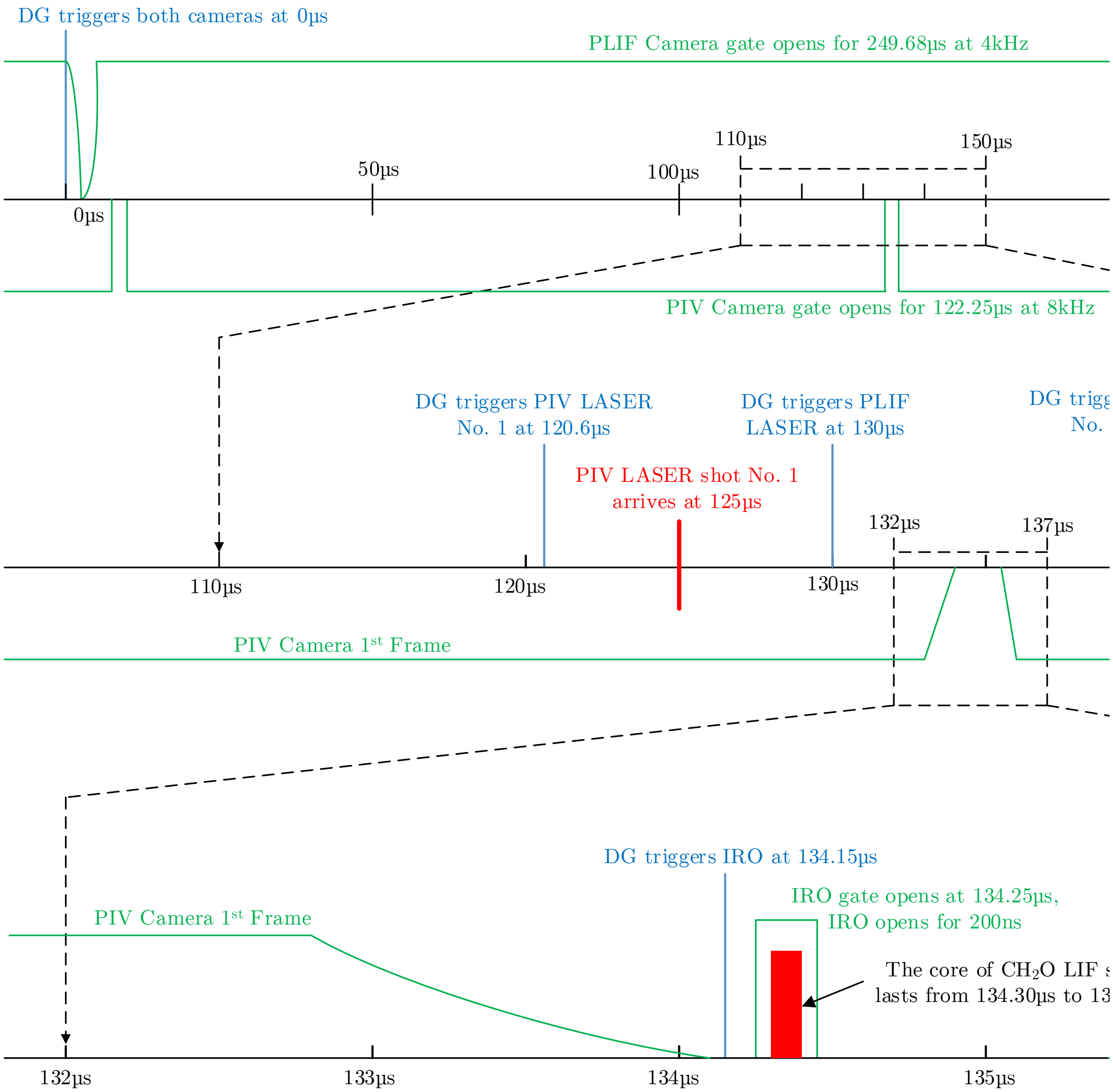

Figure 5.3: Timing diagram for PIV and PLIF system (Part 1/2), part of the figure is duplicated in the overlapping region between the two parts.

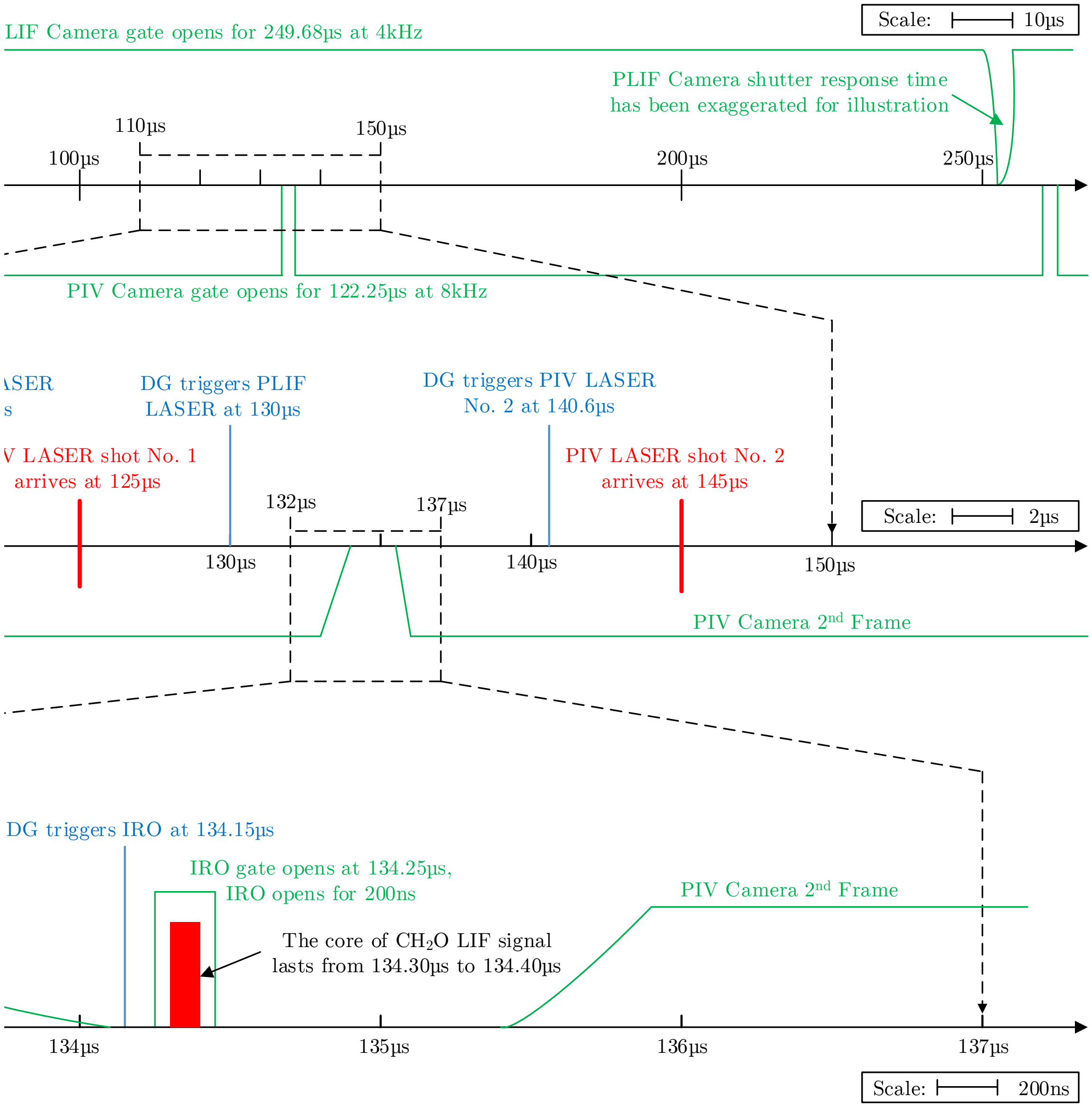

Figure 5.3: Timing diagram for PIV and PLIF system (Part 2/2), part of the figure is duplicated in the overlapping region between the two parts.

532 nm filter). This is achieved by keeping the two PIV laser pulses at a fixed Δt of 20 micro-seconds with the seeded air running, then shifting the PIV camera time base back and forth. The window between two camera shots are determined by the time between the instant when the first frame starts to lose signal and the instant when the second frame starts to pick up two shots of superimposed PIV images.

5.2.4 Details of the hydraulic system

The systems mentioned above are mostly for the diagnostic equipment, the experiment also has to be supported by a hydraulic system that supply fuel, air, and water to the GTMC and peripheral equipment. The schematics of the entire hydraulic system is illustrated in figure 5.4.

The air stream is supplied by the building low pressure air line, at an inlet pressure of 120 psi. The air stream passes through two filters to reduce the water and dust contents before going into the hydraulic control panel. There it is separated into two streams. One directly passes through two control valves, a pressure gauge, a choked orifice (size #86, $C_\mathrm{d} = 0.93$) and goes into the GTMC as the main air supply. Another air stream passes through a set of valves, a choked orifice (size #25, $C_\mathrm{d} = 0.87$), and enter the PIV seeder before merging with the main air line. The seeding particle in this study is a mixture of SiO_2 and Al_2O_3 with a mean diameter of 5 μm (3M Zeeospheres X-61).There is a pressure gauge before and one after the choked orifice in the seeding line. Hence the pressure drop can be monitored to ensure that the orifice stays choked in the experiment.

The fuel stream is supplied from a fuel cylinder. DME is in liquid phase in the cylinder, it evaporates immediately when pressure is released. The vapor pressure of DME at room temperature is about 60 psi, which is the exit pressure of the fuel bottle. The fuel stream passes through two control valves, a pressure gauge, a choked orifice (size #35, $C_\mathrm{d} = 0.89$) and goes into a fuel mixer. This mixer is a cylinder with honeycomb veins, used to slow down and damp out the unsteadiness of the fuel stream before entering GTMC. From the mixer, the fuel stream is branched out into three lines to feed into the three fuel ports of GTMC.

The flow rates of both air and fuel streams are determined by the upstream pressure of all choked orifices through a choked flow analysis. For the cases presented in this work, the pressure upstream of each orifice are summarized in table 5.1.

As shown in figure 5.4, there is a separate line of cooling water from the building circulation line coming into the main laser beam dump. This is because the combined power of two high speed lasers is 160 W (slightly higher in reality). At such power,

Table 5.1: Pressure upstream of choked orifices for the investigated cases

Case	$\dot{m}_{\mathrm{a}}$	ϕ	Fuel	Main air	Seeding air
R1	282 g/min	1.2	45 psi	64 psi	40 psi
L1	282 g/min	0.75	23 psi	64 psi	40 psi
S1	282 g/min	1.0	35 psi	64 psi	40 psi
R2	226 g/min	1.2	33 psi	47 psi	40 psi

water cooling to the beam dump is required.

5.2.5 Safety precautions

As the complexity of a system increases, the potential of having safety hazards also grows. Two of the major safety concerns in our system are the high pressure (highly) combustable fuels and high energy (invisible) laser beams. A lot of measures have been taken to ensure the safety of the lab operator as well as other occupants of the same building.

To avoid fire and potential explosion of the high pressure fuel, a set of actions have been taken to separate the fuel from air before it enters the combustion chamber. Firstly, the hydraulic connections are pressurized with nitrogen to 50 psi and checked for leakage before every major data campaign. Secondly, check-valves that only allow gases to flow through in one way are installed at the fuel port inlet of the GTMC to ensure that no air will enter the fuel line during shut off. Check-valves are also installed in the seeding air line before the seeder, so that in case reverse flow occurs in the seeding line, the PIV seeding particles will not enter the upstream hydraulics and block small orifices. Thirdly, after the experiment is finished for the day, the entire fuel line is always entirely purged with nitrogen.

As for the high energy laser beam, the following actions were taken: *i*) a interlock was installed on the door of the lab so that if someone accidentally enters the room during a run, both lasers will be immediately shut off. *ii*) both the 532 nm and 355 nm light path have been checked with fluorescence paper to ensure that all major reflections from optics are stopped by beam stops. *iii*) a curtain made of light absorbing and fire-proof material has been put around the optical table where the two lasers are located, during a run the curtain is lowered so that no stray light will enter the room. *iv*) And even though the lasers can be directly controlled from their controllers, in the current setup they are controlled (through the RS-232 port) by two separate computers. This allowed the experiment operator to remotely control the laser power without the need to open the curtain to operate the controller, and thus

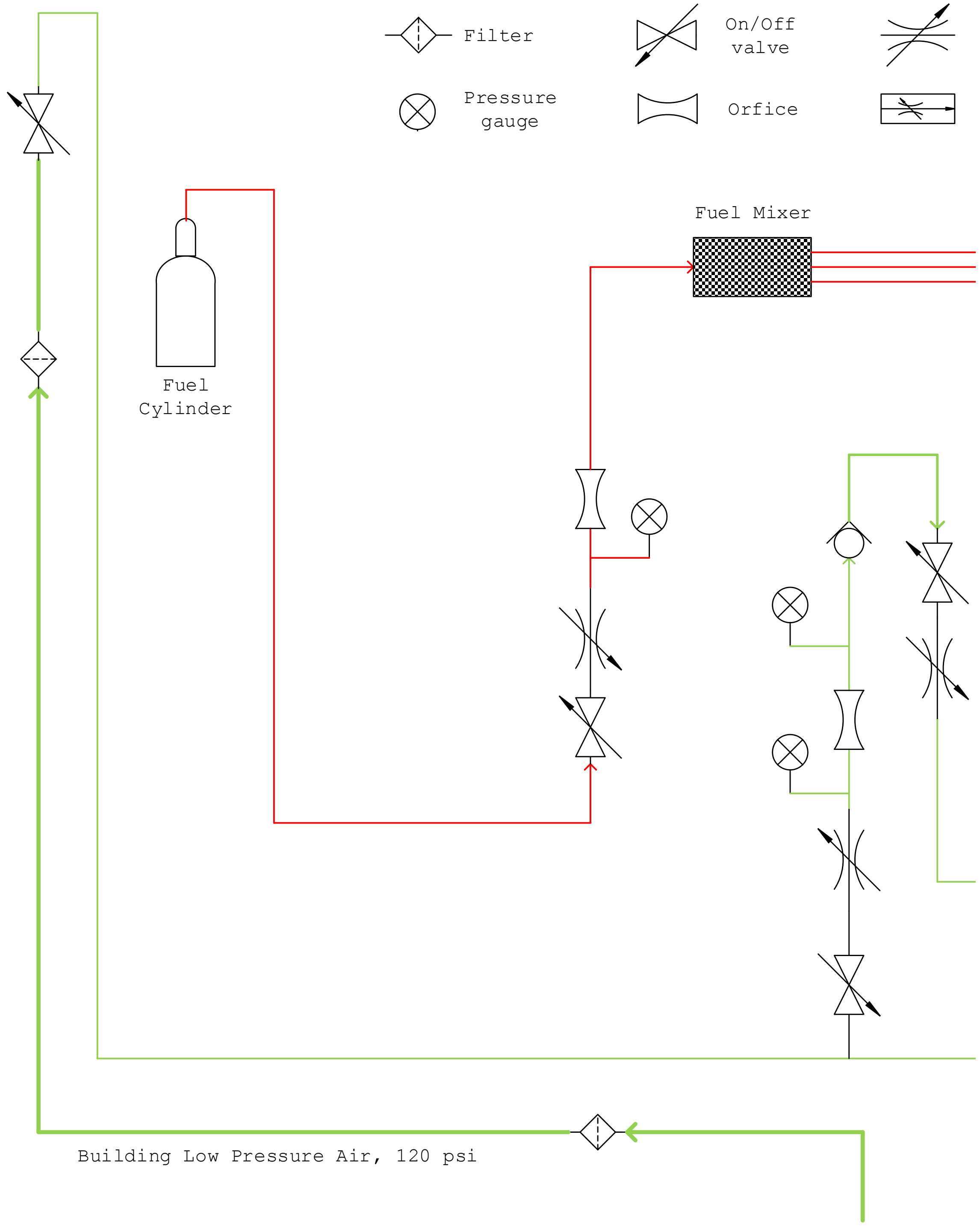

Figure 5.4: Schematics of the hydraulic system (Part 1/2), part of the figure is duplicated in the overlapping region between the two parts.

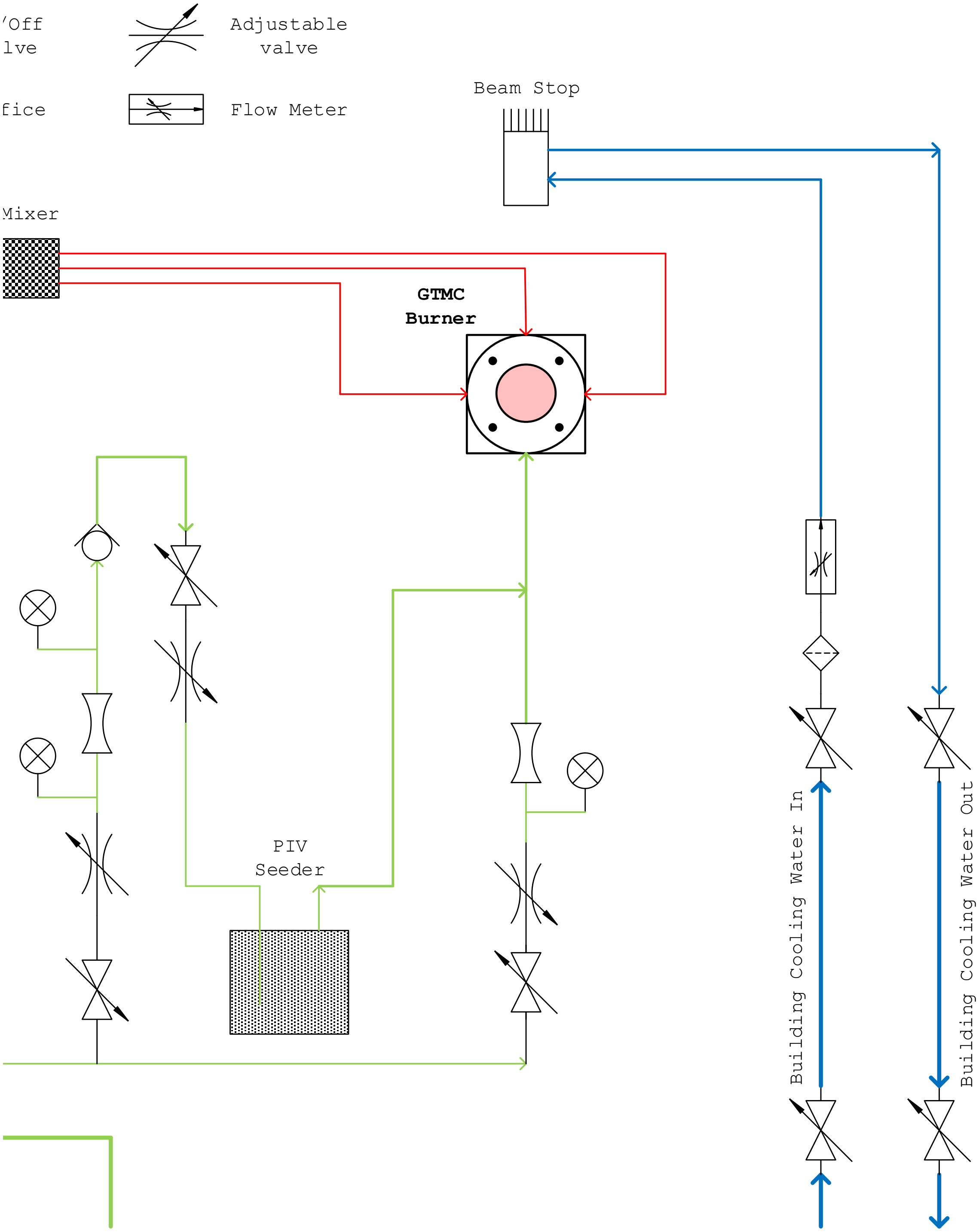

Figure 5.4: Schematics of the hydraulic system (Part 2/2), part of the figure is duplicated in the overlapping region between the two parts.

minimizes the exposure to hazardous UV laser light.

All of these precautions are enforced with the aid of a lab safety “check-list”, which is attached in appendix A. This check-list is followed so as to reduce the possibility of neglecting key steps in the operating procedures and resulting in potential safety hazards.

5.3 Data Processing

After the PLIF images and PIV images are obtained in the experiments, they have to go through a series of processing procedures before useful information can be extracted.

5.3.1 PIV data processing

The raw PIV images are processed by the LaVision Davis 8.0 software suite. After importing the images into the software, each pair of frames at a given time step are identified and bonded together. A non-linear sliding average subtraction is then applied to filter out the noises in the PIV images. In the next step the PIV vectors are calculated using the built-in solver, with a 64 pixels × 64 pixels interrogation window and 50% overlap for two rounds. The resultant vector fields (12 vectors × 12 vectors) are then filtered by a post-processing routine that removes the vectors that are more than twice the RMS values away from the average value. Figure 5.5 shows the resultant vector field for one of the cases studied in this work (case R1) at two randomly chosen instances. An average vector is obtained for the entire field of view at each time step for later spectral analysis.

5.3.2 Noise cancellation and edge detection procedure for PLIF images

A CH_2O PLIF image is a visualization of the concentration field of CH_2O, where signal strength is assumed to be proportional to the CH_2O concentration at the pixel. An “edge” of a “object” in the image would be the line defining a region of high concentration CH_2O. To be more specific, this edge line would be defined a narrow region where the local gradient of signal strength is large compared to the rest of the image. It has been demonstrated that the “sharp edges” in a CH_2O PLIF image correlates to the reaction zone of the flame [10, 70], hence can be used as an indicator for the spatial distribution of heat release. To accurately capture these edges, an algorithm has been developed to post-process the PLIF images. The schematic of this processing routine is illustrated in figure 5.6. The procedures are as follows:

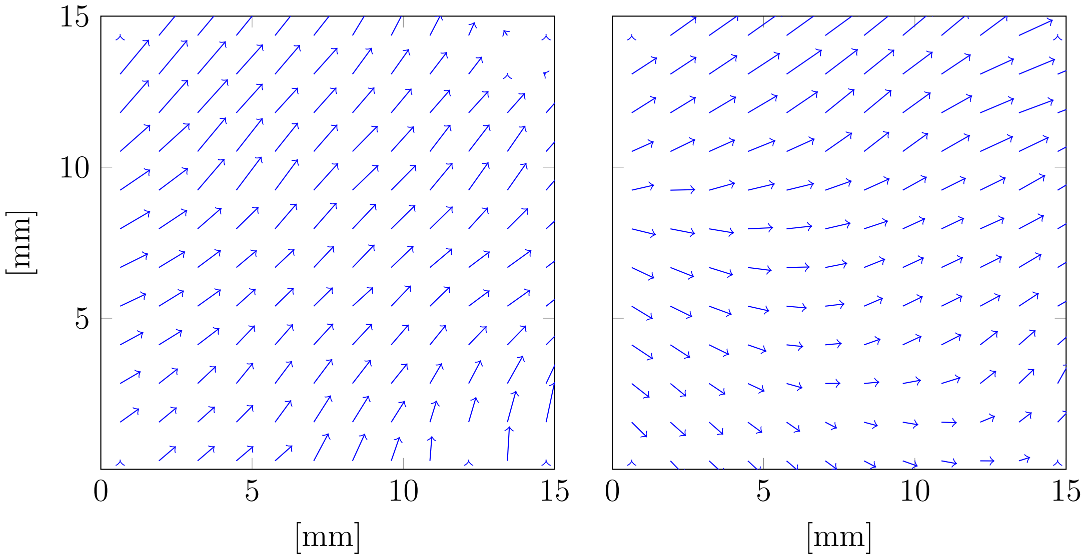

Figure 5.5: PIV vector field of case R1 at two random instances.

a) The raw image are imported into MATLAB, covered to a standard 16 bit image.

b) A dynamic thresh-hold selection routine determines the optimal threshold for noise cancellation. This routine has three options: 1) MATLAB built-in function "greythresh"; 2) Manual input (one level for all images); 3) Manually choose the threshold with a GUI tool for 20 randomly selected frames, then take the average of threshold levels chosen.

c) The input image from step a) is binarized, with the pixels with intensities larger than the threshold labelled as 1 and the rest as 0.

d) The binarized image is processed with MATLAB Image Processing Toolbox, structures whose area is smaller than a certain threshold is eliminated or filled in. This is used to reduce the "bright dot" noise. Afterwards, the edge in this cleaned binary image is detected by MATLAB function "edge" with canny edge detection method.

e) Raw image from step a) is multiplied with the binary "mask" generated in step d), hence produces a "cleaned up" version of the original data.

f) Result from step e) is subtracted from its base, so that all edge pixels are now all at "sea level."

g) A customized function is used to determine the gradient at each pixel that were deemed as edge in step d). Those whose gradient is larger than a certain threshold

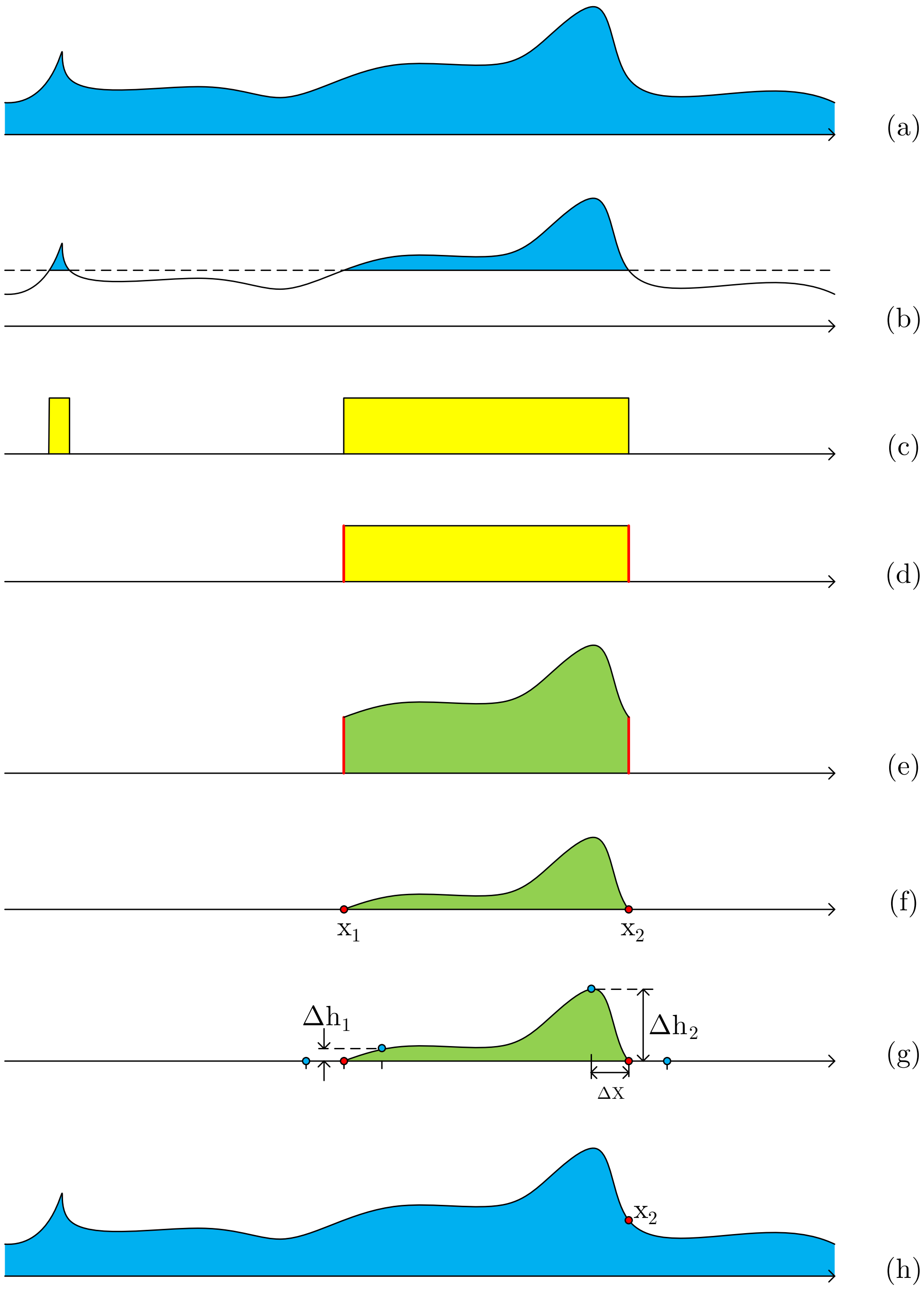

Figure 5.6: Illustration of the procedures of edge detection routine for PLIF images

is determined as flame front.

h) The determined edges are mapped back to the original image.

5.3.3 Stencil for gradient calculation

The customized function mentioned in step g) above utilizes a different stencil than conventionally used. In conventional techniques, the gradient is usually calculated locally in two directions, i.e., if we want to calculate the gradient at a point W in a image with coordinate $x = i$ and $y = j$, then its gradient ($\mathcal{G}$) is calculated as:

$$\mathcal{G}(W_{\mathrm{i,j}}) = \sqrt{\left(\frac{W_{\mathrm{i+1,j}} - W_{\mathrm{i-1,j}}}{2\Delta x}\right)^2 + \left(\frac{W_{\mathrm{i,j+1}} - W_{\mathrm{i,j-1}}}{2\Delta y}\right)^2} \ . \tag{5.1}$$

There are two issue with this traditional way of calculating the gradient. Firstly, if the grid spacing Δx or Δy is too small, as what will happen in a high resolution image, the local gradient will not be able to capture global structures. Hence the gradients calculated will be barely distinguishable. Secondly, this way of calculating gradients only considers the horizontal and vertical direction. If the edge is at a very sharp turn along a edge, this conventional way will not be able to correctly calculate the local maximum gradient.

Hence we propose a new way of calculating local gradient, with a "single maximum" algorithm. Mathematically, it states that:

$$\mathcal{G}(W_{\mathrm{i,j}}) = \left| \frac{W_{\mathrm{m,n}} - W_{\mathrm{i,j}}}{\sqrt{(m-i)^2\Delta x^2 + (n-j)^2\Delta y^2}} \right| , \quad W_{\mathrm{m,n}} = \max(W \in \mathcal{S}) \ , \tag{5.2}$$

where $W_{\mathrm{m,n}}$ is the pixel with the highest intensities in the stencil $\mathcal{S}$. The stencil in our current study is a square belt of points that are 10 pixels alway horizontally or vertically from the point of interest $W_{\mathrm{i,j}}$.

5.3.4 Determination of the gradient magnitude threshold

After the magnitude of the gradients at all edges are identified (step g) in section 5.3.2), we have to separate the edges that have small gradients (assumed to be caused by thermal decomposition of fuel) and those with larger gradients (assumed to be flame front). This is done through a statistical approach. In figure 5.7a the probability distribution of the magnitude of gradients at edges of all 4000 frames of case R1 data is presented in the black line. We can see that it resembles a normal

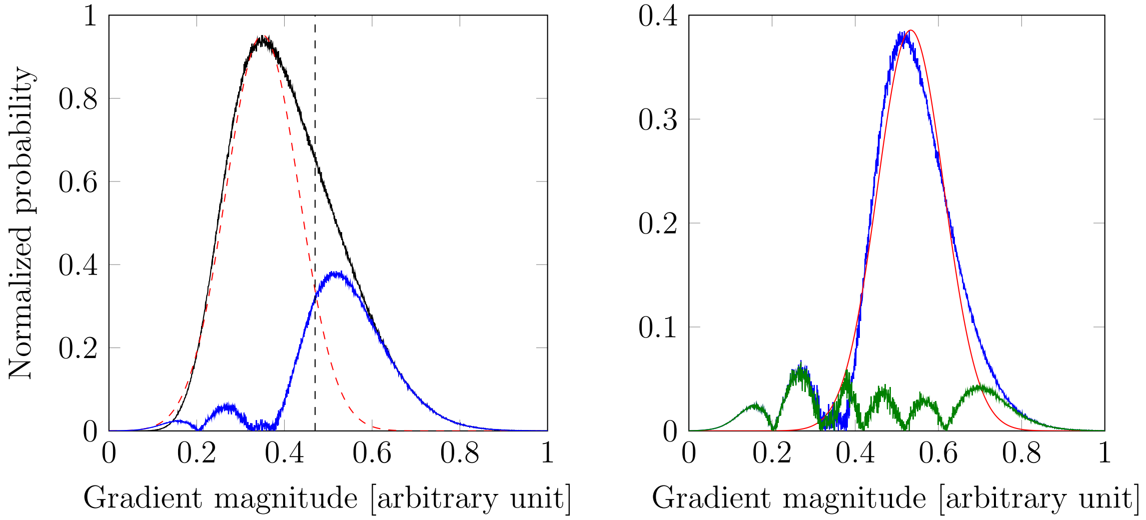

(a) The total distribution (black solid) is fitted with a normal distribution (red dash), the residue is plotted as solid blue line. The threshold for flame surface is shown as the black dashed line.

(b) The residue from 5.7a (blue) is fitted with another normal distribution (red), absolute value of their difference (green) does not shown statistical significance.

Figure 5.7: PDF of edge gradients of all frames in case R1.

distribution but it is asymmetrical. If we fit the total gradient PDF with a normal distribution curve (the red dashed line), we would realize that the absolute value of the residues (blue line) resembles another normal distribution.

In figure 5.7b we zoom in to the residue PDF obtained from figure 5.7a (still in solid blue line). If we fit the residue PDF with another normal distribution curve (solid red line), we can see that the two are very close, and in this case the absolute value of their difference (dark green line) is close to noises without any statistical significance.

Hence we can think of the total gradient PDF (black line in figure 5.7a) as being composed of two normal distributions (dashed red line in figure 5.7a and solid red line in figure 5.7b). The mean of these two normal distributions are two standard deviations away from each other, so they are likely to be representing two independent physical phenomena. In our case, it is hypothesized that the former represent the fuel thermal decomposition process, while the latter represent flame surfaces. Hence the threshold are set at the line one standard distribution away from each normal distribution (black dashed line in figure 5.7a) to minimize the statistical interference.

Other cases follow the same processing routine. The result of the entire processing routine (detailed in section 5.3.2, 5.3.3, and 5.3.4) is demonstrated in figure 5.8.

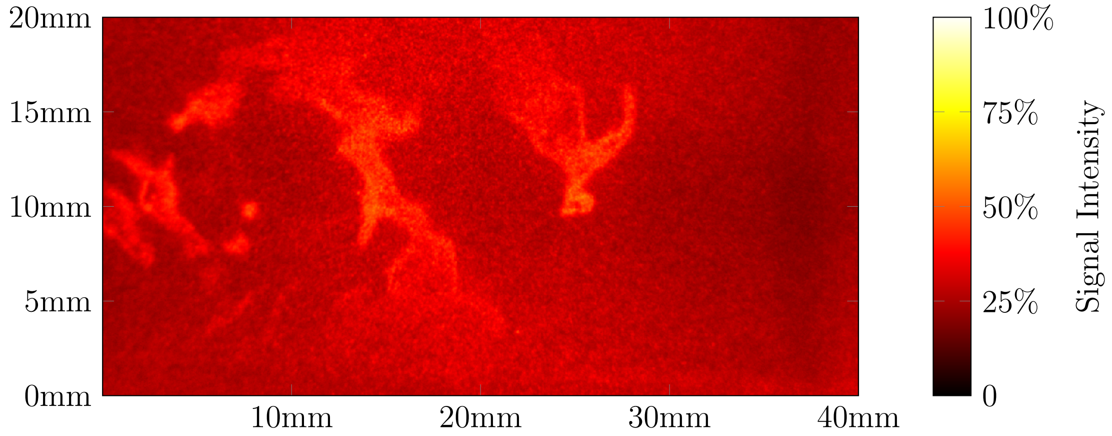

(a) Raw PLIF image before processing

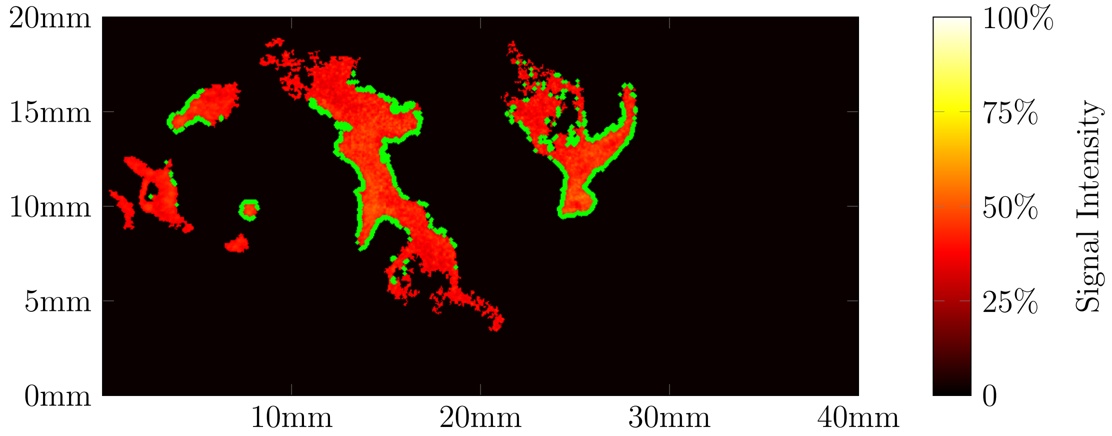

(b) PLIF image after processing, with green dots indicating identified flame surfaces

Figure 5.8: Example of PLIF processing result.

5.3.5 Superimposition of PIV vectors with PLIF images

After properly processing the PLIF images, we process our PIV images with LaVision Davis 8.1 software. Then the only remaining task is to properly superimpose the velocity vectors onto the PLIF image. Before the experiment, a transparent target with black crosses is placed on top of the burner at the focusing plane. The PIV camera and PLIF camera both take a photo of the target, the two images will appear inverted each other. Afterwards we manually locate the center of each cross on both images with their corresponding pixel index. If we locate two such centers (R and T) on each image ($\mathrm{R}_{\mathrm{PIV}}$, $\mathrm{R}_{\mathrm{PLIF}}$ and $\mathrm{T}_{\mathrm{PIV}}$ and $\mathrm{T}_{\mathrm{PLIF}}$), then the transformation relation between these two frames is governed by matrix $\mathcal{M}$:

$$\begin{bmatrix} X_{\mathrm{R,PIV}} & X_{\mathrm{T,PIV}} \\ Y_{\mathrm{R,PIV}} & Y_{\mathrm{T,PIV}} \end{bmatrix} = \mathcal{M} \cdot \begin{bmatrix} X_{\mathrm{R,PLIF}} & X_{\mathrm{T,PLIF}} \\ Y_{\mathrm{R,PLIF}} & Y_{\mathrm{T,PLIF}} \end{bmatrix} . \tag{5.3}$$

Hence $\mathcal{M}$ can be obtained through matrix inversion of the two set of coordinates. Since we have 15 cross centers in our test frame, we need to find one transformation that minimizes the distortion across all points. This is achieved by defining a error matrix $\mathcal{E}$:

$$\mathcal{E} = \begin{bmatrix} X_{\text{R,PIV}} & X_{\text{T,PIV}} \\ Y_{\text{R,PIV}} & Y_{\text{T,PIV}} \end{bmatrix} - \mathcal{M} \cdot \begin{bmatrix} X_{\text{R,PLIF}} & X_{\text{T,PLIF}} \\ Y_{\text{R,PLIF}} & Y_{\text{T,PLIF}} \end{bmatrix} , \tag{5.4}$$

and use MATLAB built-in optimizer "fmincon" to find a transformation matrix $\mathcal{M}$ that minimizes $|\mathcal{E}|$. After obtaining this optimized $\mathcal{M}$, we tested it with two of our reference frame and overlaid them in figure 5.9. In the figure, the background is the photo of the target taken from PIV camera, the center of white circles indicates the center of the same cross on a PLIF image after being transformed into PIV image coordinates. We can see that the center of the white circles and the black crosses mostly coincide with each other, which means that we are properly superimposing the two frames.

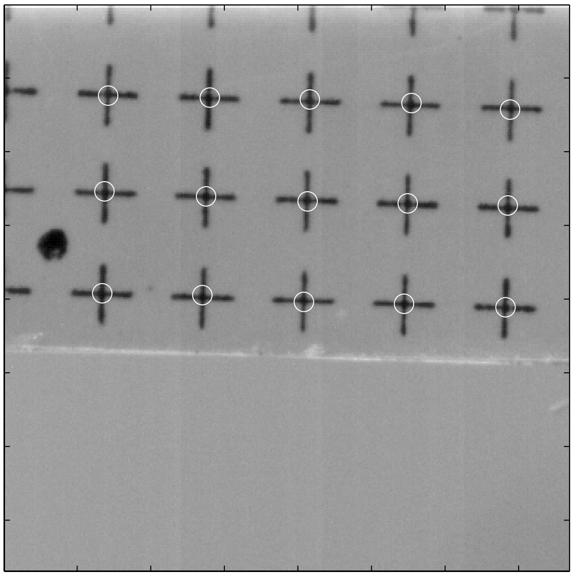

Figure 5.9: Example of coordinate transformation between PIV image and PLIF image. Back ground is the target with crosses as seen from the PIV camera, the center of white circles indicates the center of the same cross on a PLIF image after being transformed into PIV image coordinates.

Table 5.2: Test case matrix

Case	$\phi = 1.2$	$\phi = 1.0$	$\phi = 0.75$
$\dot{m}_{\mathrm{a}}$=282g/min	R1	S1	L1
$\dot{m}_{\mathrm{a}}$=226g/min	R2	–	–

5.4 Results

5.4.1 Test case matrix

In section 5.2.4 we already provided the parameters of our test matrix flow rates. Here we reorganize this information in a different format in table 5.2.

As shown, we consider four test cases in the present study. At the air flow rate of 282 g/min (which corresponds to case "B" in DLR experiments), we have three cases: R1 (R:rich), S1 (S:stoichiometric), and L1 (L:lean) with equivalence ratio of 1.2, 1.0, and 0.75 respectively. In a reduced flow rate of 226 g/min (80% of standard case), we repeat the experiment for the rich case (R2).

The test case matrix is designed in such a way to explore: *i*) the differences in spatial and temporal structure of a unstable (R1) and a stable (L1) flame; *ii*) investigate the intermittent instability case at stoichiometric condition (S1); *iii*) explore the effect of reducing mass flow rates (between R1 and R2).

5.4.2 Spectrum of pressure

Thermo-acoustic instability is characterized by a large pressure fluctuation in the combustion system. So we start our presentation with the pressure spectrum to characterize the four cases in this study.

Figure 5.10 shows the power spectrum of all four cases, normalized by a reference power E_{P} in arbitrary unit. We can see from the first row that the pressure spectrum between a unstable case (R1) and a stable case (L1) is very distinct. Whereas R1 has a single peak in 310∼320 Hz range, L1 has no prominent peak that is visible in the current scale. The spectrum of S1 (stoichiometric) is similar to that of R1, with a peak at the thermo-acoustic instability frequency of 310 Hz at a smaller magnitude (0.07 E_{P}). The single peak in R2 is smaller than R1 (0.15 E_{P} vs. 0.8 E_{P}), its frequency also shift into around 290 Hz range. This means that as mass flow rates decreases, the instability becomes weaker and shifts to a lower frequency.

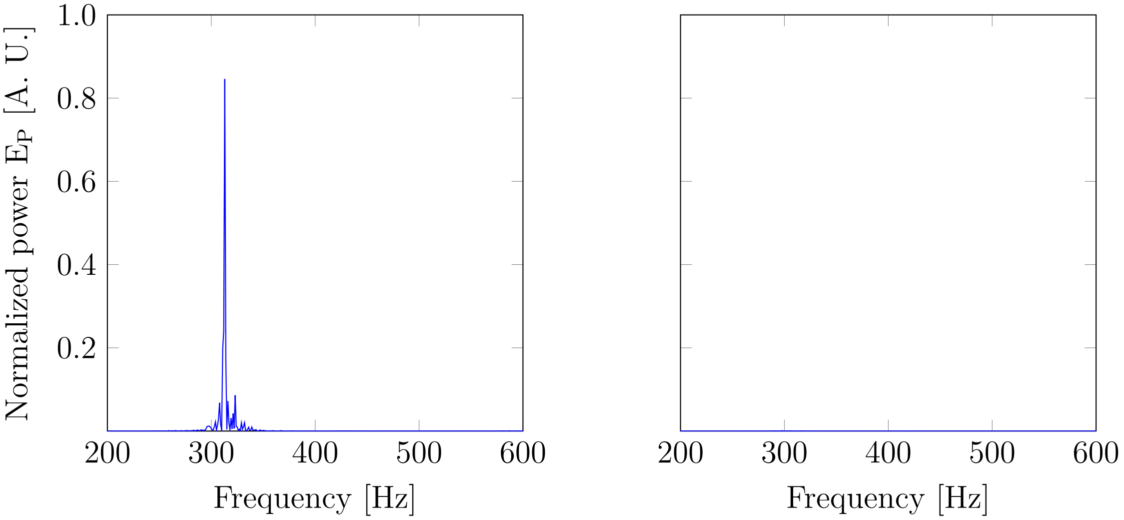

(a) Case R1 (rich, unstable)

(b) Case L1 (lean, stable)

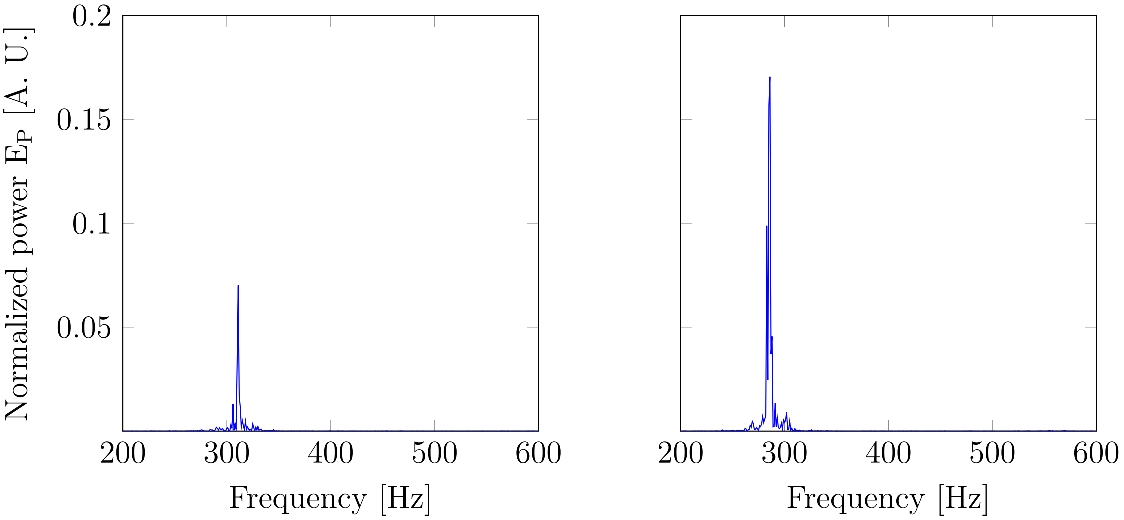

(c) Case S1 (stoichiometric, intermittent)

(d) Case R2 (rich, smaller flow rate, weakly unstable)

Figure 5.10: Pressure power spectrum of all four cases, normalized by a reference power E_{P} in arbitrary unit.

5.4.3 Spectrum of flame surface area

We assume that the integral of the flame surface area within each frame is proportional to the total heat release rate:

$$\dot{Q} \sim \sum_{A} l_{\mathrm{FS}} \tag{5.5}$$

where $\dot{Q}$ is the total heat release rate in a frame, l_{FS} is the flame surface length, and A is the area of the entire frame. Hence the fluctuations of heat release rate can be calculated from the fluctuations of the total flame surface area in each frame. In figure 5.11 we present the power spectrum of the fluctuations of the total flame surface area as identified by our edge detection algorithm.

We can see that the power spectrum of flame surface area gives us a series of new information. In the case of R1, flame surface area fluctuates at a single frequency, same as the pressure. We did not see any peaks in the pressure spectrum of L1, but the flame surface area has a very strong peak at 420 Hz. This is caused by the helical Precessing Vortex Core (PVC) that is rotating around the swirler. This flow feature has been well characterized by literature. The proof of the existence of PVC can be found in the velocity analysis later. While PVC rotates in the combustion chamber, it takes reactants and products with it. Hence there will be a overall fluctuation of CH_2O signal strength in the frame. Whether this is a artifact of image processing routine or it indicates actual heat release fluctuation has to be verified with velocity and pressure data. We see that the pressure spectrum of L1 is almost flat in this range, hence it is very unlikely that we are having a strong heat release oscillation at 420 Hz at the same time. Hence the fluctuation of flame surface area is unlikely to be linked to fluctuation of heat release rate. The effect of PVC is also evident in S1, albeit with a smaller magnitude. R2 on the other hand only shows a single peak at the themo-acoustic instability frequency of 290 Hz. This is similar to R1, only at a smaller magnitude.

5.4.4 Flame surface density

The information of flame surface length inside a local region can also be used to calculate flame surface density (ρ_{FS}), which represents the average flame length inside a volume (or a region in 2D images) by:

$$\rho_{fs} = \lim_{\Delta x \to 0} \frac{\sum_{\Delta A} l_{fs}}{(\Delta x)^2} \tag{5.6}$$

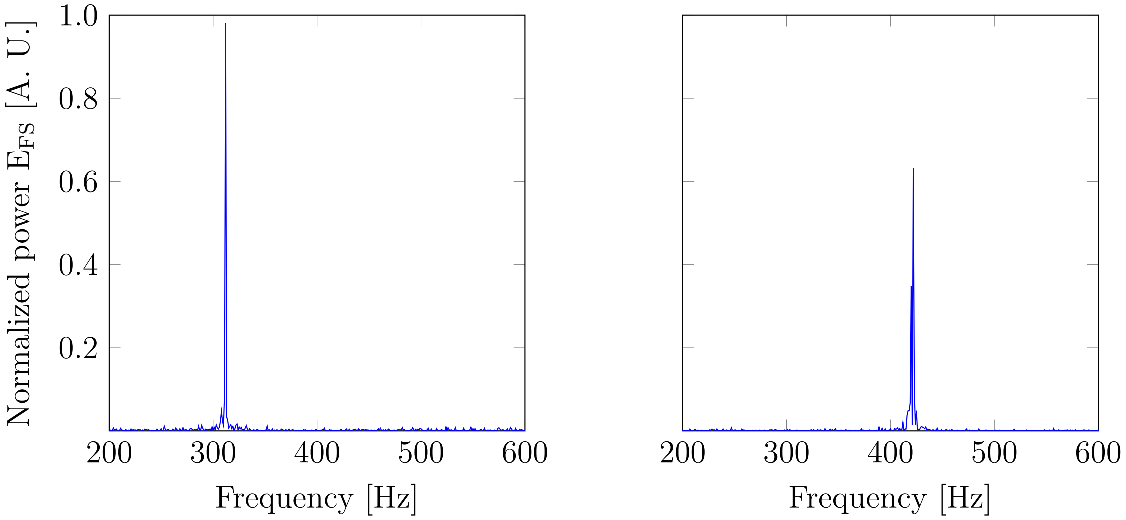

(a) Case R1 (rich, unstable)

(b) Case L1 (lean, stable)

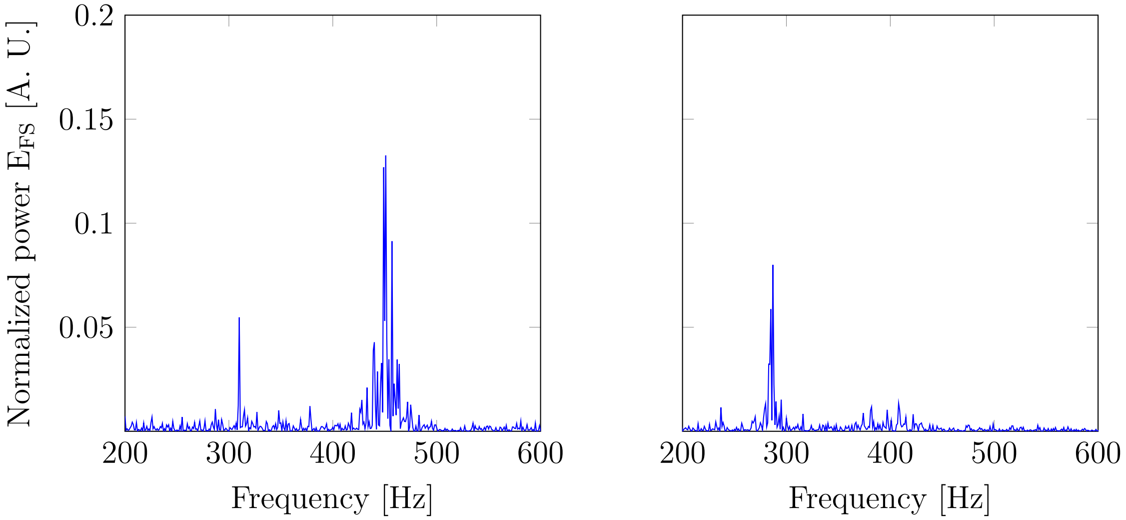

(c) Case S1 (stoichiometric, intermittent)

(d) Case R2 (rich, smaller flow rate, weakly unstable)

Figure 5.11: Total flame surface area power spectrum of all four cases, normalized by a reference power E_{FS} in arbitrary unit.

where Δx is the length of the region (bin size) and ΔA is the area of the region (bin area). The importance of flame density is that it not only indicates where the flame wrinkling is most intense, it is also believed to be directly related to local volumetric heat release rate $\dot{q}$:

$$\rho_{fs} \sim \dot{q} \ . \tag{5.7}$$

Hence the flame surface density indicates the spatial distribution of heat release intensity. Figure 5.12 shows the flame surface density of all four cases in the present work.

We can see that the spatial distributions of R1 and L1 are quite different. Flame in R1 is quite concentrated and flat, near the burner surface. The flame in L1 is more lifted, showing a "V" shape. This agrees with previous chemiluminescene measurements made by Allison et al. [9]. The shape of S1 is a combination of those of R1 and L1, again indicating that S1 is in the transition process. Lastly R2 is also concentrated like R1, but the average flame surface density is lower and its more lifted, both indicating that the flame in R2 is not as intense as that in R1.

5.4.5 Axial and Radial power spectrum

As shown in figure 5.1, the PIV FoV is positioned right at the exit of the swirler. In this way we can capture a fairly uniform flow field in our frame before it is perturbed by the flow field inside the chamber. After processing the PIV images in LaVision Davis software with a 64 × 64 pixels window and 50% overlapping ratio, we obtained a matrix of 12 × 12 vectors per frame. After averaging through all 144 vectors in their axial and radial velocity component, we can estimate the average axial and radial velocity in our FoV. A Fast Fourier Transform (FFT) analysis is carried out to explore the frequency spectrum of both velocity components.

Figure 5.13 shows the power spectrum of two of the velocity components for case R1, which represents an unstable flame. To properly compare the two components, we normalized both of them with an arbitrary unit (A.U.). This arbitrary normalizing factor is kept constant through the analysis in this section. We can see that in a unstable flame, the radial velocity fluctuation is much larger than that of the axial velocity. There are two distinctive peaks in the radial velocity spectrum, the first one is at 319 Hz and the second one is at 466 Hz. The 319 Hz peak corresponds to the thermo-acoustic instability frequency, while the second peak is the rotating frequency of a helical PVC which is also observed in the DLR experiments [64].

Figure 5.14 shows the same information as in figure 5.13 for the stable case L1. We

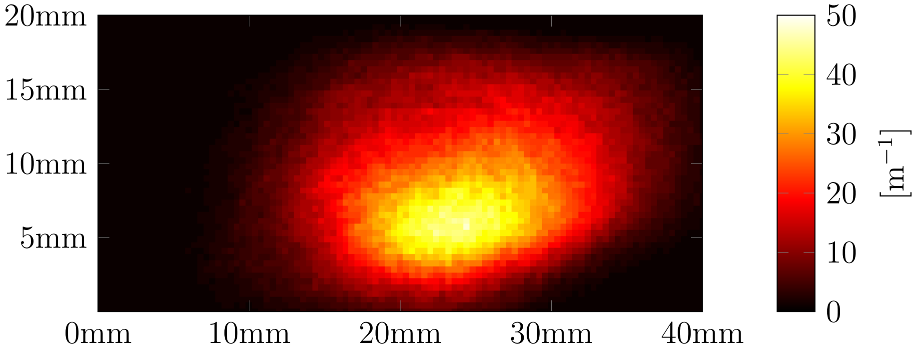

(a) Case R1 (rich, unstable)

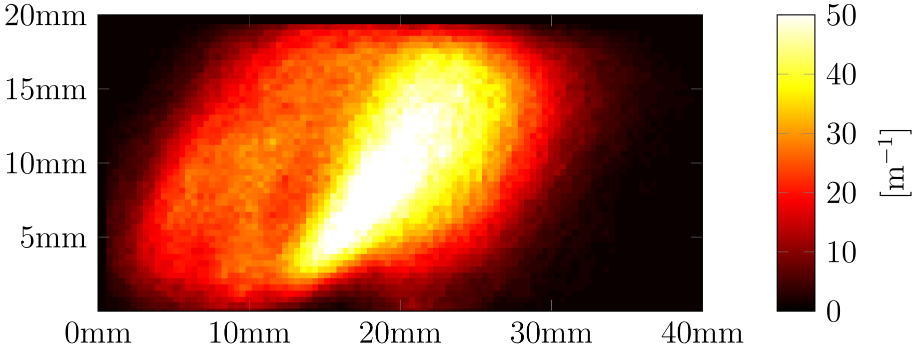

(b) Case L1 (lean, stable)

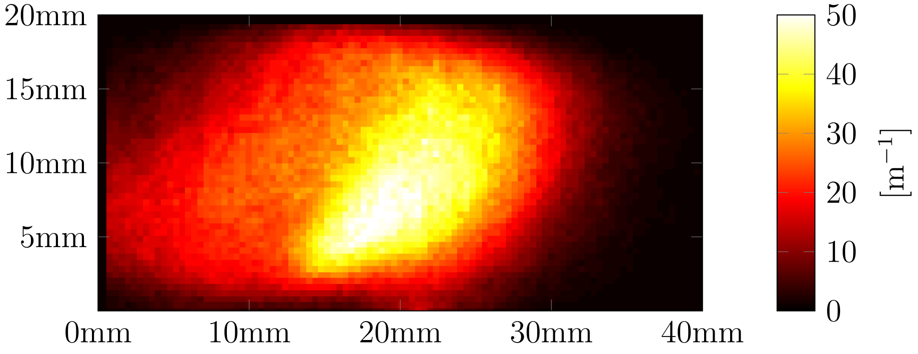

(c) Case S1 (stoichiometric, intermittent)

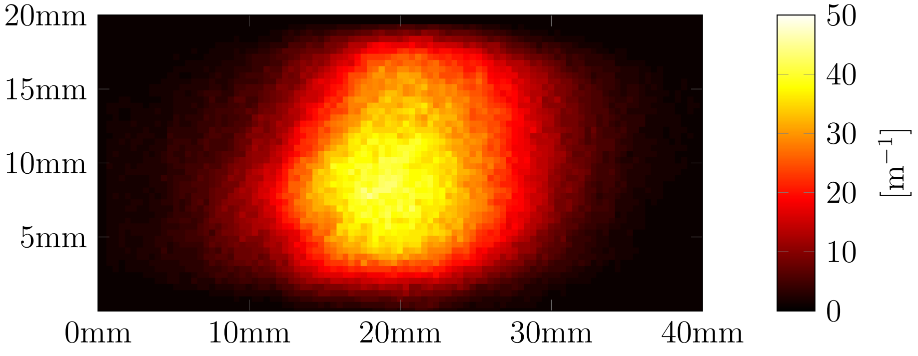

(d) Case R2 (rich, smaller flow rate, weakly unstable)

Figure 5.12: Flame surface density for all four cases, in [m^{-1}].

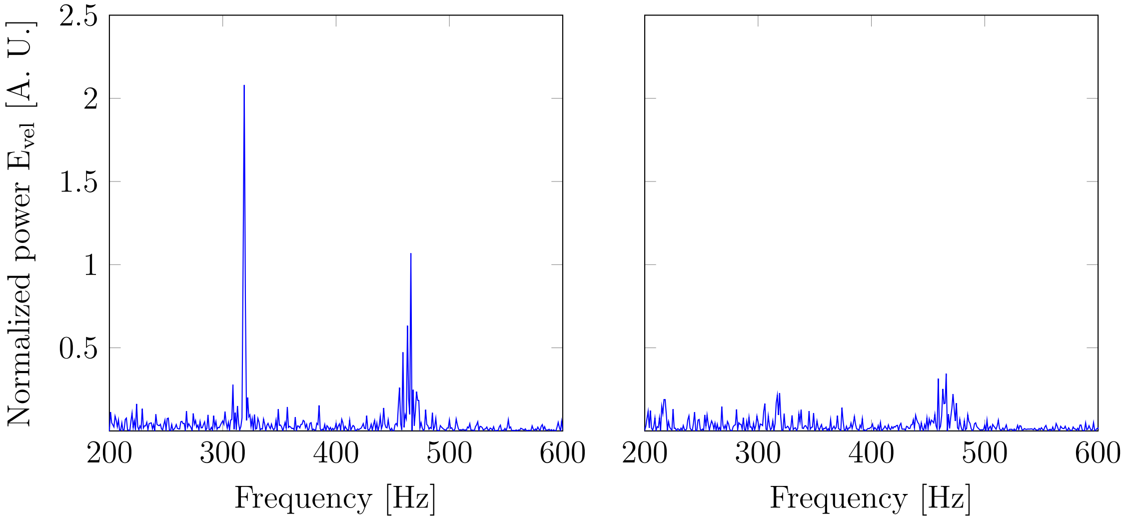

(a) Radial velocity

(b) Axial velocity

Figure 5.13: Case R1 (rich) velocity power spectrum

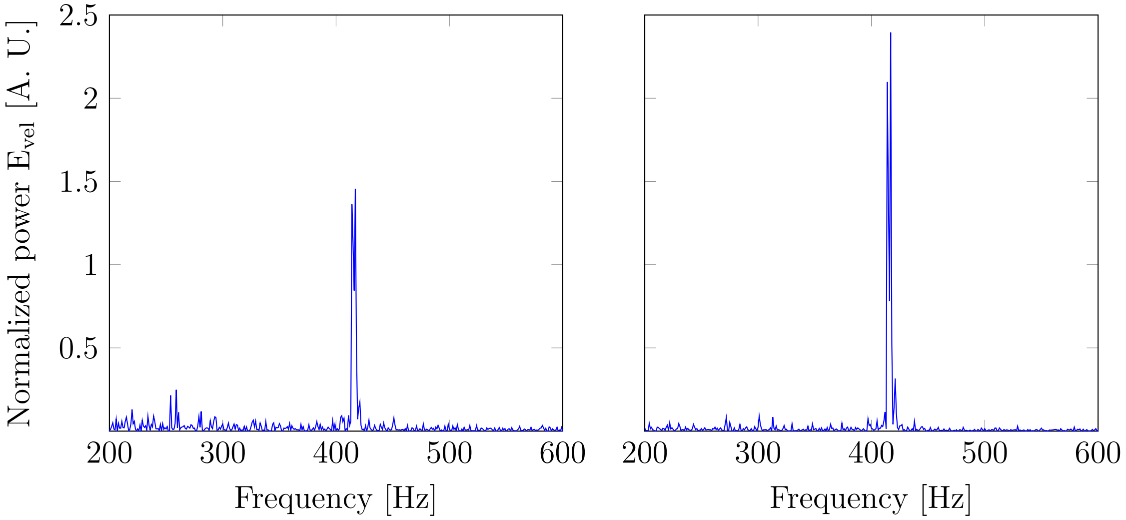

(a) Radial velocity

(b) Axial velocity

Figure 5.14: Case L1 (lean) velocity power spectrum

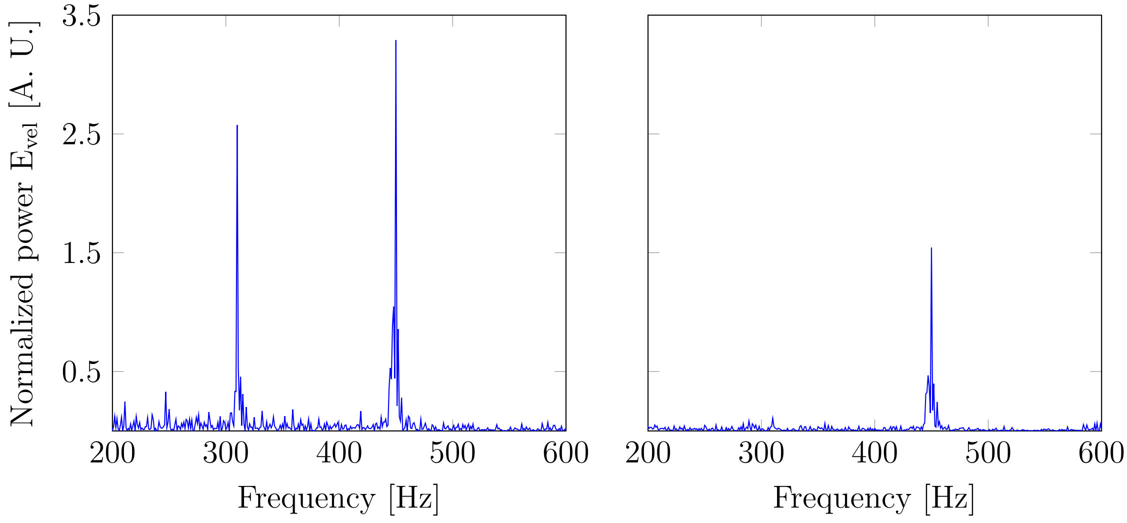

(a) Radial velocity

(b) Axial velocity

Figure 5.15: Case S1 (stoichiometric) velocity power spectrum

can see that in this stable flame, the thermo-acoustic instability frequency (∼300 Hz) no longer exists in either velocity components. Only the PVC frequency is present at 417 Hz. Also in L1 flame at the same location axial velocity fluctuation appears to be larger than that of the radial velocity fluctuation. Both velocity components having a strong peak at the PVC frequency means that in this case PVC is strong affecting the flow pattern.

Figure 5.15 shows the velocity component information for the case S1 (stoichiometric). This case is experimentally categorized as being "intermittently unstable." Its spectrum shows the features of the stable case (L1) and the unstable case (R1). Like R1, we can see two distinct peaks in the radial velocity spectrum, corresponding to thermo-acoustic instability frequency at 310 Hz and PVC frequency of 450 Hz. At the same time, we see that in R1 there are no peaks in spectrum for axial velocity but in S1 there is a peak at the PVC frequency, more like that of L1. The reason for this behavior of S1 can be attributed to the fact that it can be considered as the transition phase from stable regime to unstable regime. Hence the temporal trace of velocity represents the superposition of instances of stable and unstable flames. Another feature of S1 is the large velocity fluctuation magnitude of both axial and radial velocity compared to previous cases. This may be caused by the frequent reposition of the flow during the transition period.

Figure 5.16 shows the velocity distributions of case R2, which is fuel rich (ϕ=1.2) but only with an air flow rate only 80% of R1 (226 g/min vs. 282 g/min). We can

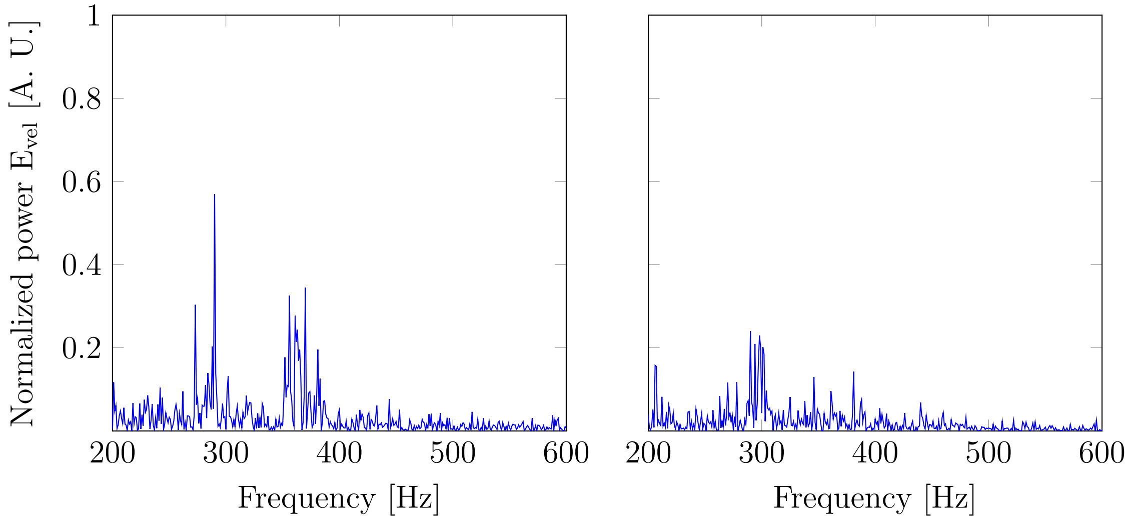

(a) Radial velocity

(b) Axial velocity

Figure 5.16: Case R2 (rich, smaller flow rates) velocity power spectrum

see spectrally it is much more noisy than those of all previous cases. In the spectrum of radial velocity, we can still recognize the thermo-acoustic frequency of 290 Hz and PVC frequency $370 \sim 380$ Hz. In the axial velocity spectrum, we can recognize the thermal-acoustic instability at 290 Hz, but it is very much buried into other noises. This behavior of velocity spectrum corresponds to our experimental observation of a weak instability, in which the fluctuation of pressure is continuous but at the small amplitude. With a smaller flow rate, R2 still keeps the same features as R1, only at a much smaller magnitude.

5.4.6 Spectrum of the total velocity magnitude

Instead of the looking at the axial and radial components of the velocity, we now look at the magnitude of the velocity vector, which is the vector sum of both radial and axial velocities. In a rough sense, this can be considered as a representation of the total mass flow rate fluctuation.

The power spectrum of velocity vector magnitude is plotted in figure 5.17. Understandably this is the result of the superimposition of both the radial and axial velocities shown in the previous section. Here the power is still normalized by E_{vel}, an arbitrary but fixed reference value. The velocity magnitudes are plotted at the same scale for direct comparison. We can see that in R1 both the thermo-acoustic instability and PVC affect the overall velocity magnitude (and hence mass flow rate), with the former being the dominant force. In L1, the fluctuation of velocity is solely

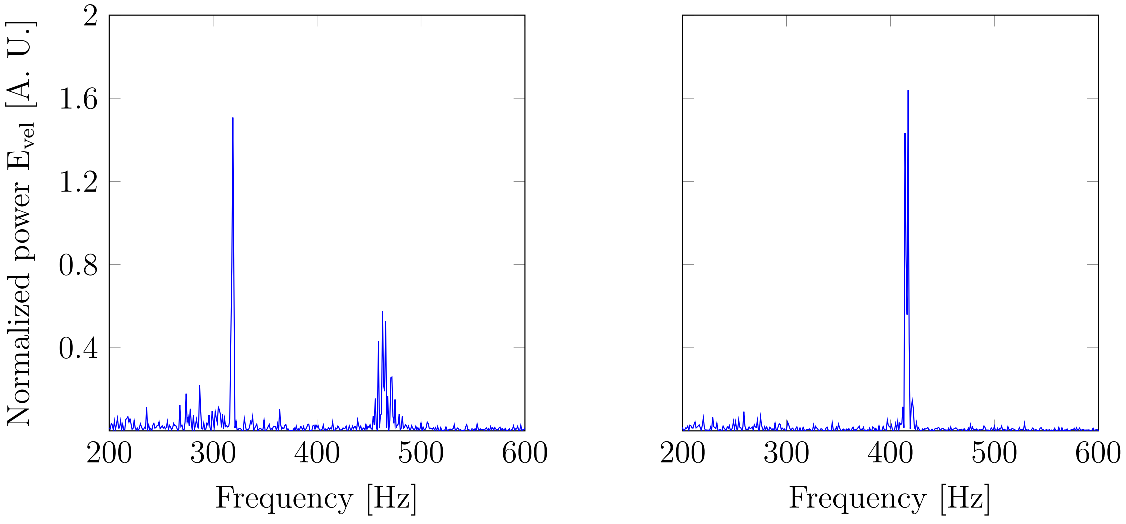

(a) Case R1 (rich, unstable)

(b) Case L1 (lean, stable)

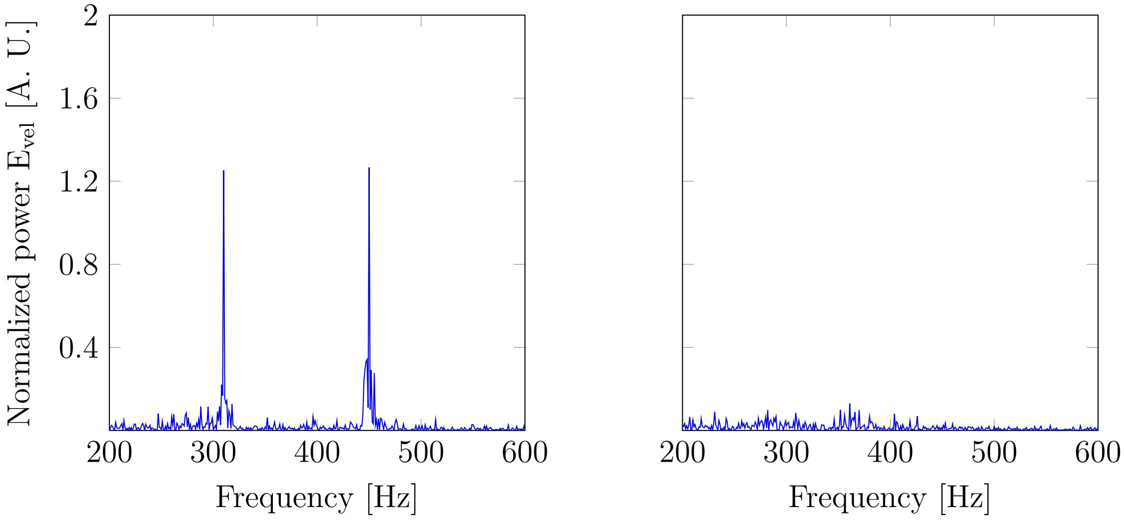

(c) Case S1 (stoichiometric, intermittent)

(d) Case R2 (rich, smaller flow rate, weakly unstable)

Figure 5.17: Velocity vector magnitude power spectrum of all four cases, normalized by a reference power E_{vel} in arbitrary unit.

attributed to PVC. S1 is a combination of R1 and L1, with thermo-acoustic instability and PVC play equally important roles. And lastly, in R2 the fluctuation of velocity is small compared to the previous cases. This means that the mean mass flow rates have a larger impact on the velocity magnitude than either combustion instability or PVC.

5.5 Discussion and Comparison with MRMF Predictions

The experimental analysis above encompasses pressure, velocity, and heat release (with flame surface as a proxy) measurements for four different operating conditions. A wide range of differences between each case have been observed, from which we have the following findings.

i) The formaldehyde kilohertz PLIF data provided spatially-resolved contours of the flame surface density, which are indicators of the contours of heat release rate. Thus PLIF provides better-resolved information about the spatial variation of the heat release rate than chemiluminescence. The kilohertz PLIF data showed that the spectrum of flame surface density oscillations has a sharp spike at the same frequency as the spike in the pressure spectrum. This proves that the heat release rate is coupled to the pressure fluctuations. The kilohertz PIV data showed that the velocity field also oscillates at the same frequency as the pressure oscillations in an unstable flame. This allows us to measure the relative phases between these quantities if proper spectral filtering is applied.

ii) From previous studies by Allison et al. [10] we already know that pressure fluctuation magnitude and flame surface density distribution are different between an unstable (R1) an stable (L1) flame. Velocity spectrum analysis in this study revealed that the effect of combustion instability would change the axial and radial velocity distribution as well. In an unstable flame the major dynamics happened in the radial direction, with velocity undergoing a large oscillation radially. In a stable flame the velocity oscillation was more evenly distributed between axial and radial directions. Considering that the flame in an unstable case sits in the outer recirculation zone, it's the radial velocity component of the swirler jet that is being "pushed" by the flame back and forth. We are not arguing whether the velocity re-distribution is the cause or the effect in this process, but we do find the links between velocity and heat release.

iii) We also gained some insights on the relationship between PVC and combustion instability. Again from velocity analysis we can see that PVC was present in both R1 and L1 flame. From L1, S1 to R1, the frequency of PVC was decreasing almost linearly, which corresponds to the decrease of mass flow rate. This means that the presence of combustion instability did not quite affect PVC. In the meantime, in flame R2, we did not see evidences of PVC, but we still saw a clear peak in pressure oscillation. This means that while instability and PVC do work together in determining the velocity distribution, physically the two are quite independent phenomena in nature.

iv) The pressure spectrum of S1 (intermittent instability) and R2 (weak instability) were very similar, but they represented two very different kinds of flame. The former, as transitional state at the stability limit, always possessed the features of both R1 (unstable) and L1 (stable) flame. S1 can be thought of as a temporal average of R1 and L1. R2 represented a different physical process. At a lower flow rate, from flame surface density we saw that the flame was more lifted off and less intense. The velocity magnitude fluctuation was also fairly small compared to R1, L1, or S1. This leads us to believe that a reduced flow rate made the flame "milder" even though equivalence ratio still determines the characteristics of the instability.

Compare these experimental observations with the assumptions of our reduced order model MRMF, we realize that:

- Just as what we hypothesized in our heat release model of MRMF (*Module Q2*), the fluctuation of velocity (and hence mass flow rates) does not necessarily generate combustion instability. In L1 we could see large velocity fluctuations caused by the PVC, but no pressure fluctuation was observed. In this case we think that it is the equivalence ratio, which determines whether fuel or air is the deficient and thus controlling stream, that matters.

- From the experiment, there is clearly a feed-back loop between heat release fluctuation and radial velocity oscillation. In our model we considered a simple condition of axial flow, and related the heat release rate fluctuation to axial instead of radial velocity. This may not be very descriptive in GTMC.

- Related to the previous point, our estimation of convection time delay τ_c was based on axial velocity and flame lift off height. However in the present study the proper time delay between injector and flame front may be more related to the horizontal displacement of the flame and the radial velocity.

- As we have foreseen, there are complex flow phenomena in the combustion, such as the PVC, that play important roles in determining the flow features inside a combustor. Our model is not capable of providing spatial predictions, hence this may be a source of error.

Even though experimental data reveals some of the limitations of our reduced order MRMF model, we need to realize that our simple model is able to predict the the existence and the frequency of combustion instability in different equivalence ratios, geometrical parameters, and mass flow rates with reasonable accuracies. This already allows it to be used as a fast first-order estimation tool for a complex combustion system.

CHAPTER VI

Summary and Conclusions

6.1 Summary

In this thesis, we looked into several aspects of partially premixed combustion.

In the first part (chapter II), we focused on the computational investigation of a well established partially premixed combustion setup. This numerical work was focused on using Large Eddy Simulation (LES) coupled with the Flamelet/Progress Variable (FPV) model to study the Sydney Piloted Premixed Jet Burner (PPJB). The applicability of FPV model to this highly turbulent partially premixed combustion regime was assessed. In addition, a new approach for the joint probability function between the two mixture fractions in this three-stream problem was proposed. Comparisons of key flow variables and species concentrations between simulation results and experimental data were in good agreement. The limitations of the FPV combustion model in regions of local extinction and re-ignition were also analyzed. This study also illustrated the costs and uncertainties that current state of the art high fidelity combustion models incur when simulating a moderately complex configuration.

In the second part (chapter III), we developed a Modular Reduced-order Model Framework (MRMF) to describe the combustion instability phenomena that usually occurs in confined combustion systems. This framework was built with a modular approach, making it easy for its sub-models to be replaced or upgraded. The geometry that our present model is based on is the DLR Gas Turbine Model Combustor (GTMC). Its geometry was abstracted into a series of four connected zero dimensional chambers. A multi-chamber Helmholtz analysis was carried out to model the pressure fluctuation inside the major chambers, while simple heat release and velocity coupling models were proposed for completing the feedback loop between heat release fluctuation and pressure oscillation.

In the third part (chapter IV and V), we used experimental techniques to assess the validity and predictions of our proposed model on the GTMC. In chapter IV we used multi-point pressure measurement to confirm that the system was indeed dominated by a Helmholtz type instability, which validated our model assumption. After estimating a series of parameters, we then used our model to explain the dependence of instability frequency on geometrical parameters, flow rates, and equivalence ratios. In chapter V, we used high speed Planar Laser Induced Fluorescence (PLIF) and Particle Image Velocimetry (PIV) along with pressure measurements to study the interactions between pressure, heat release, and velocity in detail. Results from this section agree with our hypothesis for the reduced order model that combustion instability is controlled by flow rate of the deficient stream (air or fuel). It also deepened our understanding about the interactions between combustion instability and flow patterns such as velocity distribution and Precessing Vortex Core (PVC).

6.2 Conclusions

Key conclusions from this work are:

- After extending the Flamelet/Progress Variable (FPV) model with a Dirichlet distribution as the new presumed PDF, the current approach is capable of predicting temperature and species concentrations in a partially premixed combustion regime. Specifically, Dirichlet distribution accurately describes the three stream mixing process happening in the SydneyPiloted Premixed Jet Burner (PPJB).

- However, work still needs to be done to further extend the FPV framework to account for extinction, re-ignition, and other phenomena what are governed by non-equilibrium chemistry.

- From the pressure spatial correlation data, it was concluded that the DLR Gas Turbine Model Combustor (GTMC) is dominated by a Helmholtz type resonance, and the volume of interest is the combination of the plenum and the combustor.

- Unlike the MIT model that only considers the combustor chamber or the EM2C model that requires experimental calibration, the proposed Modular Reduced-order Model Framework (MRMF) utilizes a set of coupled ODEs that consider a system with two volumes (plenum and combustion chamber) and two constrictions (injector and chimney).The measured frequency agrees with the frequency predicted by the Modular Reduced-order Model Framework (MRMF).

- The MRMF at its current form is tailored to model the GTMC specifically. It needs to be modified to model other setups. Additionally, its current form only considers Helmholtz-type instability and flat flames. If other target burners have different physics, the model will need to be extended before application.

- The reduced order model successfully explained most, but not all of the experimental data. The model is not predictive, but it shows that if a reasonable value of acoustic damping is estimated, several of the trends computed by the model are similar to the measured trends.

- The model provides an explanation to the dependence of combustion instability on equivalence ratios. It hypothesizes that heat release rate is controlled by the flow rate of the deficient stream. If the fuel flow rate is constant, then in all fuel lean conditions the heat release rate stays constant and combustion instability will not occur. This idea is an extension to existing equivalence ratio oscillation theories. It is only valid if we ignore the effect of fluid dynamics on flame and assume one-step chemistry. Hence its predictions are not general and should be confined to the present operating conditions of the GTMC.

- In a quiet flame where PLIF and pressure measurements show no signs of thermo-acoustic instability, PIV identified large velocity fluctuations caused by the PVC. This supports our hypothesis that mass flow rates oscillation alone does not necessarily result in acoustic instability.

- Experimental data shows that the instability frequency also depends linearly on laminar flame speed, which the current model is not capable of explaining. More research is needed to expand the model to account for this parameter.

6.3 Accomplishments

Major contributions of this work are:

- The ability of FPV model to predict partially premixed flames is assessed.

- A new joint PDF for the two mixture fractions in a three-stream FPV model is proposed.

- A new reduced order model based on multi-chamber Helmholtz resonator analysis is proposed to model combustion instability in a gas turbine model combustor.
- A new idea that at the current specific conditions the existence of combustion instability depends on the mass flow rates of the deficient stream is hypothesized.
- The variations of flame dynamics of a gas turbine model combustor over different equivalence ratios and mass flow rates are examined by high-speed laser diagnostic tools.

6.4 Recommendations for Future Work

We proposed the main framework of MRMF in this work, the main advantage of its modular approach is that it can be easily extended. This work provides a foundation for some related future studies:

- Currently the heat release model is based on the assumption of a simple one step chemistry. A heat release model that can *i*) consider multi-step chemical mechanisms; *ii*) account for effects of strain on the flame; *iii*) include non-equilibrium or finite-rate chemistry effects can be developed. The integration of a look-up table for experimentally calibrated flame transfer functions to the heat release model can be considered.
- Other parts of the MRMF also depend on some quite primitive models, which can be extended. For example, the relationship between velocity fluctuation and pressure difference fluctuation across the swirler may be upgraded from a simple pipe analysis to one that accounts for the swirl effects.
- The governing equations for pressure are currently based on Helmholtz analysis. Work can be done to incorporate other acoustic modes, such as standing waves, into the pressure analysis to accommodate other geometries. This may require the model to consider temporal and spatial variations, at which point the tradeoff between simplicity and accuracy needs to be evaluated.

APPENDIX

APPENDIX A

Operating procedures for combustion and laser experiments in room 2216b

General

1. Start Lab
2. Start LASER
3. Start Flame
4. Post Flame
5. LASER shut-off
6. Close Lab

Start Lab

1. Full light – on
2. Door – unlocked
3. Lab coat – on
4. Watch – off
5. Other PPE – as necessary

Start LASER

1. Cooling water for beam dump – on
2. Beam dump circulation water: 0.25-0.5 GPM
3. Beam dump circulation water: check leak
4. Clear all plastic wraps on optics
5. Check curtains in light path
6. LASER glass – double check on
7. Watch – double check off
8. LASER sign outdoor – on
9. Check DG – on
10. Check LASER cap – off
11. LASER controller – on

Start Flame

1. Exhaust – on
2. Wait for 5 min, Check Exhaust
3. Building air – on
4. Control panel: air valve on, needle valve open
5. Control panel: fuel valve on, needle valve open
6. N2 bottle – open
7. N2 bottle – close
8. Wait 5 min, check whether pressure drops
9. Servo – open
10. Control panel, fuel valve off, needle valve close
11. Double check headset – on
12. Fuel bottle – open
13. Control panel, fuel valve on, needle valve adjust
14. Control panel, fuel valve off, wait for 30 sec
15. Control panel, fuel valve – on
16. ignite

Post Flame

1. Control panel, fuel valve – off
2. Fuel bottle – off
3. N2 bottle – open
4. Control panel, fuel valve on, needle valve adjust
5. Wait for at least 5min
6. N2 bottle – close
7. Control panel, fuel valve off, needle valve close
8. Servo – closed
9. After GTMC to cool down, then building air off
10. Control panel, air valve off, needle valve off
11. Exhaust – off

LASER shut-off

1. LASER shut-down from controller
2. Safety glass – off
3. LASER sign – off
4. Beam dump water circulation – off
5. Plastic wraps on the optics – on

Close Lab

1. Power supply for Cameras & IRO and pressure transducer – off
2. Lens caps for Camera – on
3. Computer and all electronics on table – off
4. Check Fuel bottle pressure – zero
5. Check exhaust – off
6. Check water circulation – off
7. Main lights – off
8. Door – Locked

BIBLIOGRAPHY

BIBLIOGRAPHY

[1] Peters, N., *Turbulent Combustion*, Cambridge University Press, Cambridge, United Kingdom, 2000.

[2] Brackmann, C., Nygren, J., Bai, X., Li, Z., Bladh, H., Axelsson, B., Denbratt, I., Koopmans, L., Bengtsson, P.-E., and Aldén, M., "Laser-induced fluorescence of formaldehyde in combustion using third harmonic Nd:YAG laser excitation," *Spectrochimica Acta Part A: Molecular and Biomolecular Spectroscopy*, Vol. 59, No. 14, Dec. 2003, pp. 3347–3356. doi:10.1016/S1386-1425(03)00163-X.

[3] Dunn, M. J., Masri, A. R., and Bilger, R. W., "A new piloted premixed jet burner to study strong finite-rate chemistry effects," *Combustion and Flame*, Vol. 151, No. 1-2, Oct. 2007, pp. 46–60. doi:10.1016/j.combustflame.2007.05.010.

[4] Hathout, J. P., Fleifil, M., Annaswamy, A. M., and Ghoniem, A. F., "Combustion Instability Active Control Using Periodic Fuel Injection," *Journal of Propulsion and Power*, Vol. 18, No. 2, March 2002, pp. 390–399. doi:10.2514/2.5947.

[5] Schuller, T., Durox, D., Palies, P., and Candel, S., "Acoustic decoupling of longitudinal modes in generic combustion systems," *Combustion and Flame*, Vol. 159, No. 5, May 2012, pp. 1921–1931. doi:10.1016/j.combustflame.2012.01.010.

[6] Palies, P., Durox, D., Schuller, T., and Candel, S., "Nonlinear combustion instability analysis based on the flame describing function applied to turbulent premixed swirling flames," *Combustion and Flame*, Vol. 158, No. 10, Oct. 2011, pp. 1980–1991. doi:10.1016/j.combustflame.2011.02.012.

[7] Weigand, P., Meier, W., Duan, X. R., Stricker, W., and Aigner, M., "Investigations of swirl flames in a gas turbine model combustor I. Flow field, structures, temperature, and species distributions," *Combustion and Flame*, Vol. 144, No. 1-2, Jan. 2006, pp. 205–224. doi:10.1016/j.combustflame.2005.07.010.

[8] Steinberg, A. M., Boxx, I., Stöhr, M., Meier, W., and Carter, C. D., "Effects of Flow Structure Dynamics on Thermoacoustic Instabilities in Swirl-Stabilized Combustion," *AIAA Journal*, Vol. 50, No. 4, April 2012, pp. 952–967. doi:10.2514/1.J051466.

[9] Allison, P. M., Driscoll, J. F., and Ihme, M., "Acoustic characterization of a partially-premixed gas turbine model combustor: Syngas and hydrocarbon fuel

comparisons," *Proceedings of the Combustion Institute*, Vol. 34, No. 2, Jan. 2013, pp. 3145–3153. doi:10.1016/j.proci.2012.06.157.

[10] Allison, P. M., Chen, Y. T., and Driscoll, J. F., "Investigation of Dimethyl Ether Combustion Instabilities in a Partially - Premixed Gas Turbine Model Combustor Using High-Speed Laser Diagnostics," *AIAA Aerospace Sciences Meeting*, American Institute of Aeronautics and Astronautics, Reston, Virginia, Jan. 2014. doi:10.2514/6.2014-0660.

[11] Hersh, A. and Walker, B., "Fluid mechanical model of the Helmholtz resonator," Tech. Rep. September 1977, NASA Contractor Report, 1977.

[12] Pitts, W. M., "Assessment of theories for the behavior and blowout of lifted turbulent jet diffusion flames," *Symposium (International) on Combustion*, Vol. 22, No. 1, 1989, pp. 809–816.

[13] Rayleigh, J. W. S., "The Explanation of Certain Acoustical Phenomena," *Nature*, Vol. 18, No. 455, July 1878, pp. 319–321. doi:10.1038/018319a0.

[14] Lieuwen, T. C. and Zinn, B. T., "The role of equivalence ratio oscillations in driving combustion instabilities in low NOx gas turbines," *Symposium (International) on Combustion*, Vol. 27, No. 2, Jan. 1998, pp. 1809–1816. doi:10.1016/S0082-0784(98)80022-2.

[15] Schuller, T., Durox, D., and Candel, S., "Dynamics of and noise radiated by a perturbed impinging premixed jet flame," *Combustion and Flame*, Vol. 128, No. 1-2, Jan. 2002, pp. 88–110. doi:10.1016/S0010-2180(01)00334-0.

[16] Smagorinsky, J., "General circulation experiments with the primitive equations," *Monthly Weather Review*, Vol. 91, No. 3, March 1963, pp. 99–164. doi:10.1175/1520-0493(1963)091<0099:GCEWTP>2.3.CO;2.

[17] Germano, M., Piomelli, U., Moin, P., and Cabot, W. H., "A dynamic subgrid-scale eddy viscosity model," *Physics of Fluids A: Fluid Dynamics*, Vol. 3, No. 7, 1991, pp. 1760–1765. doi:10.1063/1.857955.

[18] Pierce, C. D., *Progress-variable approach for large-eddy simulation of turbulent combustion*, Ph.D. thesis, Stanford University, June 2001.

[19] Pierce, C. D. and Moin, P., "Progress-variable approach for large-eddy simulation of non-premixed turbulent combustion," *Journal of Fluid Mechanics*, Vol. 504, April 2004, pp. 73–97. doi:10.1017/S0022112004008213.

[20] Adrian, R. J., "Twenty years of particle image velocimetry," *Experiments in Fluids*, Vol. 39, No. 2, July 2005, pp. 159–169. doi:10.1007/s00348-005-0991-7.

[21] Raffel, M., Willert, C. E., Wereley, S. T., and Kompenhans, J., *Particle image velocimetry*, Springer, 2nd ed., 2010.

[22] Eckbreth, A. C., *Laser Diagnostics for Combustion Temperature and Species*, Gordon and Breach Publishers, 2nd ed., 1996.

[23] Lefebvre, A. H., *GAS Turbine Combustion*, Taylor & Francis, 2nd ed., 1999.

[24] Mongia, H. C., "TAPS - A 4th Generation Propulsion Combustor Technology for Low Emissions," *AIAA Paper 2003-2657*, 2003.

[25] Dhanuka, S. K., Temme, J. E., Driscoll, J. F., and Mongia, H. C., "Vortex-shedding and mixing layer effects on periodic flashback in a lean premixed prevaporized gas turbine combustor," *Proceedings of the Combustion Institute*, Vol. 32, No. 2, 2009, pp. 2901–2908. doi:10.1016/j.proci.2008.06.155.

[26] Dunn, M. J., Masri, A. R., Bilger, R. W., Barlow, R. S., and Wang, G.-H., "The compositional structure of highly turbulent piloted premixed flames issuing into a hot coflow," *Proceedings of the Combustion Institute*, Vol. 32, No. 2, 2009, pp. 1779–1786. doi:10.1016/j.proci.2008.08.007.

[27] Dunn, M. J., Masri, A. R., Bilger, R. W., and Barlow, R. S., "Finite Rate Chemistry Effects in Highly Sheared Turbulent Premixed Flames," *Flow, Turbulence and Combustion*, Vol. 85, No. 3-4, July 2010, pp. 621–648. doi:10.1007/s10494-010-9280-5.

[28] Rowinski, D. H. and Pope, S. B., "PDF calculations of piloted premixed jet flames," *Combustion Theory and Modelling*, Vol. 15, No. 2, March 2011, pp. 245–266. doi:10.1080/13647830.2010.535568.

[29] Duwig, C., Nogenmyr, K.-J., Chan, C.-k., and Dunn, M. J., "Large Eddy Simulations of a piloted lean premix jet flame using finite-rate chemistry," *Combustion Theory and Modelling*, Vol. 15, No. 4, Aug. 2011, pp. 537–568. doi:10.1080/13647830.2010.548531.

[30] Barlow, R. S., 2011, Tenth International Workshop on Measurement and Computation of Turbulent Nonpremixed Flames (TNF10).

[31] Barlow, R. S., 2012, Eleventh International Workshop on Measurement and Computation of Turbulent Nonpremixed Flames (TNF11).

[32] Ihme, M. and See, Y. C., "LES flamelet modeling of a three-stream MILD combustor: Analysis of flame sensitivity to scalar inflow conditions," *Proceedings of the Combustion Institute*, Vol. 33, No. 1, 2011, pp. 1309–1317. doi:10.1016/j.proci.2010.05.019.

[33] Ihme, M., Zhang, J., He, G., and Dally, B., "Large-Eddy Simulation of a Jet-in-Hot-Coflow Burner Operating in the Oxygen-Diluted Combustion Regime," *Flow, Turbulence and Combustion*, Vol. 89, No. 3, May 2012, pp. 449–464. doi:10.1007/s10494-012-9399-7.

[34] Peters, N., "Laminar diffusion flamelet models in non-premixed turbulent combustion," *Progress in Energy and Combustion Science*, Vol. 10, No. 3, Jan. 1984, pp. 319–339. doi:10.1016/0360-1285(84)90114-X.

[35] Dunn, M. J., *Finite-rate Chemistry Effects in Turbulent Premixed Combustion*, Ph.D. thesis, The University of Sydney, 2008.

[36] Ihme, M., Cha, C. M., and Pitsch, H., "Prediction of local extinction and reignition effects in non-premixed turbulent combustion using a flamelet/progress variable approach," *Proceedings of the Combustion Institute*, Vol. 30, Jan. 2005, pp. 793–800. doi:10.1016/j.proci.2004.08.260.

[37] Ihme, M. and Pitsch, H., "Prediction of extinction and reignition in nonpremixed turbulent flames using a flamelet/progress variable model 2. Application in LES of Sandia flames D and E," *Combustion and Flame*, Vol. 155, No. 1-2, Oct. 2008, pp. 90–107. doi:10.1016/j.combustflame.2008.04.015.

[38] Jiménez, J., Liñán, A., Rogers, M. M., and Higuera, F. J., "A priori testing of subgrid models for chemically reacting non-premixed turbulent shear flows," *Journal of Fluid Mechanics*, Vol. 349, Oct. 1997, pp. 149–171. doi:10.1017/S0022112097006733.

[39] Wall, C., Boersma, B. J., and Moin, P., "An evaluation of the assumed beta probability density function subgrid-scale model for large eddy simulation of non-premixed, turbulent combustion with heat release," *Physics of Fluids*, Vol. 12, No. 10, 2000, pp. 2522–2529.

[40] Ingram Olkin, Leon Jay Gleser, C. D., *Probablity Models and Applications*, Prentice Hall, 2nd ed., 1994.

[41] Samuel Kotz, N. Balakrishnan, N. L. J., *Continuous Multivariate Distributions*, Vol. 1, Wiley, 2nd ed., 2000.

[42] Pitsch, H., "FlameMaster v3.1: A C++ computer program for 0D combustion and 1D laminar flame calculations," 1998, available from http://www.stanford.edu/group/pitsch/.

[43] Ihme, M., *Pollutant Formation and Noise Emission in Turbulent Non-Premixed Flames*, Ph.D. thesis, Stanford University, 2007.

[44] Ihme, M. and See, Y. C., "Prediction of autoignition in a lifted methane/air flame using an unsteady flamelet/progress variable model," *Combustion and Flame*, Vol. 157, No. 10, Oct. 2010, pp. 1850–1862. doi:10.1016/j.combustflame.2010.07.015.

[45] Smith, G. P., Golden, D. M., Frenklach, M., Moriarty, N. W., Eiteneer, B., Goldenberg, M., Bowman, C. T., Hanson, R. K., Song, S., Gardiner, Jr., W. C., Lissianski, V. V., and Qin, Z., "GRI-Mech 3.0," 2000, available from http://www.me.berkeley.edu/gri-mech/.

[46] Bowman, C. T., Hanson, R. K., Davidson, D. F., Gardiner, W. C., Lissianski, V., Smith, G. P., Golden, D. M., Frenklach, M., and Goldenberg, M., "GRI-Mech 2.11," 1997, available from http://www.me.berkeley.edu/gri-mech/.

[47] Wang, H., You, X., Joshi, A. V., Davis, S. G., Laskin, A., Egolfopoulos, F., and Law, C. K., "USC Mech Version II, High-Temperature Combustion Reaction Model of H2/CO/C1-C4 Compounds," 2007, available from http://ignis.usc.edu/USC_Mech_II.htm.

[48] Lee, D. J., Thakur, S., Wright, J., Ihme, M., and Shyy, W., "Characterization of flow field structure and species composition in a shear coaxial rocket GH2/GO2 injector: modeling of wall heat losses," *AIAA/ASME/SAE/ASEE Joint Propulsion Conference*, San Diego, CA, Aug. 2011.

[49] Balusamy, S., Li, L. K., Han, Z., Juniper, M. P., and Hochgreb, S., "Nonlinear dynamics of a self-excited thermoacoustic system subjected to acoustic forcing," *Proceedings of the Combustion Institute*, Vol. 35, No. 3, 2015, pp. 3229–3236. doi:10.1016/j.proci.2014.05.029.

[50] Renaud, A., Ducruix, S., Scouflaire, P., and Zimmer, L., "Flame shape transition in a swirl stabilised liquid fueled burner," *Proceedings of the Combustion Institute*, Vol. 35, No. 3, 2015, pp. 3365–3372. doi:10.1016/j.proci.2014.07.012.

[51] See, Y. C. and Ihme, M., "Large eddy simulation of a partially-premixed gas turbine model combustor," *Proceedings of the Combustion Institute*, Sept. 2014. doi:10.1016/j.proci.2014.08.006.

[52] Candel, S., Durox, D., Schuller, T., Bourgouin, J.-F., and Moeck, J. P., "Dynamics of Swirling Flames," *Annual Review of Fluid Mechanics*, Vol. 46, No. 1, Jan. 2014, pp. 147–173. doi:10.1146/annurev-fluid-010313-141300.

[53] Noiray, N., Durox, D., Schuller, T., and Candel, S., "A unified framework for nonlinear combustion instability analysis based on the flame describing function," *Journal of Fluid Mechanics*, Vol. 615, Nov. 2008, pp. 139–167. doi:10.1017/S0022112008003613.

[54] Silva, C. F., Nicoud, F., Schuller, T., Durox, D., and Candel, S., "Combining a Helmholtz solver with the flame describing function to assess combustion instability in a premixed swirled combustor," *Combustion and Flame*, Vol. 160, No. 9, Sept. 2013, pp. 1743–1754. doi:10.1016/j.combustflame.2013.03.020.

[55] Kinsler, L. E., Frey, A. R., Coppens, A. B., and Sanders, J. V., *Fundamentals of Acoustics*, Wiley, 2000.

[56] Ducruix, S., Schuller, T., Durox, D., and Candel, S., "Combustion Dynamics and Instabilities: Elementary Coupling and Driving Mechanisms," *Journal of Propulsion and Power*, Vol. 19, No. 5, Sept. 2003, pp. 722–734. doi:10.2514/2.6182.

[57] Caux-Brisebois, V., Steinberg, A. M., Arndt, C. M., and Meier, W., "Thermo-acoustic velocity coupling in a swirl stabilized gas turbine model combustor," *Combustion and Flame*, Vol. 161, No. 12, Dec. 2014, pp. 3166–3180. doi:10.1016/j.combustflame.2014.05.020.

[58] Giezendanner-Thoben, R., Keck, O., Weigand, P., Meier, W., Meier, U., Stricker, W., and Aigner, M., "Periodic combustion instabilities in a swirl burner studied by phase-locked planar laser-induced fluorescence," *Combustion Science and Technology*, Vol. 175, 2003, pp. 721–741. doi:10.1080/00102200390196322.

[59] Giezendanner-Thoben, R., Weigand, P., Duan, X. R., Meier, W., Meier, U., Lehmann, B., Stricker, W., and Aigner, M., "Characterization of Thermoacoustic Instabilities in a Gas Turbine Model Combustor by Laser Spectroscopic Measurements," *Proceeding of the European Combustion Meeting 2003*, 2003.

[60] Duan, X. R., Meier, W., Weigand, P., and Lehmann, B., "Phase-resolved laser Raman scattering and laser Doppler velocimetry applied to periodic instabilities in a gas turbine model combustor," *Applied Physics B*, Vol. 80, No. 3, Jan. 2005, pp. 389–396. doi:10.1007/s00340-004-1722-0.

[61] Meier, W., Duan, X. R., and Weigand, P., "Investigations of swirl flames in a gas turbine model combustor II. Turbulencechemistry interactions," *Combustion and Flame*, Vol. 144, No. 1-2, Jan. 2006, pp. 225–236. doi:10.1016/j.combustflame.2005.07.009.

[62] Boxx, I., Arndt, C. M., Carter, C. D., and Meier, W., "High-speed laser diagnostics for the study of flame dynamics in a lean premixed gas turbine model combustor," *Experiments in Fluids*, Vol. 52, No. 3, Dec. 2010, pp. 555–567. doi:10.1007/s00348-010-1022-x.

[63] Stöhr, M., Arndt, C. M., and Meier, W., "Effects of Damköhler number on vortexflame interaction in a gas turbine model combustor," *Proceedings of the Combustion Institute*, Vol. 34, No. 2, Jan. 2013, pp. 3107–3115. doi:10.1016/j.proci.2012.06.086.

[64] Steinberg, A. M., Boxx, I., Stöhr, M., Carter, C. D., and Meier, W., "Flowflame interactions causing acoustically coupled heat release fluctuations in a thermo-acoustically unstable gas turbine model combustor," *Combustion and Flame*, Vol. 157, No. 12, Dec. 2010, pp. 2250–2266. doi:10.1016/j.combustflame.2010.07.011.

[65] Allison, P. M., *Experimental Characterization of Combustion Instabilities and Flow-Flame Dynamics in a Partially-Premixed Gas Turbine Model Combustor*, Ph.D. thesis, University of Michigan, 2013.

[66] Yu, K. H., Trouvé, A., and Daily, J. W., "Low-frequency pressure oscillations in a model ramjet combustor," *Journal of Fluid Mechanics*, Vol. 232, April 1991, pp. 47–72. doi:10.1017/S0022112091003622.

[67] Ahlborn, B., Seto, M. L., and Noack, B. R., “On drag, Strouhal number and vortex-street structure,” *Fluid Dynamics Research*, Vol. 30, No. 6, June 2002, pp. 379–399. doi:10.1016/S0169-5983(02)00062-X.

[68] Arcoumanis, C., Bae, C., Crookes, R., and Kinoshita, E., “The potential of di-methyl ether (DME) as an alternative fuel for compression-ignition engines: A review,” *Fuel*, Vol. 87, No. 7, June 2008, pp. 1014–1030. doi:10.1016/j.fuel.2007.06.007.

[69] Durox, D., Schuller, T., and Candel, S., “Self-induced instability of a premixed jet flame impinging on a plate,” *Proceedings of the Combustion Institute*, Vol. 29, Jan. 2002, pp. 69–75. doi:10.1016/S1540-7489(02)80013-X.

[70] Allison, P. M., Chen, Y. T., Ihme, M., and Driscoll, J. F., “Coupling of flame geometry and combustion instabilities based on kilohertz formaldehyde PLIF measurements,” *Proceedings of the Combustion Institute*, Vol. 35, No. 3, July 2015, pp. 3255–3262. doi:10.1016/j.proci.2014.05.127.